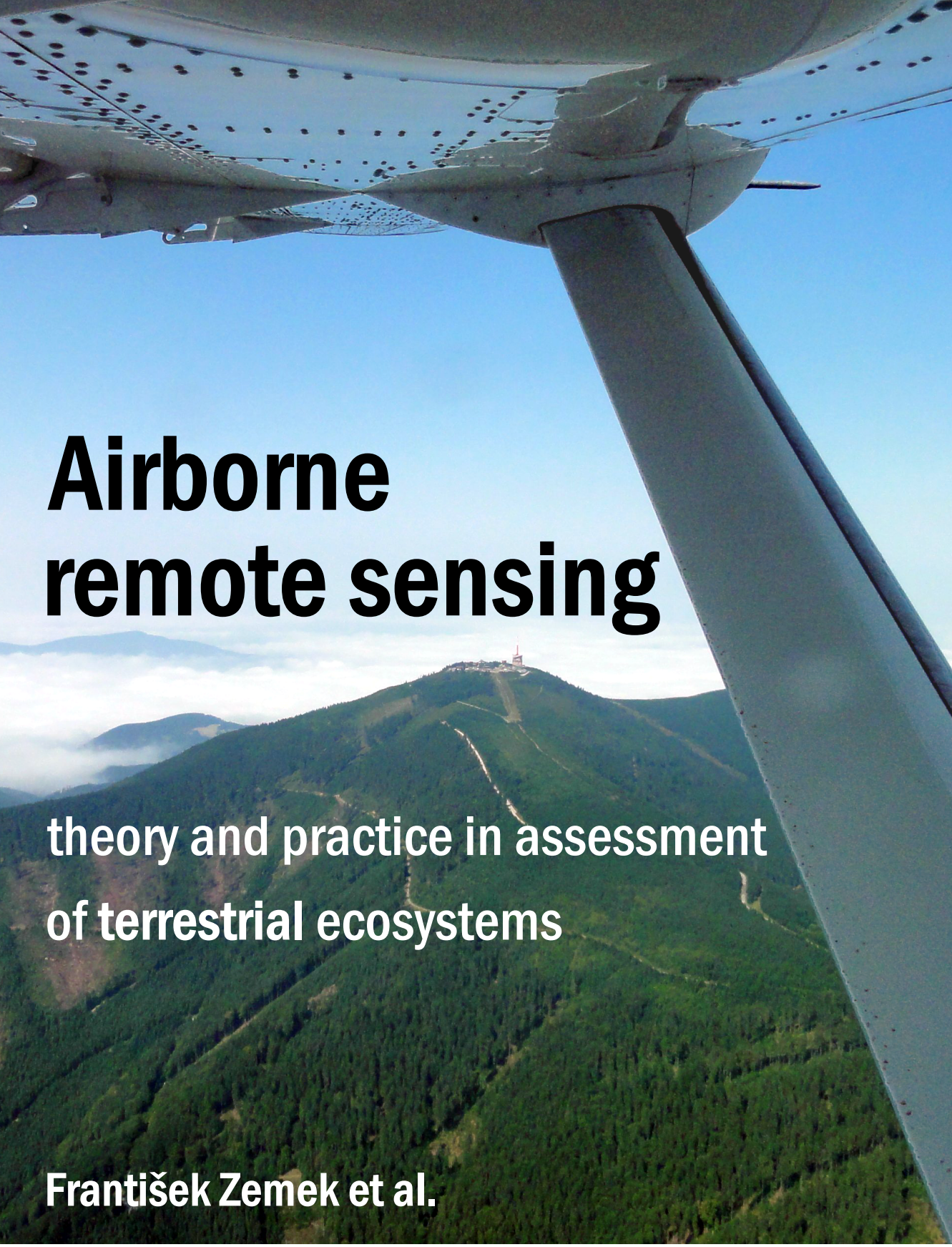

Airborne remote sensing

theory and practice in assessment of terrestrial ecosystems

František Zemek et al.

esf european social fund in the czech republic
EUROPEAN UNION
MINISTRY OF EDUCATION, YOUTH AND SPORTS
OP Education for Competitiveness
INVESTMENTS IN EDUCATION DEVELOPMENT

AIRBORNE REMOTE SENSING
THEORY AND PRACTICE IN ASSESSMENT OF TERRESTRIAL ECOSYSTEMS

FRANTIŠEK ZEMEK et al.

Reviewed by
Siri-Jodha Singh Khalsa, Ph.D., CIRES, Univ. of Colorado, Boulder, Colorado, USA

List of authors (in alphabetic order)
Jakub Brom, Miloš Cibulka, Tomáš Fabiánek, Jan Frouz, Jan Hanuš, Vlastimil Hanzl, Petra Hesslerová, Petr Hlavinka, Lucie Homolová, Růžena Janoutová, Vladimír Jirka, Jan Křen, Petr Lechner, Vojtěch Lukas, Martin Machala, Zbyněk Malenovský, Blahoslav Maršálek, Eliška Maršálková, Tomáš Mikita, Václav Nedbal, Jan Novotný, Marcela Pavlíková, Miroslav Pikl, Marek Pivovarník, Jan Pokorný, Jan Procházka, Fernando Rodriguez Moreno, Daniela Semerádová, Hana Vinciková, Olga Vindušková, František Zemek, Zdeněk Žalud

Acknowledgment
This monograph is published as a part of the project "The latest remote sensing technologies in the service of research, education and application for regional development", Reg. No. CZ.1.07/2.4.00/31.0213.

Graphical layout by Jan Holešovský
Cover page layout by Lucie Homolová
Cover page photo by Jan Hanuš
Language correction by Jitka Khalsa

Published by
Global Change Research Centre AS CR, v.v.i.
Bělidla 986/4a, CZ-603 00 Brno, Czech Republic

Printed by
www.knihovnicka.cz
Tribun EU s.r.o., Cejl 892/32, CZ-602 00 Brno, Czech Republic

Edition of 150 hard copies and 150 CDs, 159 pages

ISBN: 978-80-87902-05-9

AIRBORNE REMOTE SENSING

THEORY AND PRACTICE IN ASSESSMENT OF TERRESTRIAL ECOSYSTEMS

FRANTIŠEK ZEMEK et al.

Global Change Research Centre
AS CR, v.v.i.

CONTENTS

PREFACE

In recent decades the accelerating development of remote sensing (RS) and Earth navigation systems has created a high potential for their exploration in not only basic research but also in practical applications in disciplines such as forestry, agriculture, water management, urban planning, and the like. Unfortunately, current applications of RS in research, practical and management spheres do not fully reflect the opportunities that RS technologies offer. A prime reason for this may be a poor awareness of the potential that RS holds for other disciplines and end users.

This book aims to be a small contribution in helping to bridge the gap between RS specialists and potential users of RS data and information, and to increase the knowledge base for the application of the newest RS approaches in different disciplines.

From the very wide scope of RS we touch here only a small but still perhaps the most dynamically developing parts, namely imaging spectroscopy, laser scanning technologies and imaging thermography. And even though only short introductions to the theoretical principles of these RS branches are presented in Chapters 1 through 4, and the focus is on airborne platforms, we believe that this combination of RS tools is of high value owing to their complementarity. While spectral characteristic from narrow-band imagining spectroscopy and from imaging thermography can deliver information about the properties of objects on the Earth's surface, active laser scanning can provide information about structural parameters and spatial characteristics of those objects. This fusion can significantly contribute to the description of ecosystems and perhaps even revealing some causality in their behaviour.

Remote sensing is itself a very interdisciplinary field and it is not possible to enumerate all of its applications. The results of the project funded by the Czech Ministry of Education and entitled "Latest technologies of remote sensing in re-

search and education" (acronym HyDaP) form the basis of this book, but we went one step further. The RS team from the Global Change Research Centre AS CR recruited experts oriented in different aspects of ecosystems assessment who had almost no or very little background or experience in applications of RS in their branches. These included experts in soil biology and carbon sequestration from Biological Centre AS CR; fresh water monitoring from RAWAT consulting; thermal and water regime of landscape from University of South Bohemia and ENKI, o.p.s.; agriculture, precision farming and forestry from Mendel University in Brno. The Brno University of Technology contributed material on laser scanning.

The case studies in Chapters 5 to 10 document practical applications of airborne RS information in the above mentioned disciplines, going from soil and water assessment to more structurally complex ecosystems related to vegetation cover: agroecosystems, forests and landscape.

Each chapter of the book includes a basic recommended reading list related to the respective topic and comprehensive references to each case study. For these reasons the book can be seen as a useful information source for many categories of people. It can be an introductory reading for students who are starting with remote sensing or students who would like to test the potential of RS in their disciplines. The later group can be extended to researchers and specialist who study or observe different types of terrestrial ecosystems or their parts, and who search for new inspirations, interdisciplinary approaches or just simply need or would like to scale up their local measurements and information to broad spatial extent or interpolate point information to a continuous surface. Moreover, the CD attached to the book with already preprocessed hypterspectral and LiDAR data will enable different users to learn what the data are like and what information can be derived from it.

František Zemek

Global Change Research Centre AS CR

LIST OF ABBREVIATIONS

AAC	Autonomous Atmospheric Compensation
ABA	Area Based Approach
AISA	Airborne Imaging Spectrometer for Application
ALS	Airborne Laser Scanning
$ANCB_{650-720}$	Area under continuum-removed curve Normalized to the Chlorophyll absorption Band depth between 650 and 720 nm (vegetation index)
ANN	Artificial Neural Networks
APEX	Airborne Prism EXperiment
ATCOR	Atmospheric and Topographic CORrection (for airborne optical scanner data)
AUC	Area Under Curve
AVIRIS	Airborne Visible InfraRed Imaging Spectrometer
BBCH	Biologische Bundesanstalt, Bundessortenamt und CHemische Industrie (crop phenology scale)
BRDF	Bidirectional Reflectance Distribution Function
C_a	Chlorophyll a
C_{ab}	Chlorophyll a and b
CAD	Computer Assisted Design
CASI	Compact Airborne Spectrographic Imager
CBD	Continuum removal Band Depth
CHM	Canopy Height Model
CHRIS	Compact High Resolution Imaging Spectrometer
CR	Continuum Removal
DART	Discrete Anisotropic Radiative Transfer model
DBH	Diameter Breast Height
DEM	Digital Elevation Model

DLM	Dorsiventral Leaf radiative transfer Model
DLR	Deutsches Zentrum für Luft- und Raumfahrt (German Aerospace Centre)
DN	Digital Number
DSM	Digital Surface Model
DTM	Digital Terrain Model
EC	Electric Conductivity
EM	Electro-Magnetic (spectrum)
EO-1	The Earth Observing-1 mission
ESA	European Space Agency
FLI/PMI	Fluorescence Line Imager/Programmable Multispectral Imager
FLIGHT	Forest LIGHT interaction model (canopy radiative transfer model)
FMP	Forest Management Plan
FOM	Fossil Organic Matter
FOV	Field Of View
FPA	Focal Plane Array
FTIR	Fourier Transform Infrared
FWHM	Full Width Half Maximum
GCP	Ground Control Point
GIS	Geographic Information System
GNSS	Global Navigation Satellite System
GPS	Global Positioning System
ICT	Information and Computer Technologies
IFOV	Instantaneous Field of View
IMU	Inertial Measurement Unit
IR	Infra-Red
ISAC	In-Scene Atmospheric Corrections
ITD	Individual Tree Detection
KIA	Kappa Index of Agreement
LAI	Leaf Area Index
LEAFMOD	Leaf Experimental Absorptivity Feasibility MODel (leaf radiative transfer model)
LIBERTY	Leaf Incorporating Biochemistry Exhibiting Reflectance and Transmittance Yields (leaf radiative transfer model)
LPIS	Land Parcel Information System
LST	Land Surface Temperature
LUE	Light Use Efficiency
LUT	Look-Up Table
MERIS	Medium Resolution Imaging Spectrometer
MIR	Mid Infra-Red
MODIS	MODerate-resolution Imaging Spectroradiometer
MODTRAN	MODerate resolution atmospheric TRANsmission
NASA	National Aeronautics and Space Administration

NDVI	Normalized Difference Vegetation Index
NIR	Near Infra-Red
OBIA	Object-Based Image Analysis
OSAVI	Optimized Soil-Adjusted Vegetation Index
PARGE	PARametric Geocoding (Orthorectification for airborne scanner data)
Pc	Phycocyanin
PRF	Pulse Repetition Frequency
PRI	Photochemical Reflectance Index
PROBA	PRoject for On-Board Autonomy (satellite)
PROSPECT	A model of leaf optical PROperties SPECTra
RAMI	RAdiation transfer Model Intercomparison
REIP	Red-Edge Inflection Point
RMSE	Root Mean Square Error
ROI	Region Of Interest
ROSIS	Reflective Optics System Imaging Spectrometer
RS	Remote Sensing
RSOM	Recent Soil Organic Matter
RTE	Radiative Transfer Equation
RTM	Radiative Transfer Model (or modelling, depending on the context)
SAIL	Scattering by Arbitrarily Inclined Leaves (canopy radiative transfer model)
SAM	Spectral Angle Mapper (classification technique)
SASI	Shortwave Airborne Spectrographic Imager
SLOP	Stochastic model for Leaf Optical Properties
SNR	Signal-to-Noise Ratio
SOM	Soil Organic Matter
SPOT	Satellite Pour l'Observation de la Terre
SWIR	Short Wave Infra-Red
TCARI	Transformed Chlorophyll Absorption in Reflectance Index
TIR	Thermal Infra-Red
TLS	Terrestrial Laser Scanning
TWI	Topographic Wetness Index
UAV	Unmanned Aerial Vehicle
USGS	U.S. Geological Survey
UTM	Universal Transverse Mercator (coordinate system)
UV	Ultra-Violet
VI	Vegetation Index
VIS	VISible (radiation or part of EM spectra)
VNIR	Visible and Near Infra-Red
WBI	Water Band Index
ČÚZK	Czech Office for Surveying, Mapping and Cadaster (Český úřad zeměměřičský a kartografický)

1

INTRODUCTION AND BASIC THEORY OF REMOTE SENSING

Lucie Homolová, Marek Pivovarník, and František Zemek

Remote sensing (RS) in its broader sense means obtaining information about object through the analysis of data acquired by a device that is not in contact with the object. For example, our eyes are acting as remote sensors when they respond to the light reflecting from this page. Data on reflected light are analysed by our mental computer - brain to decode a collection of letters forming words and sentences. Beyond that, your brain can interpret the information that the sentences convey. Remotely collected data can be of many forms, including variations in force, acoustic wave, or electromagnetic energy distributions. In this book we talk about remote sensing as the interdisciplinary science and the technology that measures reflected or emitted electromagnetic radiation (EMR) from Earth-atmosphere system to obtain data and information about its properties. More specifically, we will talk about digital remote sensing from airborne platforms and focus on three currently evolving technologies: hyperspectral remote sensing (also called as imaging spectroscopy), laser scanning and thermal remote sensing.

This chapter introduces in a rather condensed way the fundamental theory

and basic principles of remote sensing. The discussion here is based on the books by Lillesand & Kiefer (2000) and Campbell & Wynne (2011). Interested readers are referred to those books for more details.

1.1 History of Remote Sensing

The origins of remote sensing can plausibly be traced back to the 4^{th} century BC and Aristotle's camera obscura. The technology of modern remote sensing began with the invention of photography. The very first attempts to form an image date from the early 1800's. Although the first, rather primitive photographs were taken on the ground, the practice of taking downward looking pictures from cameras secured to balloons started in 1858 when Gasper Felix Tournachon took the first aerial photograph of Paris. With the invention of aircraft in early 1910's, the technology of aerial photography moved for next five decades from balloons to other airborne platforms. As a curiosity, perhaps the most novel and extraordinary platform for aerial photography, invented at the beginning of the 20^{th} century, was a fleet of trained pigeons that operated in Germany.

Color photography became available in the mid-1930's. Massive development of RS technology came with World Wars. WWI marked the beginning of routine use of aerial photography when over one million of aerial reconnaissance photographs were taken. WWII pushed the development in RS technology beyond the visible part of the electromagnetic spectrum to the near-infrared (NIR) and microwave regions. The NIR was particularly useful for haze penetration, active microwave systems (RADAR - Radio Detection And Ranging) to detect and track moving objects such as ships and aircrafts. The logical entry of RS technology into space began with the inclusion of automated photocameras, hand in hand with both Russian and American space programs. First photographs from space were captured from V-2 rockets that were acquired from Germany after WWII and launched from New Mexico in 1946. First satellite-based operational systems for collecting digital information about the Earth on a regular basis were launched in 1960's (e.g. the meteorological satellite of the TIROS series). More advanced systems followed in 1970's when US launched the Landsat program.

The first exciting images provided by the early meteorological satellites and manned space missions stimulated NASA to begin a conceptual study of a series of Earth Resources Technology Satellites (ERTSs). The program that started in 1967 and resulted in a sequence of eight Earth observing satellites is better known as the Landsat program (officially renamed from ERTS to Landsat in 1975). The first satellite was launched on July 23, 1972. Nowadays, two satellites Landsat-7 and Landsat-8 (earlier referred as Landsat Data Continuity Mission) are still operational and provide digital image data in a multispectral mode (6–11 spectral bands) and of moderate spatial resolution (30–100 m). The Landsat program provides the longest continuous space-based global record of the Earth's

surface. The unique data provided by Landsat multispectral sensors resulted in a vast range of applications (Cohen & Goward 2004; Hansen & Loveland 2012).

In general we can conclude that since the 1980's remote sensing technology, spaceborne as well as airborne systems, for land, ocean and meteorological observations has been flowering and rapidly developing. In 1980's, the development of airborne hyperspectral remote sensing (also synonymous for imaging spectroscopy or imaging spectrometry) started. Airborne imaging spectrometers become available on a wider basis in late 1980's and early 1990's. This phase of development resulted in the launch of first spaceborne imaging spectrometers MODIS and MERIS. Nowadays, airborne imaging spectrometers provide data of unprecedented radiometric quality with ultra-fine (sub-nanometer) spectral resolution.

Active laser scanning technology (LiDAR – Light Detection And Ranging), although it had been known since the 1960's and based on the same principle as RADAR, was opened to the airborne applications thanks to the development of precision navigation (GNSS and IMU) technologies which also matured in during 1980's and 1990's. Early laser scanners from 1990's were capable of emitting and recording 2 to 25 thousand pulses per second. Although primitive by today's standards, these instruments were already delivering dense data sets, which stimulated a rapid improvement of CAD and GIS processing software to handle such a large volume of data. Currently, there are more than a hundred (Baltsavias 1999) LiDAR systems operating worldwide that are capable of 250,000 pulses per second, capturing multiple returns from individual pulses, or even digitizing the full return waveform. More details about LiDAR can be found in Chapter 4.

Development of thermal infra-red remote sensing technology accelerated during WWII thanks to the development of advanced detectors. The technology was strictly used for military purposes, but in 1960's the US government declassified some coarse-resolution thermal infra-red systems. The first multispectral thermal scanner (TIMS) was developed by NASA JPL in 1980. The multispectral scanner of Landsat 3, launched in 1978 carried a thermal sensor. ASTER has been providing multispectral (5 channel) TIR data since 2000. Nowadays, there are two satellite missions in preparation that will provide multispectral thermal RS data of global coverage. These are Sentinel-3 developed by ESA and HyspIRI developed under the NASA governance. Moreover, to our best knowledge, there are currently three commercially available airborne hyperspectral thermal systems and a few prototype systems build for research purposes (more details in Section 3.2).

1.2 Basic Concepts of Remote Sensing

1.2.1 The Electromagnetic Spectrum

The most obvious source of electromagnetic (EM) radiation is the Sun. However, with the exception of objects at absolute zero, all objects also emit EM radiation. By recording reflected or emitted radiation from objects on the Earth's surface,

Table 1.1 Milestones in the history of remote sensing. More complete account can be found at `http://www.geog.ucsb.edu/~jeff/115a/remotesensinghistory.html` or in Stoney (2005).

Period	Milestones in the history
$\approx$ 1827	Joseph Niepce takes first picture of French countryside from a window. It took 8 hours in bright sunlight to produce the image.
1858	Gaspard Felix Tournachon, known as "Nadar" used a balloon to ascend to a height of 80m to obtain the first aerial photograph over Paris.
1858	James Clerk Maxwell, a Scottish physicist, describes colour additive theory for the producing colour photographs.
1909	Wilbur Wright takes first aerial photograph from an airplane of Centocelli, Italy, using a motion picture camera.
1910's	WWI provided a boost in the use of aerial photography, but after the war, enthusiasm waned.
1920's–30's	Development and first non-military applications of aerial photography for forestry and agriculture.
1934	American Society of Photogrammetry (now the American Society for Photogrammetry and Remote Sensing) was founded and the journal Photogrammetric Engineering published first time.
1940's	WWII brought more sophisticated techniques into air photo interpretation and development in nonvisible – infrared and microwave regions.
1946	First space photographs were captured from V–2 rockets that were acquired from Germany after WWII and launched out of White Sands in New Mexico.
1950's	First time the term "remote sensing" is being used by Ms. Evelyn Pruitt of the U.S. Office of Naval Research.
1960	TIROS-1 (Television and Infrared Observation Satellite) was launched by NASA as the first declassified satellite used for meteorological purposes.
1972	Launch of ERTS-1, NASA's first Earth Resources Technology Satellite (later renamed Landsat 1). It carried return beam vidicon and multispectral scanner.

Continued Table 1.1

Period	Milestones in the history
1977	Launch of Meteosat-1, the first in a long series of European weather satellites.
1980's	Development of hyperspectral sensors.
1990's	Remote sensing boom – launch of satellite- and airborne-based sensors by national agencies and commercial companies. Rapid development of global remote sensing systems and laser scanning technology.
1995	Launch of OrbView-1 the world's first commercial imaging satellite.
1999	Launch of NASA's flagship of Earth Observing System – Terra platform that provides global data on the state of atmosphere, land and oceans (MODIS, ASTER, CERES, MISR and MOPITT instruments onboard).
2002	Launch of Envisat, the largest Earth observation satellite build by ESA, that carried 10 instruments to provide continuous observation of Earth's land, atmosphere, oceans and ice caps. The mission was terminated in 2012 due to a sudden loss of contact with the satellite.
2005	Google Inc. Releases Google maps and Google Earth applications that greatly increase public awareness of geospatial data.
2010's	Expected launch of ESA series of five Sentinel satellites. (Sentinel 1 already launched.)

and applying knowledge of their behaviour, remote sensing can infer properties of those objects.

The most familiar electromagnetic radiation is visible light, which represent only a small, but very important, portion of the entire EM spectrum (400–700 nm). However, other spectral regions, such as infra-red and microwave, are equally important for remote sensing. Figure 1.1 shows the major division of the EM spectrum based on wavelength and convention names. In reality there are no sharp breaks between the spectral regions, they are only established for convenience. It should be noted that these divisions can differ among disciplines.

The part of the EM spectrum that is typically used for remote sensing spans from about 380 nm up to 1 m. The ultraviolet spectrum (UV, 300–380 nm) is rarely used for remote sensing of Earth surfaces as it is easily scattered by the atmosphere. Passive remote sensing instruments that measure reflected solar radiation from Earth surfaces operate in so called reflective domain of the EM spectrum (380–3000 nm), which contains the visible (VIS, 400–720 nm), the near

(NIR, 720–1300 nm) and the mid (MIR, 1300–3000 nm) infra-red regions. The far infra-red region (3–1000 µm) of the EM spectrum is fundamentally different from the visible of the near infra-red regions. The far infra-red radiation is emitted by Earth surfaces and it is popularly called "heat" or "thermal" energy. More specifically, the region of 8 to 14 µm refers most often to thermal infra-red (TIR) in remote sensing. The longer wavelengths of the microwave regions (1 mm up to 1 m) are used by passive and active radar systems, which are beyond the scope of this book.

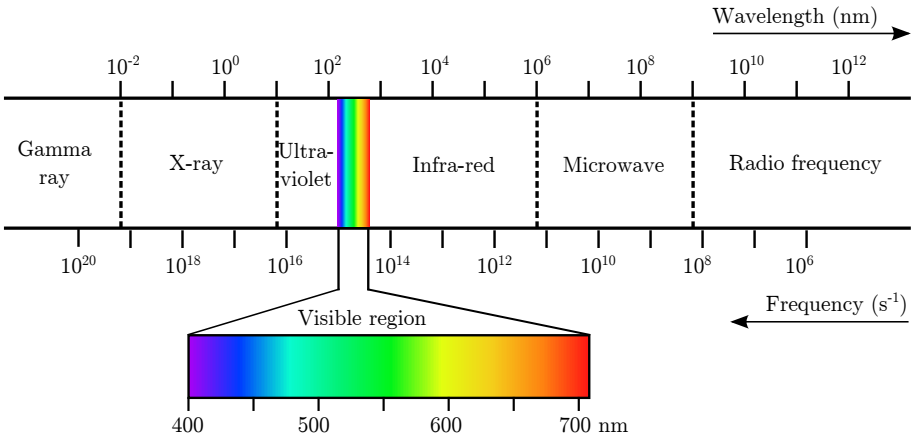

Figure 1.1 The electromagnetic spectrum.

1.2.2 Radiation Laws

The dual characteristics of electromagnetic radiation are described by two theories, the wave and the particle theory. The wave theory (Figure 1.2) describes EM energy as travelling in harmonic, sinusoidal waves at the velocity c. The distance from one wave peak to the next is the wavelength λ, and the number of peaks passing a fixed point in space per unit time is the wave frequency ν. The electromagnetic waves thus obey the general equation

$$c = \nu\lambda. \tag{1.1}$$

Since the velocity of light c is constant ($3 \cdot 10^8$ m sec), frequency and wavelength for any given wave are related inversely.

The second theory, the theory of particles, states that electromagnetic radiation is emitted and absorbed in discrete units called quanta or photons. As defined by Max Planck (1858–1947), the energy of a quantum Q is given

$$Q = h\nu, \tag{1.2}$$

where h is Planck's constant ($6.626 \cdot 10^{-34}$ J sec) and ν is frequency.

We can related the wave and particle models of electromagnetic radiation by solving eq. 1.1 for ν and substituting into eq. 1.2 to obtain

$$Q = \frac{hc}{\lambda}. \tag{1.3}$$

The energy of a quantum Q decreases with increasing wavelength. This property has important implication for remote sensing meaning that longer, e.g. microwave radiation is more difficult to record than shorter wavelengths with their higher energy content.

The amount of emitted energy increases rapidly with the kinetic temperature of an object and it is expressed by the *Stefan-Boltzman law*

$$M = \sigma T^4, \tag{1.4}$$

where M is total radiant emittance from an object ($\mathrm{W\,m^{-2}}$), σ is Stefan-Boltzmann constant ($5.6697 \cdot 10^{-8}\,\mathrm{W\,m^{-2}\,K^{-4}}$), T is the kinetic temperature of an emitting object (K). The kinetic temperature is a physical property expressing the amount of internal energy of an object (solid, liquid or gas) due to the displacement or rotation of atoms or molecules.

The total amount of radiation emitted by an ideally emitting (i.e. "blackbody") object varies with its kinetic temperature, and the wavelength at which an object emits the maximum of the energy is a function only of its kinetic temperature (T). This relationship is defined by the Wien's displacement law as follows

$$\lambda_{max} = \frac{A}{T}, \tag{1.5}$$

where λ_{max} is the wavelength of maximum emitted radiance (µm), A is a constant of $2898\,\mu\mathrm{m\,K}$, and T is the kinetic temperature (K). Wien's law tells us that that higher the kinetic temperature the lower the wavelength with the maximum emitted radiation.

Both principles described above are clearly summarized by Planck's radiation law (Planck 1900). Planck's radiation law assumes that energy sources behave as perfect blackbodies. A perfect blackbody is a hypothetical, ideal radiator that totally absorbs and reemits all energy incident upon it. A perfect blackbody does not exist in the nature, but can be approximated using laboratory instruments. All real objects reflect at least a small proportion of the radiation and thus do not act as perfect blackbodies. They emit only a fraction of the energy that a blackbody with equivalent temperature can emit. Thus the efficiency of an object radiating energy compared to a perfect blackbody of the same temperature is described by a factor called *emissivity* ε

$$\varepsilon = \frac{M_{RB}}{M_{BB}} \tag{1.6}$$

where M_{RB} and M_{BB} is the radiant remittance of a real body and a perfect blackbody respectively. Emissivity, which for real objects varies with wavelength,

can reach values between 0 and 1. The emissivity of a perfect blackbody is 1, and that of a perfect reflector (a whitebody) is 0. In nature, most of the objects have emissivities falling into a range from 0.85 to 0.99 (Lillesand & Kiefer 2000).

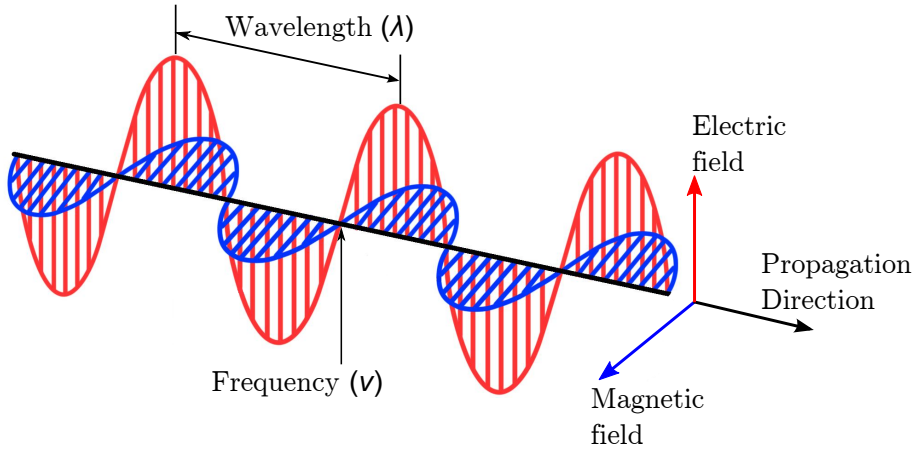

Figure 1.2 An electromagnetic wave with sinusoidal vibration states in the electric and magnetic field. Wavelength is defined as a distance between successive wave peaks. Frequency is defined as number of cycles passing a fixed point per second.

1.2.3 Interactions with the Atmosphere

Irrespective of its source, all radiation detected by remote sensing sensors has to travel through the atmosphere. The atmosphere can have a profound effect on the intensity and the spectral composition of radiation reaching a remote sensing system. As electromagnetic radiation passes the atmosphere, it is subject to modification by physical process of scattering and absorption.

Scattering

Atmospheric scattering is the redirection of radiation by particles suspended in the atmosphere or by large molecules of atmospheric gasses. The amount of scattering depends on the sizes of these particles, their abundance, the wavelengths of the radiation, and the path length that radiation travels through the atmosphere. We differentiate two types of scattering, Rayleigh and Mie scattering.

Rayleigh scattering occurs when radiation interacts with molecules of atmospheric gases or very tiny particles that have diameter very small relative to the wavelength of the radiation. It means that shorter wavelengths are being scattered much stronger than longer wavelengths. Blue light is scattered about four times as much as is red light and this is the reason why the sky appears blue. At sunrise and sunset, however, the solar radiation travels through a longer atmospheric path than during midday. With the longer path, the scatter (and subsequently the

absorption) is so complete that we see only the less scattered, longer wavelengths of orange and red.

Mie scattering occurs when radiation interacts with particles of the size that is roughly equivalent to the wavelength of the passing radiation. These particles include dust, pollen, smoke and water droplets. Although Rayleigh scattering tends to dominate under most atmospheric conditions, Mie scattering can significantly influence the visible and the near infra-red regions.

Absorption

Atmospheric absorption occurs when atmospheric constituents retain the passing radiation and attenuate its transmission. Most of the absorption of solar radiation is caused by only three atmospheric gasses, namely ozone (O_3), carbon dioxide (CO_2) and water vapour (H_2O). Although all three barely reach up 3–5 % by volume, they are responsible for most of the absorption. O_3 absorbs shortwave ultraviolet radiation (below 240 nm) and between 9 and 10 µm in the thermal infra-red. CO_2 absorbs in the mid and far infra-red regions (most strongly from 13 to 17.5 µm). H_2O is several times more effective in absorbing radiation than all other atmospheric gasses combined. The strongest water absorption occurs between 1 and 2.5 µm, 5.5 and 7 µm and above 27 µm. It is obvious that the absorbing gasses attenuate the passing radiation differently in different spectral regions. It is also important to realize that some gasses and suspended particles may emit radiation of their own and amplify the emitted signal recorded by thermal scanners. In general, spectral regions that are least affected by the atmosphere, and where radiation transmits easily, are called atmospheric windows (Figure 1.3). Atmospheric windows have important implications for remote sensing because they allow RS instruments to measure radiation from the surface without it being fully absorbed by the atmosphere. In the solar domain, it corresponds to a region between 400 and 2500 nm, in the thermal domain, the spectral range least affected by the atmosphere is located between 10 and 12 µm.

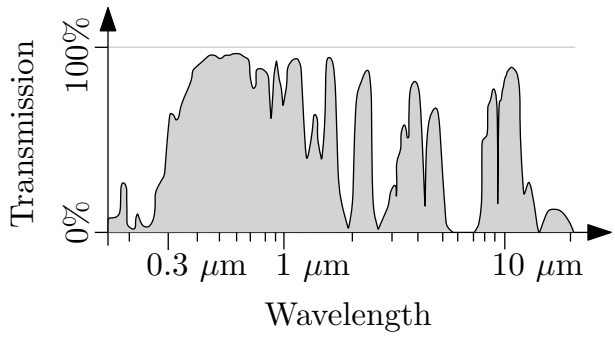

Figure 1.3 Atmospheric transmission for electromagnetic radiation coming from Sun.

1.2.4 Interaction of Radiation with Matter

As many RS instruments operate in spectral regions in which reflected energy dominates (i.e. 400–2500 nm), the following discussion on basic theory of radiation interaction with earth surfaces holds true for the reflective domain only. The thermal domain is covered later on in Chapter 3.

We shall first introduce the basic radiometric quantities. For better overview, Figure 1.4 provides a brief summary of basic radiometric quantities and their commonly used units. Their simplified definitions are stated in form of equations.

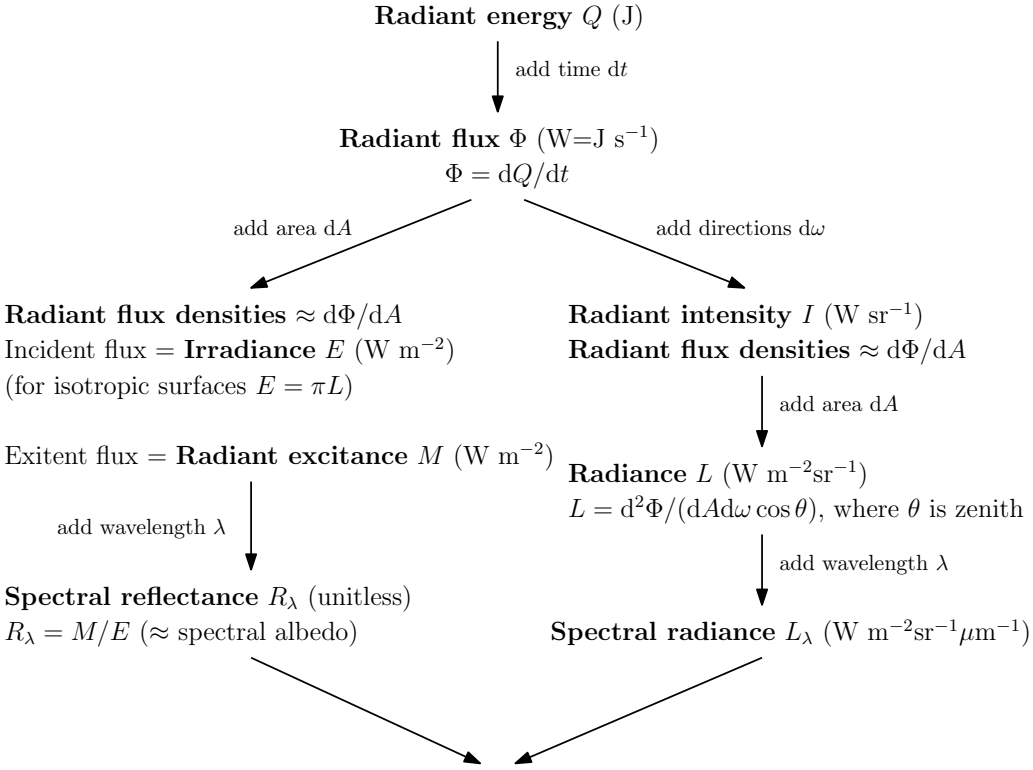

Figure 1.4 Summary of radiometric terms and definitions.

When electromagnetic radiation interacts with a surface, it is partly absorbed, transmitted or scattered (reflected). The principle of energy conservation states that the incident radiant flux (E_i) is totally distributed among reflected (E_r), transmitted (E_t) and absorbed (E_a) fractions.

$$E_i = E_r + E_t + E_a. \tag{1.7}$$

The proportion between reflected, transmitted and absorbed is wavelength dependent and furthermore it depends on chemical composition and surface roughness.

The reflectance characteristics of earth surfaces may be quantified by measuring the portion of incident energy that is reflected in a specific wavelength. The geometric behaviour of reflected energy is extremely important for remote sensing. This is mainly influenced by the surface roughness. Ideal smooth surfaces act as a mirror (specular reflectance), whereas ideal rough surfaces reflect uniformly in all directions (Lambertian reflectance) (Figure 1.5). Most of earth surfaces reflect somewhere between the specular and Lambertian cases.

The reflective characteristics of a surface are completely described by the bidirectional reflectance distribution function (BRDF). BRDF is a theoretical description of the geometrical behaviour of reflectance with respect to angle of illumination and observation. Spectral BRDF is defined as ratio of the reflected radiance from a surface in the direction relative to the incident irradiance on the surface.

BRDF is rather a theoretical concept. Real remote sensing measurements do not coincide with the bidirectional reflectance quantities as RS sensors integrate the reflected signal over a large viewing solid angle. Term "reflectance" can be to some extent ambiguous as it might refer to slightly different physical quantities. Here we refer interested readers to the paper of Schaepman-Strub et al. (2006), who clearly define various reflectance quantities used in the optical RS studies.

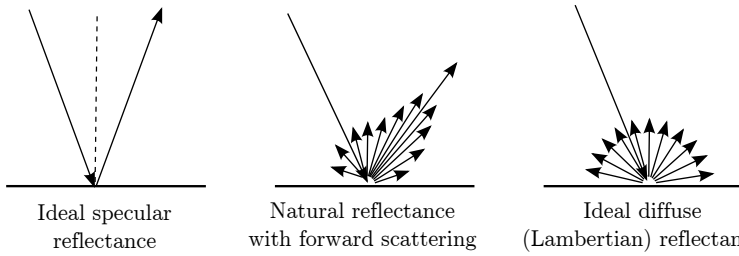

Figure 1.5 Specular versus diffuse reflectance.

1.3 Optical and Thermal Properties of Surfaces

All surfaces can be characterized by their spectral signatures, which can act like a fingerprint. The spectral signature allows us to differentiate among visually similar surfaces, to classify images into thematic groups with similar spectral signatures. Furthermore, we can analyse spectral signatures in order to derive some quantitative properties of surfaces.

In this chapter we show typical spectral signatures in the reflective, as well as in the thermal domain, of common surfaces (vegetation, soil, water and artificial surfaces). All spectral signatures are reproduced from the ASTER spectral library (`http://speclib.jpl.nasa.gov/`) (Baldridge et al. 2009).

Vegetation

The spectral signature of vegetation in the reflective domain has a very characteristic shape (Figure 1.6a). In the visible wavelengths, the spectrum is influenced by strong absorption of plants' pigments (chlorophylls a and b absorbing mainly around 450 and 660 nm). The near infra-red region is characterized by a rather flat signature influenced by internal leaf structure and overall canopy architecture. The mid infra-red region exhibits several broad and strong absorption by plant water (around 1200, 1450, 1940 and 2500 nm). Furthermore, other plant compounds, such as lignin, cellulose, starch, proteins and nitrogen absorb in the mid infra-red. In the thermal region, compared to the reflective region, the spectral response (expressed by the object's emissivity) of vegetation is almost flat without any prominent features (Figure 1.6b).

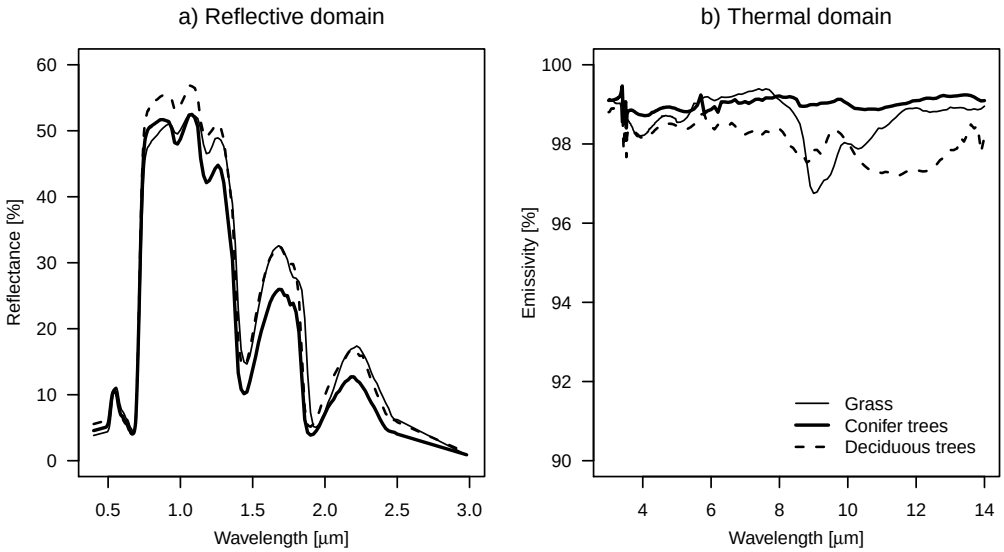

Figure 1.6 Vegetation spectral signatures in the (a) reflective and (b) thermal domain.

Soils

Spectral properties of soils are influenced by four main factors: mineral composition, soil moisture, organic matter and soil texture. In the reflective domain (Figure 1.7a), organic matter has a very important influence, because amounts exceeding 2 % reduce the overall reflectivity and mask the diagnostic absorption features determined by mineral composition. The absorption features of minerals are mainly located in the shortwave infra-red region and extend further into the thermal domain. For example, little absorption located at 2.2 um and sharp broad feature starting at 2.7 um indicate the presence of clay minerals such as kaolinite and montmorillonite. Another important factor influencing the reflective proper-

ties of soils is water. Increasing moisture content generally decreases the overall reflectance of soils. The most prominent features that are located around 1.4 and 1.9 µm are due to the water absorption. In the thermal domain (Figure 1.7b) the strong double feature between 7.7 and 9.7 µm is due to quartz presence in soils.

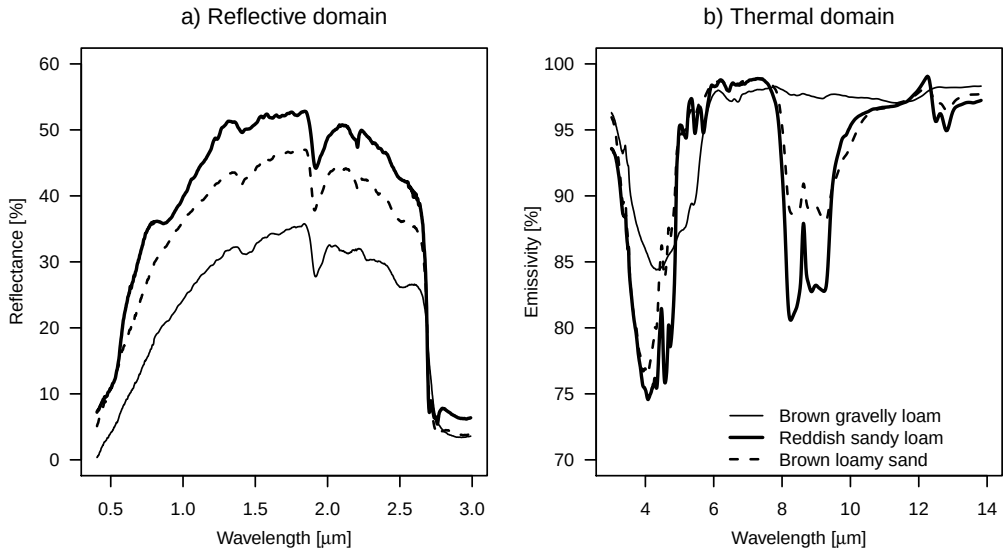

Figure 1.7 Spectral signatures of dry soils in the (a) reflective and (b) thermal domain.

Water

In very clear waters almost all radiation is absorbed or transmitted except a small fraction being reflected in the blue region (400–500 nm). However suspended sediments, plankton, water plants and water turbidity increase the reflective signal in the near infra-red wavelengths. Still, the reflected signal of water is much lower compared to snow, which reflects almost all the incident radiation in the visible wavelengths (Figure **??**a). In the thermal region, most of the incident radiation is being emitted and as seen in Figure 1.8b, the spectral signature is almost flat, without any prominent features.

Artificial surfaces

It is impossible to provide a characteristic spectral signature of artificial, man-made surfaces because of their enormous variability. Therefore we show only a very few examples of materials such as construction asphalt, concrete and a roofing material (Figure 1.9). Their spectra help in the classification of objects in multispectral or hyperspectral images.

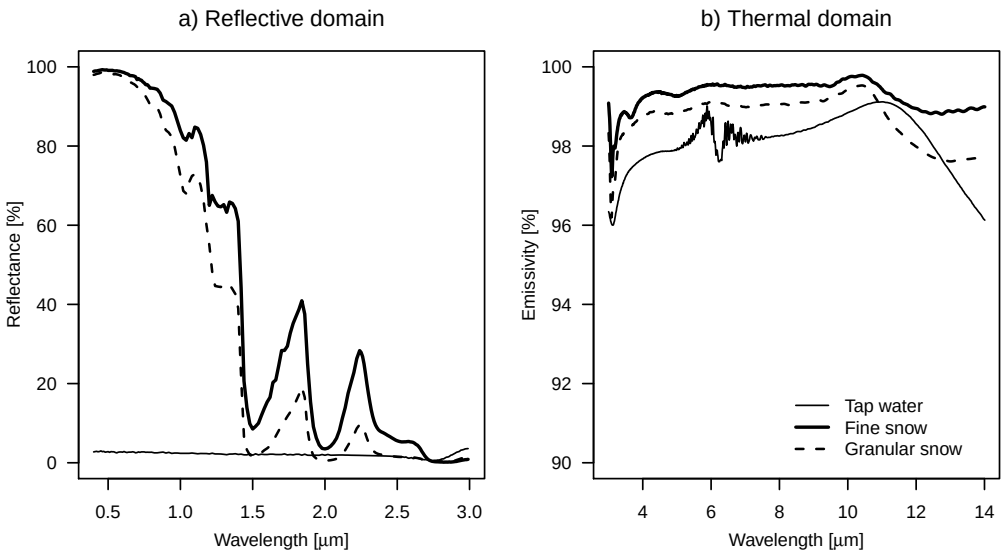

Figure 1.8 Water and snow spectral signatures in the (a) reflective and (b) thermal domain.

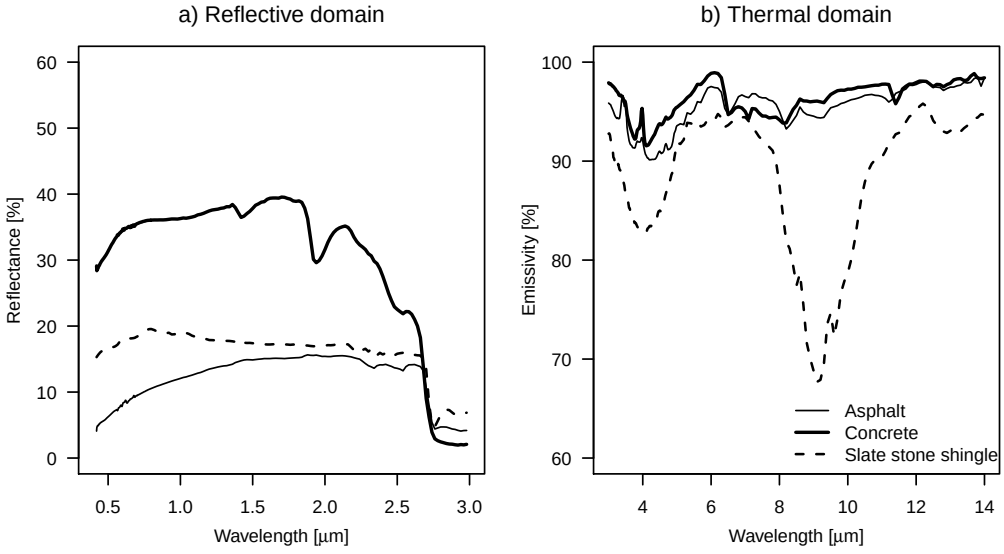

Figure 1.9 Spectral signatures of artificial surfaces in the (a) reflective and (b) thermal domain.

1.4 Principles of Airborne Scanning

There are three basic types of radiation used in electromagnetic remote sensing: a) diffused scattering of incoherent EM, b) emission and c) reflection of artificial coherent waves (Figure 1.10). Acquisition of digital imagery in general can be accomplished in passive or active regime. The first two types refer to the passive remote sensing and the third one to active RS.

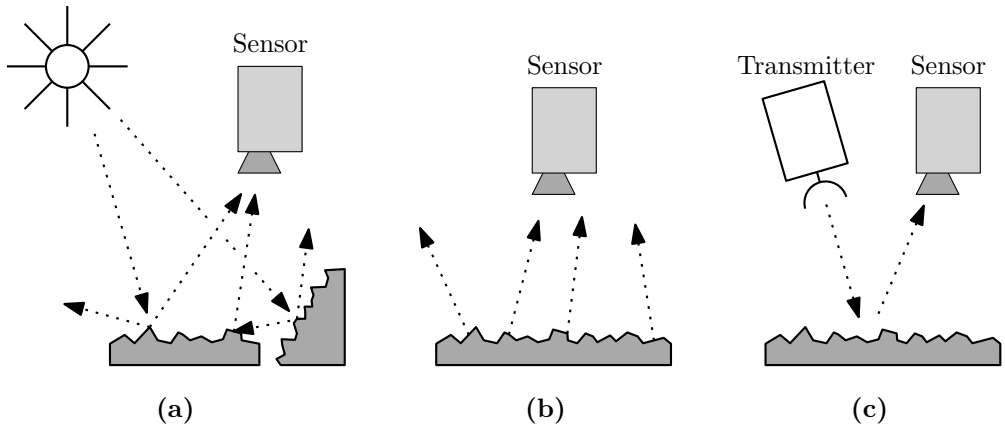

Figure 1.10 Three basic types of radiation used in electromagnetic remote sensing: (a) diffused scattering of incoherent EM, (b) emission and (c) reflection of artificial coherent waves. Passive remote sensing is represented by (a) and (b) and active remote sensing by (c).

In this book we are going to discuss all three forms of acquisition executed from an airborne platform. In the first form, a spectrometer records the reflected solar radiation, usually between 400 and 2500 nm. This is further discussed in Chapter 2. In the second form, emitted radiation from Earth's surfaces is recorded by a thermal scanner. This is further discussed in Chapter 3. The active sensing is represented here by laser scanning technology, which differs from the previous two by having distinct operating principles. This is further introduced in Chapter 4. In terms of operating principles and image geometry, active laser scanning is fairly distinct from the passive instruments (Figure 1.11). Therefore, the content of this chapter concerns mainly hyperspectral and thermal RS rather than laser scanning. In this chapter we will introduce basic operating principles of digital image data acquisition, clarify terms such as spatial and spectral resolutions and introduce ancillary onboard and field measurements.

Operating principles of image acquisition

If we imagine a remotely sensed image as a 3D data matrix, x and y dimensions refer to the horizontal spatial coordinates and the z dimension refers to the spectral domain (see Figure 2.2 for better illustration of the 3D data matrix). In

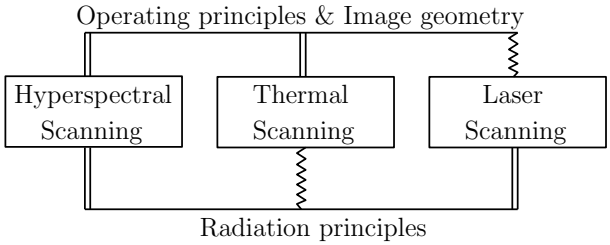

Figure 1.11 Similar (double lines) and dissimilar (zigzag lines) principles behind the three forms of remote sensing discussed in this book (hyperspectral, thermal and laser airborne scanning).

terms of operational data acquisition, there are two most commonly used scanning mechanisms, allowing the formation of the 3D data matrix. The two types are whiskbroom and pushbroom scanners (Figure 1.12).

A whiskbroom scanner is an electro-mechanical device that collects lines of individual pixels across-track (perpendicular to the direction of flight) using either a scanning mirror sweeping from one edge of the flight swath to the other or the mechanical rotation of the sensor system. The along-track dimension of an image is acquired by the forward movement of the plane (Figure 1.12a). The particular advantage of this scanning principle is a higher spectral uniformity since all pixels are recorded using the same detector. The disadvantage is that the mechanical part makes the instrument more expensive, more likely to wear out and often causing resonance that may be observed in the data as striping. Airborne imaging spectrometers using the whiskbroom scanning principle are e.g. AVIRIS and HyMap.

A pushbroom scanner is an electronic device that consists of linear detector array, which enables recording of one cross-track line of an image at once (Figure 1.12b). The image formation is solely based on the forward, along-track movement of the sensor. The advantage of pushbroom scanners is that they allow a longer integration time and therefore the sensors receive a stronger signal in comparison with whiskbroom scanners. Since an array of detectors is used, the major drawback is that the detectors can have varying sensitivity and therefore a perfect, uniform calibration of the detectors response is critical. Airborne imaging spectrometers using the pushbroom scanning principle are e.g. AISA, APEX and CASI. Examples of thermal sensors are TASI and AISA Owl.

The operational principle of the laser scanning is however totally different. A laser scanner emits its own light pulses and records travel time from the instrument to the ground surface and back, as well as the intensity of reflected signal. Details on laser scanning are further discussed in Chapter 4.

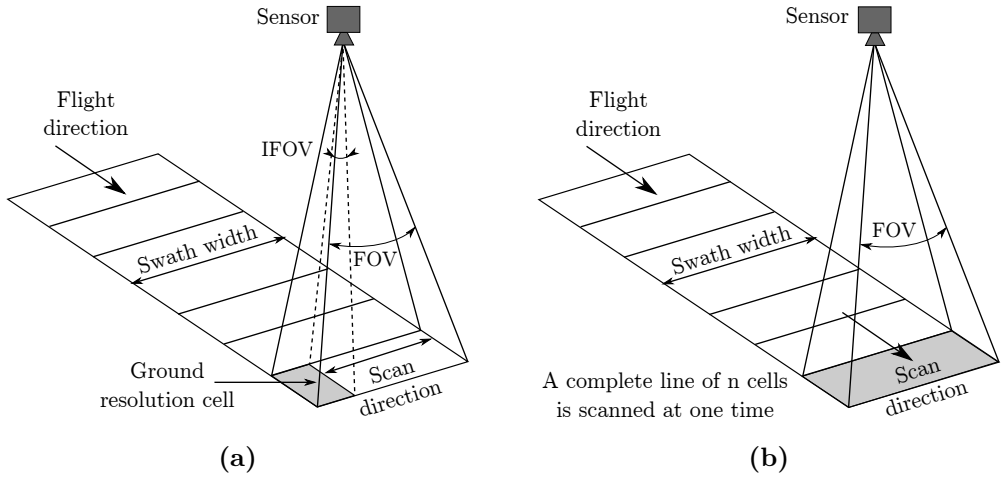

Figure 1.12 Whiskbroom (a) and pushbroom (b) scanning concept used for airborne hyperspectral remote sensing. (IFOV – instantaneous field of view, FOV – field of view)

Resolutions of a digital RS imager

Quality and information content of RS data are determined by the resolutions of a RS system. When speaking about resolution, most people would think about spatial resolution only. The other types of resolution – radiometric, spectral and temporal, however, are equally important. In a broad sense, resolution of a digital RS system can be understood as its ability to resolve the smallest possible detail in signal variation.

Radiometric resolution is the ability of an imaging system to record smallest change in the signal intensity level. The intrinsic radiometric resolution of a RS system depends on the signal-to-noise ratio and it is further determined by the digital coding, i.e. how many bits are used to digitize the continuous intensity values.

Spectral resolution refers to the ability of an instrument to resolve features in the electromagnetic spectrum. Spectral resolution is usually described by the full width at half maximum (FWHM) and sampling interval. FWHM is an interval measured at the level where the instrument's spectral response reaches half of its maximum value (Figure 1.13). The same figure illustrates the spectral sampling interval which is the distance between peaks of two adjacent spectral bands.

Spatial resolution of an imaging sensor is defined as the size of the smallest object that can be resolved on the ground. This is primarily determined by instantaneous field of view (IFOV) of a sensor (Figure 1.12a). IFOV refers the ground area viewed by a single detector element and, if measured in terms of the "footprint" on the ground (it can also be measured by solid angle) it varies with the flight altitude. The terms spatial resolution and pixel size are often used interchangeably, but in reality, they are not quite the same. Image data can be

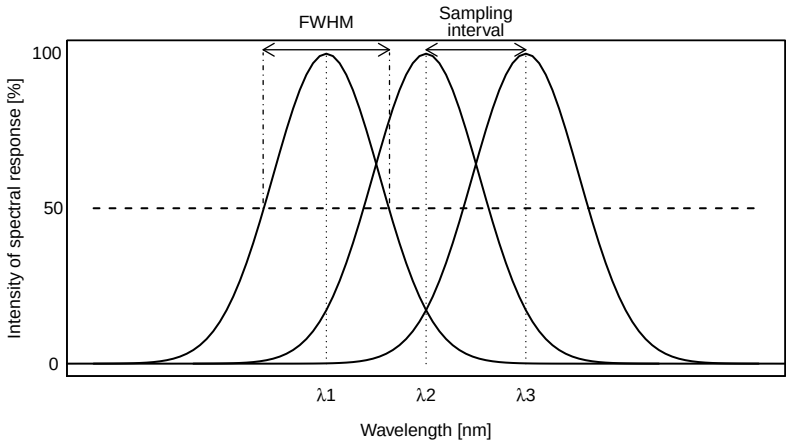

Figure 1.13 Illustration of full width half maximum (FWHM) and spectral sampling.

aggregated so that a pixel size represents an area larger than IFOV, i.e. larger than the actual spatial resolution of a sensor. However, in raw data it is not possible for pixels to get information about areas smaller than IFOV Figure 1.14 illustrates how an image subset of the original spatial resolution of 0.4 m is resampled to coarser pixel sizes.

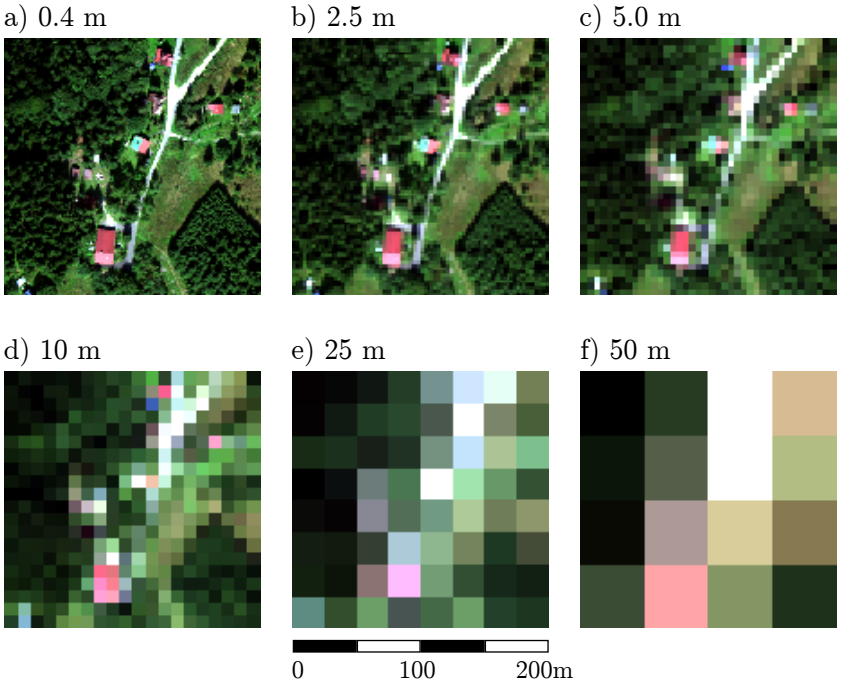

Figure 1.14 A contrived example in which an image subset (with the original pixel size of 0.4 m) has been degraded by averaging adjacent pixels into increasingly larger blocks.

For the sake of completeness, we also mention temporal resolution (or revisit time), which is defined as time elapsed between two consequent image acquisitions of the same point on the Earth. Temporal resolution is somewhat irrelevant in airborne RS as the date of image acquisition is usually determined by a user or an operator. However, for satellite-based RS data it is an important characteristic.

Ancillary onboard and field measurements

Each airborne image acquisition, irrespective of it concerns hyperspectral, thermal or laser scanning, has to be accompanied by series of ancillary onboard measurements. Some supportive field measurements can be required too. Most important, and the de facto standard onboard measurements, are the measurements carried out by an IMU/GNSS unit during an overflight. The unit records exact position, altitude, speed and angular changes (pitch, roll and heading) of the aircraft. This information is used for geometric corrections of airborne hyperspectral, thermal, as well as laser scanning data as it compensates for geometric distortions caused by variations in the aircraft's orientation and trajectory during the scanning.

Another type of onboard measurement, potentially useful but less often employed in practice, is the characterization of the varying atmospheric conditions during the flight. This can be done by synchronous measurements of downwelling solar irradiance reaching the aircraft level. This information can be potentially used for rapid, but less accurate atmospheric corrections of airborne hyperspectral imagery (Choi & Milton 2001).

In cases where precise calibration and correction of remotely sensed hyperspectral or thermal image data is required, it is necessary to carry out supportive field measurements. Additional data on surface reflectance, geometric accuracy of selected ground control points and atmospheric conditions shall be measured simultaneously, or as close as possible, to RS acquisition. Figure 1.15 illustrates different types of ancillary field measurements.

Field measurements of reflectance properties of natural and artificial surfaces support the processing of airborne hyperspectral imagery. Field reflectance spectra are used as essential inputs for empirical, as well as physically-based approaches to remove the effect of the atmosphere (more details on this can be found in Chapter 2). Furthermore, they can be used to verify the quality of atmospheric corrections. Field reflectance spectra are measured by field spectrometers and some commonly used instruments are for example FieldSpec models produced by ASD Inc. (Figure 1.15a) or instruments from Spectra Vista Corporation and Ocean Optics. When performing the field reflectance measurements, one should select surfaces that are: i) homogenous in terms of spectral variations from pixel to pixel, ii) large enough to be identified in the acquired airborne image, iii) represent the brightness diversity of the imaged area (at least one dark and one bright target should be used), and iv) spectrally flat and lambertian. Interested

readers can find more details on field reflectance measurements in Milton (2009) and McCoy (2004).

Precise geometric location of ground control points (GCPs) measured by a GNSS system have dual uses in processing of any kind of remotely sensed data. First, they serve to precisely georeferenced the image data, i.e. to adjust an image to a known coordinate system. Second, it allows evaluating the accuracy of the image georeferencing by calculating the root mean square error between actual positions of GCPs and their calculated position on the image after georeferencing. That is why the GCPs should be easily identified on the images (e.g. a road crossing, an edge of a parcel) and spread evenly across the imaged area. Meeting the later condition is becomes obligatory especially when higher polynomial transformation is being used for georeferencing.

Characterisation of the atmospheric conditions at the time and location of the flight is important as this information can be used to improve atmospheric corrections of hyperspectral and thermal imagery (Richter & Schläpfer 2002). Most often, ground-based multi-band devices called sun photometers are used to estimate aerosol optical thickness and water vapour content. Examples of frequently used sun photomters are Microtops II (Solar Light Company, USA, Figure 1.15c) or Cimel (Cimel Electronique S.A.S, Fr).

(a) **(b)** **(c)**

Figure 1.15 Ancillary ground measurements of (a) surface reflectance properties (ASD Field Spec-3), (b) location of geometric ground control points (TOPCON), (c) atmospheric characterisation (Microtops II).

Recommended Reading

Campbell, J.B. & Wynne, R.H. 2011. *Introduction to remote sensing (5^{th} edition).* The Guilford Press, 72 Spring Street, New York NY 10012.

Lillesand, T.M. & Kiefer, R.W. 2000. *Remote Sensing and Image Interpretation (4^{th} edition).* John Wiley & Sons, Inc., New York.

Rees, W.G. 2012. *Physical Principles of Remote Sensing (3^{rd} edition).* Cambridge University Press.

2

HYPERSPECTRAL DATA

Lucie Homolová, Jan Hanuš, Tomáš Fabiánek, and František Zemek

2.1 Characteristics of Hyperspectral Data

Hyperspectral remote sensing or imaging spectroscopy, a synonym that is extensively being used in scientific literature, is a rapidly developing field of remote sensing (Ustin et al. 2004; Kokaly et al. 2009; Schaepman et al. 2009). What makes hyperspectral RS so specific is that it uses the practice of spectroscopy to acquire images in a large number of narrow, adjacent spectral bands. Compared to broadband multispectral RS, hyperspectral data contain typically hundreds of narrow spectral bands (typically 1–10 nm in width) such that for each pixel a continuous spectral signature over a certain range of wavelengths can be derived. Figure 2.1 shows the contrast between a continuous spectral signature of vegetation acquired by a hyperspectral instruments and spectral responses of three commonly used multispectral RS instruments – MODIS, Landsat TM and Spot 4. In general, airborne imaging spectrometers differ from other RS instruments in terms of their exceptionally fine spectral, spatial and radiometric resolutions and their need for careful calibration.

The concept of spectroscopy has existed since eighteen century, but the imaging part of this became technically possible only in early 1980's. Figure 2.2 illustrates the generalized concept of imaging spectroscopy. A hyperspectral image is represented as a three-dimensional data cube, a series of superimposed image

layers, where each layer carries information about surface reflectance at an individual wavelength interval.

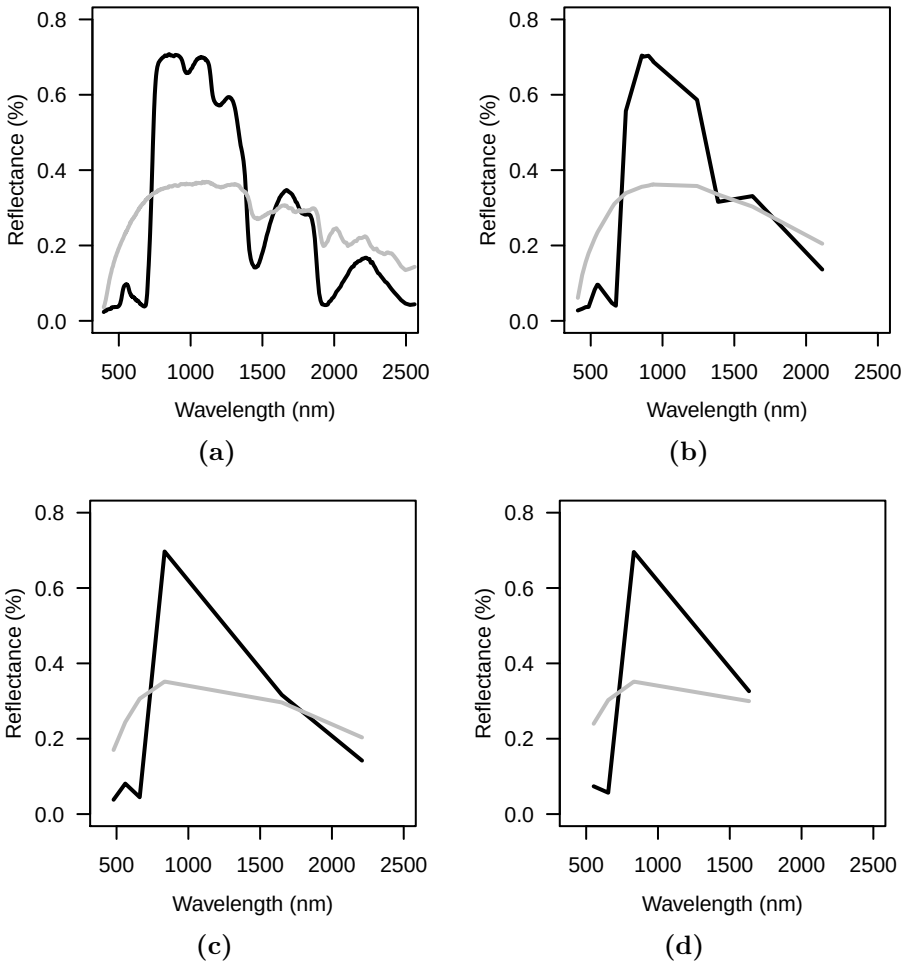

Figure 2.1 Spectral signature of fresh (black line) and dry (grey line) vegetation as derived from (a) laboratory spectroradiometer (USGS database) resampled to the spectral resolution of (b) MODIS, (c) Landsat TM, (d) Spot 4 remote sensing instruments.

2.2 Overview of Airborne Hyperspectral Sensors

Ongoing development of imaging spectroscopy since 80's resulted in many research prototypes, as well as many commercially available airborne hyperspectral sensors. Currently only tree spaceborne instruments can provide truly hyperspectral data. They are Hyperion on EO-1 (Pearlman et al. 2003), CHRIS on PROBA (Barnsley et al. 2004), and Resurs-P (Kirilin et al. 2010). In Table 2.1 we

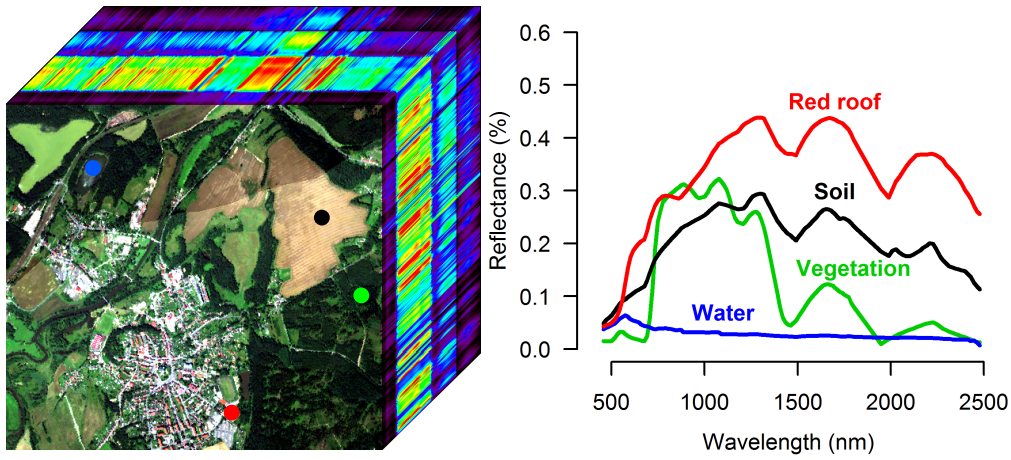

Figure 2.2 The concept of imaging spectroscopy illustrated with a HyMap image scene from the region of Sokolov displayed as a hyperspectral cube. The top most layer represents a three-band colour composite ($R = 646.5\,\text{nm}$, $G = 543.6\,\text{nm}$, $B = 455.4\,\text{nm}$). The depth of the cube represents the spectral dimension, which displays as contiguous spectral signatures, as depicted on the right graph. Colour dots on the left image indicate from where the spectral signatures for vegetation, soil, water and roofing material were extracted for the purposes of demonstration.

present an overview of currently operational airborne hyperspectral instruments. Airborne imaging spectrometers that are nowadays rarely used are deliberately omitted, although we have to acknowledge several key projects that have had an impact on the evolution of the state-of-art imaging spectrometers. These include: AIS - Airborne Imaging Spectrometer - the precursor of the AVIRIS instrument developed by the NASA Jet Propulsion Laboratory (Vane et al. 1984); FLI/PMI instrument that can be considered the precursor of CASI (Gower et al. 1992); ROSIS - an airborne forerunner instrument for the spaceborne MERIS mission developed by DLR (Kunkel et al. 1991), and some others. For further reading about the evolution of imaging spectrometers we refer the reader to Schaepman (2009).

The current trend indicates that hyperspectral instruments are becoming more commercially available. They are also getting smaller, allowing them to be carried by small unmanned airborne vehicles (Micro-Hyperspec system from Headwall Photonics, Cubert's UHD 185 system, Pika system from Recon and many others).

At the moment, the only provider of high quality airborne hyperspectral data in the Czech Republic is CzechGlobe. CzechGlobe operates AISA Eagle (a VNIR system developed by Specim, Ltd.) and three instruments (CASI, SASI and TASI developed by ITRES, Ltd.). The suite of Itress instruments covers the entire

optical, as well as the thermal infrared domain. At CzechGlobe all sensors are integrated into an airborne carrier Cessna 208B Grand Caravan equipped with two fuselages slits. The entire imaging system at CzechGlobe is called FLIS (Hanuš et al. 2014).

2.3 Basic Pre-processing of Hyperspectral Data

In the context of hyperspectral data analysis, the pre-processing steps usually refer to three major operations. These are: i) radiometric corrections that convert raw DN values into at-sensor radiance values, ii) atmospheric corrections that remove the effect of the atmosphere and convert at-sensor radiance to at-surface reflectance or brightness temperature values, and iii) geometric corrections that compensate image distortions caused by the aircraft movements and bring an image into registration with a map or another image. All three steps are usually accompanied with some quality assessment.

Especially for research purposes, excellent sensor calibration and image corrections are ultimately required. In this case, it is necessary to carry out supportive ground measurements, where additional data on surface reflectance, geometric accuracy of selected ground control points and atmospheric conditions are measured simultaneously to RS data acquisition. If feasible, each airborne campaign shall be accompanied with supportive field measurements. However, this is not always possible and for those applications where the radiometric quality of RS data is not of the highest priority it is possible to perform simplified atmospheric corrections, i.e. by calculating so called apparent reflectance.

The image data pre-processing is usually carried by the institute that operates an imaging spectrometer. In most cases, end users are provided with geometrically corrected at-surface reflectance data or at-sensor radiance together with the sensor characteristics needed for further analysis. It should be mentioned here that, although certain pre-processing steps are frequently used, there is no definitive standard pre-processing chain available for hyperspectral RS data. Often, the pre-processing steps have been tailored to a certain instrument or to match specific requirements of a project. It is also often the case that each data provider developed its own pre-processing chain using commercial and/or in-house tools and software. The following sections will introduce a processing chain that includes radiometric, atmospheric and geometric corrections of hyperspectral RS data as they are currently being implemented at CzechGlobe. Figure 2.3 shows a schematic workflow of the pre-processing chain for CASI hyperspectral data at CzechGlobe. The workflow for TASI has not yet been fully established.

2.3.1 Radiometric Calibration

Incoming radiation from a surface reaching an airborne imaging spectrometer is split by a set of lenses and filters into the wavelength ranges specified by the

Table 2.1 Overview of currently operational airborne hyperspectral sensors in the reflective domain.

Name	Full name	Max. No. of bands	Spectral range (nm)	Spectral sampling (nm)	Manufacturer/Operator (Information source)
AHS 80	Airborne Hyperspectral Scanner	80	441–13170	30–500	Argonst (formerly SenSyTech inc., Daedalus inc.)/ e.g. INTA (`http://www.uv.es/~leo/sen2flex/ahs.htm`)
AISA Dual (Eagle/Hawk)	Airborne Imaging Spectrometer for Applications	488/254	400–970/ 970–2500	1.2–9.2/6.3	Specim Ltd./ e.g. NERC, Univ. of Debrecen, CzechGlobe (Eagle only) (`http://specim.fi/index.php/products/airborne`)
APEX	Airborne Prism EXperiment	334	380–2500	0.6–10	ESA (Swiss-Belgian consortium)/ Vito (`http://www.apex-esa.org/`)
AVIRIS	Airborne Visible InfraRed Imaging Spectrometer	224	400-2500	10	NASA, JPL/ NASA, JPL (`http://aviris.jpl.nasa.gov/`)
CASI/SASI	Compact/SWIR Airborne Spectrographic Imager	288/100	365–1050/ 950–2450	3.5/12	Itres Ltd./ CzechGlobe (`http://www.itres.com/products/imagers`)
HyMap		128	450–2500	15–20	Integrated Spectronics Pty Ltd / HyVista Corp.
HySpex VNIR/SWIR		160/256	400–1000/ 1000–2500	3.7/6	NEO/ e.g. DLR (`http://www.hyspex.no/products/`)
PRISM	Portable Remote Imaging SpectroMeter	85+2	350–1050 + 1240–1610	2.8 + n.a.	NASA, JPL/ NASA JPL (`http://prism.jpl.nasa.gov`)

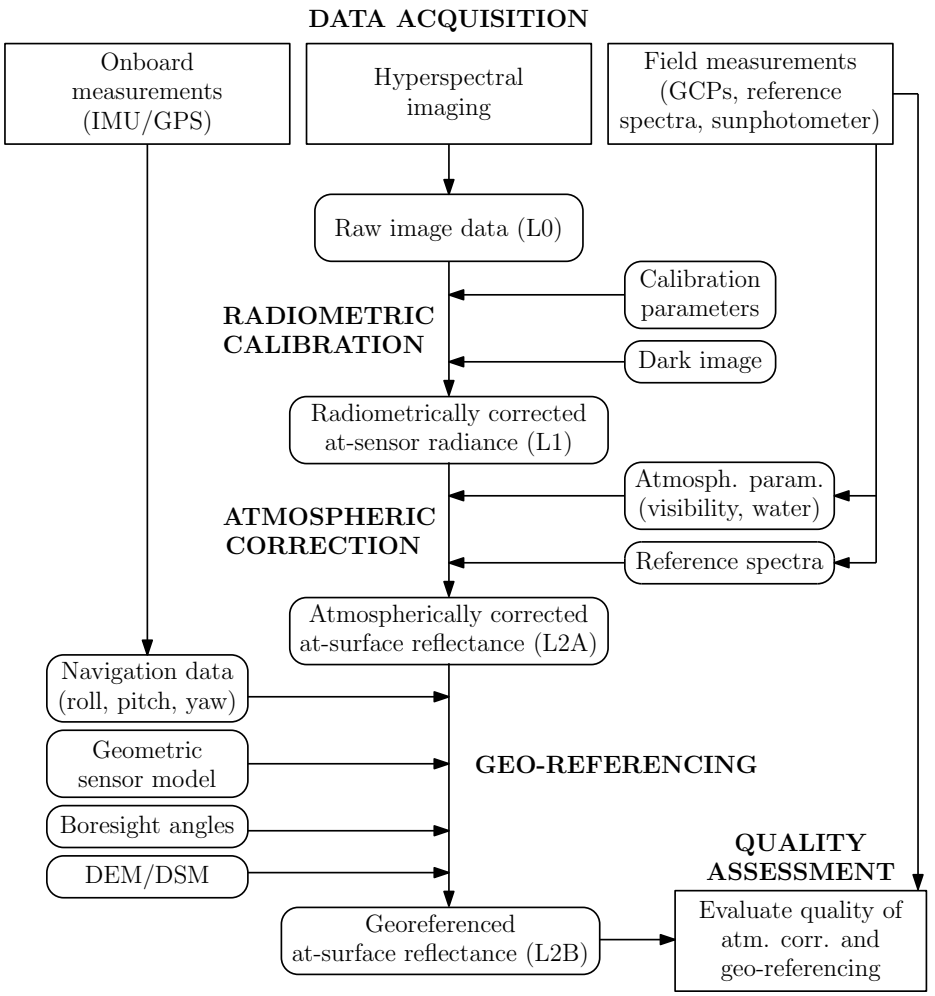

Figure 2.3 Pre-processing chain for airborne hyperspectral data.

instrument. The signal charges accumulated on the detector elements are passed through an amplifier and a digitizer. A digital signal (digitized in 8, 12 or 16 bits) is directly proportional to the incoming photon energy, but not measured in any physically meaningful unit. It is expressed in digital numbers (DN). Therefore a radiometric correction has to be applied in order to convert raw DN values into a physically meaningful parameter – spectral radiance expressed as photon flux power per unit solid angle per wavelength interval (cf. Figure 2.4a and b). At-sensor spectral radiance L is calculated from raw DN values using given calibration gain and offset values as follows:

$$L = C_0 + C_1 \mathrm{DN}. \tag{2.1}$$

The gain (C_1) and offset (C_0) values are parameters of a radiometric response function that is empirically established for each spectral band. The radiometric response function is established during radiometric calibration. Radiometric calibration is a process where a sensor measures a signal originating from a light source with known spectral radiance in an integrating sphere (Figure 2.5).

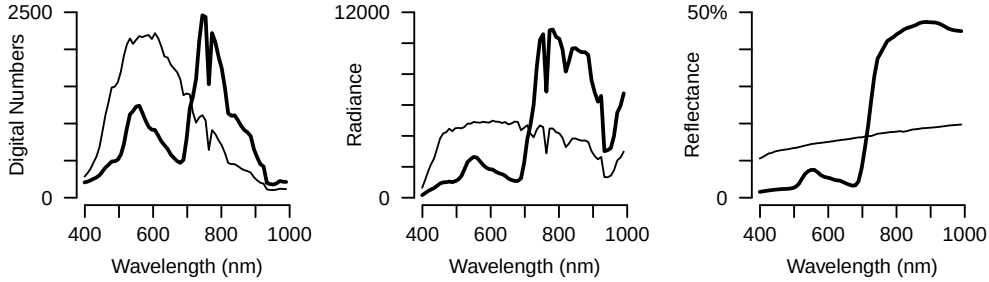

(a) **(b)** **(c)**

Figure 2.4 (a) Raw digital numbers (unitless), (b) Radiance ($\mathrm{mW\,cm^{-2}\,sr^{-1}\,nm^{-1}}$), (c) Reflectance (%) signatures of vegetation (thick line) and asphalt (thin line) surfaces as obtained from AISA Eagle spectrometer.

2.3.2 Atmospheric Corrections

The signal that is recorded by an imaging spectroradiometer is strongly influenced by scattering and absorption in the atmosphere of the radiation reflected or emitted by the surface (see Chapter 1). Influences of water vapour absorption at approximately 0.94, 1.14, 1.38 and 1.88 µm, of oxygen at 0.76 µm, and of carbon dioxide near 2.08 µm are clearly seen in the radiance spectrum. Wavelengths below 1 µm are affected by molecular and aerosol scattering. Moreover, the total radiation signal reaching a sensor (L) consists of three components (Figure 2.6): i) path radiance – photons reaching senor's IFOV without having been in contact with ground (L_1), ii) reflected radiation from a pixel (L_2), and iii) reflected radiation from the neighbourhood (L_3).

As the majority of RS applications are based on at-surface reflectance, where results from different sites, sensors and acquisition times are compared, it is necessary to remove unwanted atmospheric effects. This process is called atmospheric correction and it converts at-sensor radiance to at-surface reflectance (cross-compare a raw signal with at-sensor radiance and surface reflectance shown at Figure 2.4). We wish to clarify at this point that the term "reflectance" in this book is used in a common sense and for a review on different reflectance quantities we refer curious readers to a review of Schaepman-Strub et al. (2006). Atmospheric corrections algorithms can be divided into two major groups: empirical methods that produce apparent reflectance, and methods based on rigorous atmospheric radiative transfer modelling that produce absolute reflectance. A very

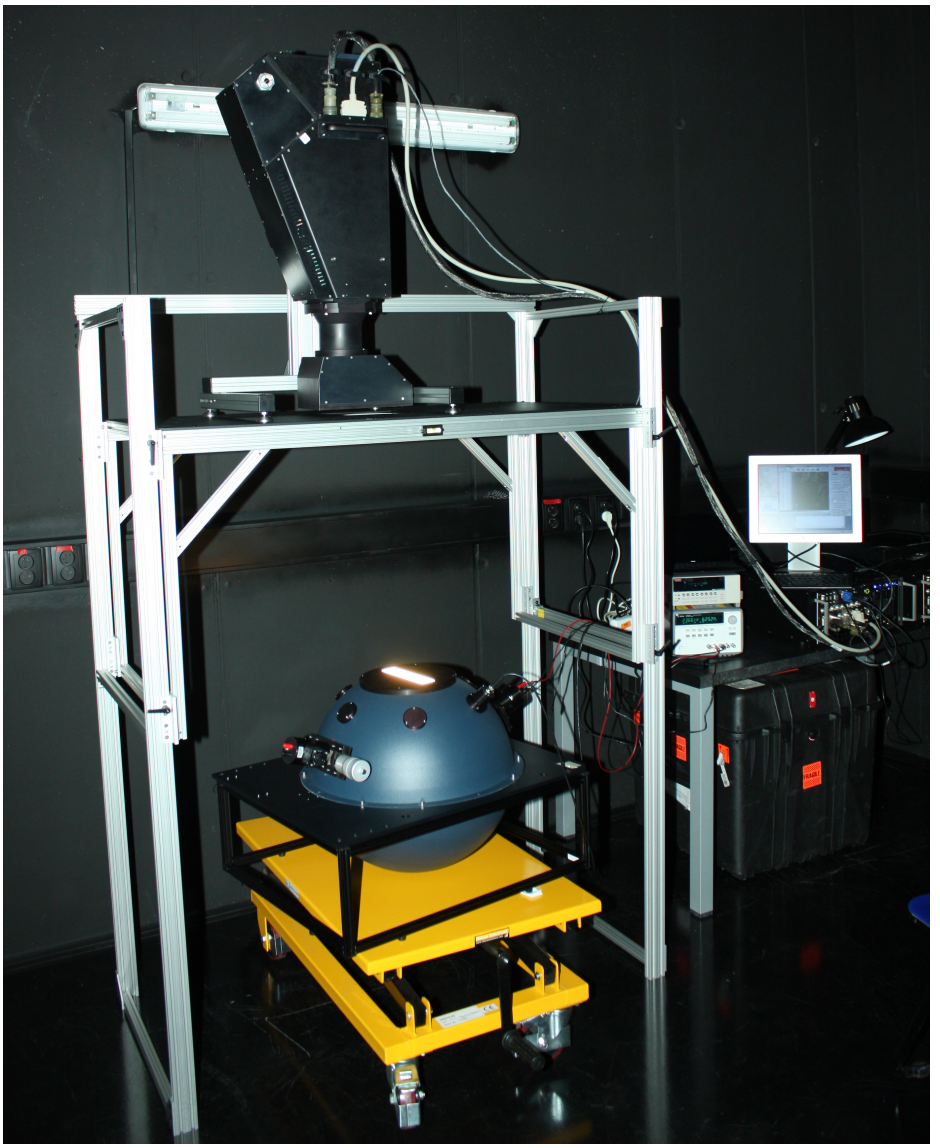

Figure 2.5 Example of a calibration facility at Czechglobe. Calibration of a hyperspectral sensor (mounted on the top of the frame) using an integration sphere from LabSphere©.

good review of existing atmospheric correction approaches is given in Gao et al. (2009) and here we briefly introduce the two groups.

Empirical approaches

Empirical atmospheric correction approaches produce apparent reflectance that is relative to a standard target from the image scene. Several methods have been developed, some of them specifically targeting water or land surfaces. For land

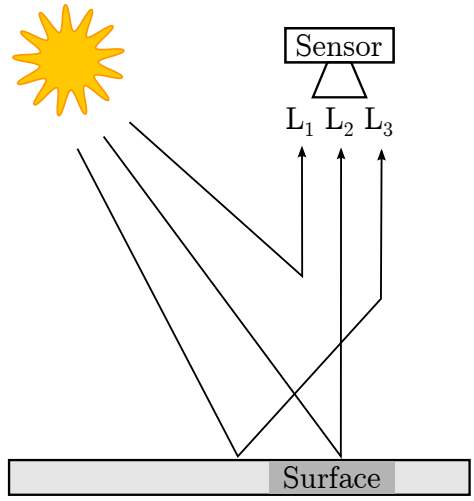

Figure 2.6 Schematic sketch of solar radiation components in flat terrain conditions. L_1 = path radiance, L_2 = reflected radiance, L_3 = adjacency radiance.

surfaces, some of the empirical corrections are: Flat Field correction (FF), Internal Average Relative Reflectance method (IARR), and Empirical Line correction (EL). Taking the case of the Empirical Line correction, the method forces the image radiance (or DN) data to match selected field reflectance spectra. This method requires at least one bright target and one dark target to establish a linear regression between the field measured reflectance spectra and corresponding image data. Gains and offset values are retrieved for each spectral band and applied to the entire image scene. The EL method produces spectra that are most comparable to reflectance spectra measured in the field and locally it is very effective. However, if the atmospheric conditions changes outside the area with ground reference targets, the reflectance calculation is less accurate and will contain atmospheric features. The EL method ultimately requires simultaneous measurements of ground reflectance on carefully selected, homogenous reference targets, which is not the case for the other two (i.e. FF, IARR).

Another example of fast empirical atmospheric corrections, where field data are not required, is the calculation of apparent at-sensor reflectance. In this case, the image data are normalized to the downwelling solar irradiance incident at the aircraft level. The incident solar irradiance is recorded simultaneously with image acquisition using a diffuse cosine receptor. This rapid correction normalizes the signal differences between flight lines and removes the atmospheric effects above the aircraft level. Depending on the flight altitude and current atmospheric situation, the at-sensor apparent reflectance can be to smaller or larger extent still influenced by the atmosphere below an aircraft.

Radiative transfer modelling approaches

Atmospheric corrections based on radiative transfer model (RTM) allow calculation of absolute at-surface reflectance without a-priori knowledge of surface reflectance properties. Atmospheric corrections consist of two major steps: estimation of atmospheric parameters and retrieval of surface reflectance. The most important atmospheric parameters are aerosol type, visibility (or optical thickness) and water vapour, because they vary in time and space rapidly. Visibility and water vapour can be measured in-situ using a sunphotometer (Figure 1.15c in Chapter 1) or they can be estimated directly from the image data. Retrieval of surface reflectance is most commonly done using the look-up table method, in which an RTM is used to pre-compute atmospheric transmittance for each wavelength and for given combination of key atmospheric parameters and operational altitudes. Assuming flat terrain without adjacency effects and cloud-free sky, the at-sensor radiance (L) for surface reflectance (ρ) at given wavelength λ can be expressed as follows:

$$L = L_{path} + \frac{\rho \tau E_g}{\pi}, \tag{2.2}$$

where L_{path} is path radiance (equivalent to L_1 at Figure 2.6), τ is total ground-to-sensor atmospheric transmittance calculated as the sum of direct and diffuse transmittance, E_g is global ground irradiance calculated as sum of direct and diffuse irradiance for a ground surface with zero reflectance. Detailed description of atmospheric radiative transfer, estimation of atmospheric parameters and atmospheric corrections are beyond the scope of this chapter, however, interesting readers are referred to e.g., Richter & Schläpfer (2002), Richter (2012) or Gao et al. (2009).

The individual radiation components of eq. 2.2 and total atmosphere transmittance are calculated by an atmospheric RTM. Two RT models commonly employed for atmospheric corrections of airborne imaging spectroscopy are MODTRAN and 6S. MODTRAN, the latest release being MODTRAN-5 (Berk et al. 1989; Berk et al. 2006), is more widespread, although a comparison of both models has indicated some major advantages of the 6S vector version (Kotchenova et al. 2006) due to its support of polarisation effects. These two models serve as basis for many software toolboxes developed for atmospheric correction of airborne hyperspectral imagery. An overview of some tools for atmospheric corrections based on RTM is given in Table 2.2. Some of these tools include more advanced features, e.g. ATCOR-4 (Richter, (2012) offers additional corrections for nadir normalization and BRDF correction.

2.3.3 Geometric Pre-processing

Data image acquisition from an airborne platform is never as stable as acquisition from a satellite platform. Airborne hyperspectral data suffer from spatial distortions that can be so severe that they cannot be used directly as a map base

Table 2.2 Overview of tools for atmospheric corrections of airborne hyperspectral for land applications.

Name	Development Team	Reference	RTM	Use
ACORN (Atmosphere CORection Now)	ImSpec LLC, USA	(Kruse, 2004) `http://www.imspec.com`	MODTRAN-4	Commercial
ATCOR (Atmospheric and Topographic CORrection)	German Aerospace Centre & ReSe Applications Schläpfer	(Richter & Schlapfer, 2002) `http://www.rese.ch/products/atcor/atcor4/`	MODTRAN-5	Commercial
ATREM (ATmospheric REMoval algorithm)	Uni. of Colorado, Boulder, USA	(Gao et al. 1993)	HITRAN and 6S	Research (no more support)
FLAASH (Fast Line-of-sight Atmospheric Analysis of Spectral Hypercubes)	Air Force Phillips Laboratory, Hanscom AFB & Spectral Sciences, Inc., USA	(Adler-Golden et al., 1999)	MODTRAN-4	Commercial (distributed with ENVI)
HATCH (High-accuracy Atmospheric Correction for Hyperspectral data)	Uni. of Colorado, Boulder, USA	(Qu et al. 2003)	HITRAN & own RT algorithm	Research, licence agreement

without any pre-processing. The sources of geometric distortions are a sensor's inherent geometric characteristics, the aircraft motions during the data acquisitions and terrain variations. Such distortions cannot be easily corrected using ground control points, since the aircraft movements cannot be approximated accurately by polynomial transformation of the image. Therefore geometric pre-processing of airborne hyperspectral data is done in more sophisticated way when line- or even pixel-wise calculation has to be performed.

Fortunately, aircrafts are nowadays equipped with an onboard IMU/GNSS system that records instantaneous position of the aircraft (longitude, latitude and altitude) and its movement (roll, pitch and heading angles). This data, together with sensor geometric characteristics (e.g. field of view, swath width) and a digital terrain model, are key input data for geometric pre-processing of airborne hyperspectral data. Geometric pre-processing (or geo-referencing) is performed in two successive steps, direct geocoding and resampling to a selected coordinate system.

Direct geocoding of airborne images consists of geometric corrections and orthogonalization. Geometric corrections compensate for image geometric distortions caused by variations in flight path and attitude of a plane. Orthogonalization compensates distortion caused by sensor acquisition geometry and surface topography. The coordinates of each pixel of the hyperspectral image are determined as if on a flat terrain.

During the resampling the image data are transformed to a regular grid of the reference frame (i.e. a desired coordinate system such as UTM map projection). In this step, a desired spatial resolution and a method for interpolation have to be selected. Examples of well-known and commonly used interpolation methods are nearest neighbour, bilinear or cubic interpolation. Among these, only the nearest neighbour interpolation preserves the original spectral data. With other interpolation methods the new value of a resampled pixel is calculated as some combination of its surrounding pixels. For airborne hyperspectral RS, a paradigm so far has been to avoid as much as possible interpolated spectra in order to preserve the physical meaning of spectral signatures for classification and quantitative analysis.

Software tools for geometric pre-processing of hyperspectral airborne data are usually supplied by a sensor producer (e.g. CaliGeo for processing of AISA images developed by Specim Ltd, GeoCorr supplied by ITRES, Ltd. for processing of image data from a suite of their sensors). An example of a commercially available tool for complex geometric pre-processing of commonly available airborne imaging spectrometers (Table 2.1) is the PARGE software (Schläpfer & Richter 2002).

2.3.4 Quality Assessment

More and more remote sensing applications and data users require information about the quality of hyperspectral data. This information is highly important

when data from multiple sources or multiple acquisitions are analysed together. Quality assessment of hyperspectral data is highly dependent on several factors and parameters. Each stage of the data pre-processing chain can be characterised by quality indicators. The quality indicators can be calculated for the entire image area or on the pixel-basis.

The most important indicator of the radiometric quality is the signal-to-noise ratio (SNR). The SNR of a sensor is specified as a ratio value and for modern hyperspectral instruments the producers declare up to 1000:1 (theoretical maximum). However, practical values of SNR are usually lower (e.g. 10:1 to 300:1), especially for surfaces and wavelength regions with low reflectance.

The quality of atmospheric corrections can be evaluated by means of independent ground reference spectra measured simultaneously with image acquisition. The reference targets have to be precisely located on the images and the reference spectra are compared with spectral signatures extracted from the image data. Spectra can be compared visually or by calculating root mean square error between the two. It is very hard to provide one objective number, but as a rule of thumb, RMSE below 2 % is excellent, and 5 % can be considered as a satisfactory accuracy (Richter & Schläpfer 2002).

Geometric quality of hyperspectral data can be evaluated by calculating horizontal accuracy using a set of independent GCPs. The horizontal accuracy is mainly influenced by the resolution and the accuracy of underlying DEM used during geometric pre-processing. In the ideal case, when all ancillary data (navigation data and DEM) are available and of high resolution, we can reach the horizontal accuracy equal to the size of a pixel.

Furthermore, during the pre-processing chain, pixel-based quality flags can characterize bad pixels, such as pixels with saturated signals, areas influenced by clouds, haze and cloud shadows.

Doporučená literatura

Liang, S. 2004. *Quantitative remote sensing of land surfaces.* Hoboken, New Jersey: John Wiley & Sons, Inc.

Gao, B.-C., Montes, M.J., Davis, C.O. & Goetz, A.F.H. 2009. Atmospheric correction algorithms for hyperspectral remote sensing data of land and ocean. *Remote Sensing of Environment* 113, *Supplement* 1, S17—S24.

Schaepman, M.E. 2009. Imaging Spectrometers. In T.A. Warner, M. Duane Nellis, & G.M. Foody (Eds.), *The SAGE Handbook of Remote Sensing* (pp. 166–178). London (UK): SAGE.

3

THERMAL DATA

Jakub Brom, Marek Pivovarník, Petra Hesslerová, Václav Nedbal, Vladimír Jirka, Hana Vinciková, Jan Procházka, and Petr Lechner

Airborne thermal data offers valuable information about land surfaces resulting in many applications in different fields such as energy balance, evapotranspiration, water temperature assessment, vegetation applications, mineral mapping, urban studies, volcano surveillance, landmine fields mapping, drainage system detection, archaeological studies and others. It is important to realize that data obtained from airborne thermal instruments can be interpreted and analysed in two ways. First, only the visual information is analysed, (e.g. thermovision cameras employed to search for missing people, detection of specific phenomena and objects). Second, the radiometric information content allowing quantitative analysis of temperature and spectral properties is considered. One of the applications focusing on landscape thermal regime is described in detail in Chapter 10. The core analyses of thermal data are related to object detection and quantification of temperature and spectral features.

In order to interpret thermal data correctly, it is necessary to understand their characteristics and related principles of data acquisition. These topics are briefly discussed in the following sections. In addition, an overview of currently available instruments with their specifications is provided. The references, in which readers can find more details, are attached at the end of this chapter.

3.1 Thermal Data Characteristics

Every object emits electromagnetic energy. The amount and the spectral distribution of the emitted energy depend on the object's temperature and emissivity. In the case of an ideal blackbody the amount and spectral distribution of emitted energy are described by Planck's law (see Section 1.2.2). Most natural and artificial objects that can be observed using airborne RS have temperatures in the range of 270–330 K. According to the Planck's law this means that the bulk of thermal radiation can be detected in two atmospheric windows 3–5 µm and 8–14 µm. In the first interval not only emitted radiation is recorded but also reflected solar radiation. Therefore, these data are usually acquired at night, when the reflected radiation is minimized. The second atmospheric window is more relevant for acquisition of remotely sensed thermal data, since the peak of emitted radiation is situated here (a consequence of the Wien's displacement law as described in 1.2.2). Further on we will discuss only the emitted thermal radiation in the second atmospheric window.

An image taken in the thermal part of the EM spectrum is either known as a thermogram in which case each pixel contains only a single value registering the intensity of thermal radiation at that location, or a thermal hyperspectral cube (Figure 2.2) in which case each pixel contains a spectral record. If thermal image data are well corrected, they can be used for creation of temperature maps. Unlike conventional field measurements, which provide point temperature information, airborne thermal data are spatially continuous. This information may be qualitative (for comparisons) and quantitative in nature (for getting absolute values). For qualitative purposes, atmospheric corrections of thermal imagery data are not necessary. However, in case of quantitative analyses an accurate instrument calibration, geometrical and atmospheric corrections are ultimately required (further discussed in Section 3.3). In order to perform radiometric calibration and atmospheric corrections correctly one has to understand the radiative transfer equation as described below.

3.1.1 Properties Determining the Thermal Radiation of an Object

From the perspective of RS, the most important thermal property of an object is emissivity (ε). The principle of emissivity and some examples of emissivity spectral curves can be revisited in Chapter 1. In short, ε can be understood as thermal radiation emission effectiveness in comparison with thermal radiation emitted by a blackbody of the same temperature. Emissivity in general depends on wavelength, temperature and on the direction of the emission. Since in remote sensing an observed object's temperature mostly varies within the range of 270–330 K and the observation angle is close to nadir, it can be assumed that ε depends on the wavelength mainly.

In general, when acquiring thermal RS data, one shall consider actual weather condition, season and daytime as all these influences thermal properties of an object. Besides emissivity, the following thermal properties can cause variation in thermal image data. These are:

- thermal conductivity is a measure of the rate at which heat passes through a material; i.e. an ability to conduct heat [$\mathrm{W\,m^{-1}\,K^{-1}}$];
- thermal capacity determines how well a material stores heat, i.e. an ability to retain warmth [$\mathrm{J\,K^{-1}}$];
- thermal inertia is a measure of the response of a material to temperature changes, i.e. the rate of the temperature change [$\mathrm{J\,m^{-2}\,K^{-1}\,s^{-1/2}}$].

Moreover, additional thermal properties can be used for different applications, such as a building up a relationship of thermal inertia and soil moisture (Maltese et al. 2013).

3.1.2 Surface Thermal Behaviour as a Result of Energy Transformations

The thermal behaviour of a surface can be perceived as a thermodynamic state of that surface, as well as a result of energy transformations taking place at the surface. Changes in surface temperature are due to exchanges of radiation between surface, its surroundings and conduction of the heat to the ground. This influences the amount of energy entering the system (a surface), as well as amount of energy leaving the system. Under normal conditions in nature the formation of surface temperature mostly involves energy transformation during the phase changes of water (water condensation and evaporation, water thaw and freezing, water sublimation and desublimation) as well as the body heat flux, to a certain degree.

In order to explain and to understand changes in surface temperature, we need to start with the radiation balance equation:

$$R_n = R_s^{\downarrow} - R_s^{\uparrow} + R_l^{\downarrow} - R_l^{\uparrow}. \tag{3.1}$$

The equation expresses the balance of energy inputs entering into and outputs leaving from a natural system in the form of the short-wave (R_s) and long-wave (R_l) EM radiation. The source of short-wave radiation is the Sun ($R_s^{\downarrow}$) and a certain portion of incoming short-wave radiation is reflected upon incidence ($R_s^{\uparrow}$). The long-wave radiation balance is given by the energy radiation emitted in the thermal infrared part of the electromagnetic spectrum from the Earth surface ($R_l^{\uparrow}$) and atmosphere ($R_l^{\downarrow}$). The result of radiation balance represents the so called total net radiation (R_n), which is used for processes of heat transformation into

individual heat fluxes. The total net radiation can be also described within the frame of heat balance as follows:

$$R_n = J + P + G + H + LE, \tag{3.2}$$

where J is the energy consumed for the change in surface temperature; P is the energy consumed for photosynthesis; G is the heat flux entering the ground; H is the sensible heat flux into the atmosphere; and LE is the latent heat flux of evaporation. Since the amount of energy consumed for the change in surface temperature and photosynthesis tends to be very low, J and P fluxes are normally omitted when considering energy transformations. Only the heat flux into the ground, sensible heat flux and latent heat flux are significantly involved in this process. All mentioned energy fluxes carry a positive sign if downward and are usually described in $\mathrm{W\,m^{-2}}$.

From a simple modification of the heat balance equation (3.2) we can obtain following expression of sensible heat flux:

$$H = R_n - G - LE. \tag{3.3}$$

Furthermore, sensible heat flux is possible to express analogically to the Ohm's law as a ratio of temperature gradient δT of a surface temperature T_s and the air temperature T_a to aerodynamic resistance of atmosphere for heat and momentum transfer r_a $[\mathrm{s\,m^{-1}}]$ (Thom 1975):

$$H = \frac{\rho c_p \delta T}{r_a} = \frac{\rho c_p \left(T_s - T_a\right)}{r_a}, \tag{3.4}$$

where ρ is the density of air $[\mathrm{kg\,m^{-3}}]$; and c_p is the specific thermal capacity of dry air $[\mathrm{J\,kg^{-1}\,K^{-1}}]$. Note that r_a is a function of surface aerodynamic characteristics (e.g. surface roughness), wind speed, vertical temperature profile and atmospheric stability. With combination of equations 3.3 and 3.4 we can express surface temperature in the following way:

$$T_s = \frac{\left(R_n - G - LE\right) r_a}{\rho c_p} + T_a. \tag{3.5}$$

The above mentioned equation shows that surface temperature involves the solar radiation balance, transfer of energy into the body itself (ground), evaporation and, alternatively, water condensation, aerodynamic properties of the surface, wind flow and environment properties (e.g., air heat capacity, air specific density and air temperature). The amount of solar radiation, surface aerodynamic properties and wind flow act as energy sources, evapotranspiration consumes the energy. When observing natural surfaces (Figure 3.1), temperature variations of surfaces covered with vegetation are of a smaller extent than those without vegetation. The same holds true for dry and wet areas. If it is true that surface temperature is a result of energy transformations, we can significantly influence the entire thermal regime at the landscape level, by adjusting the water regime and vegetation coverage.

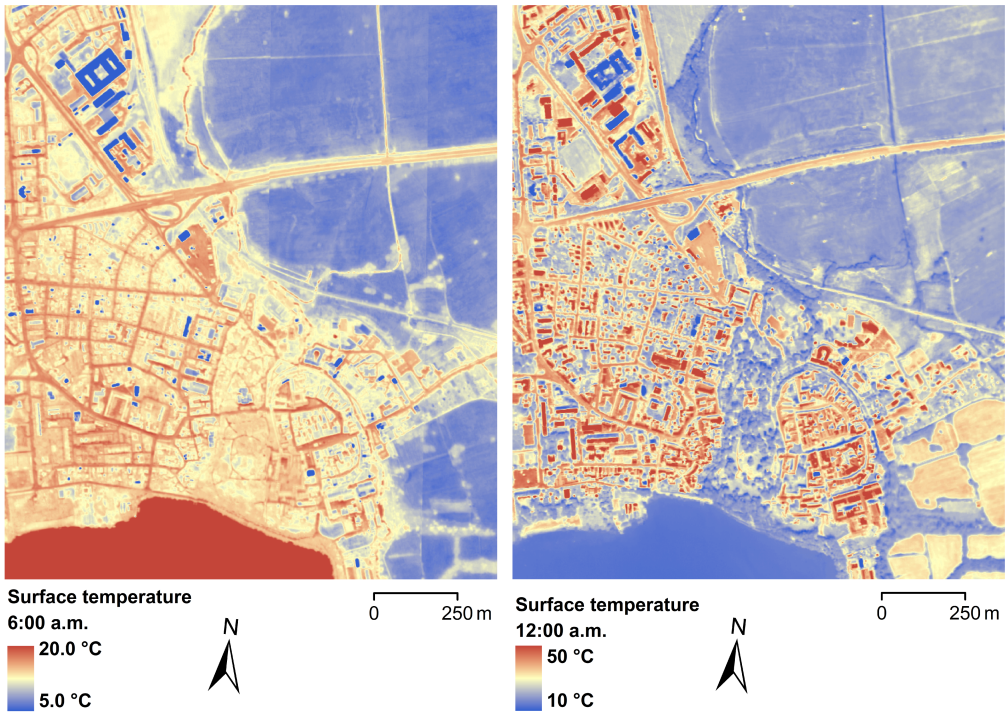

Figure 3.1 Temperature maps of the Třeboň town centre and its surroundings in the morning and noon during a cloudless summer day (July 27, 2008). The built-up area accumulates heat and forms a "heat island" in the town. Similarly, heat accumulates in water bodies (the Svět pond in the lower part of the image). Surfaces covered with vegetation in the right part of the image, where strong evapotranspiration occurs, exhibit less dynamic changes in surface temperature throughout the day. Note that the colour scale is different in the two images.

3.1.3 Radiative Transfer Equation

The signal measured by a sensor (L_m) consists of radiance emitted from the ground, reflected downwelling atmospheric radiance ($L^{\downarrow}_{atm}$) and the atmospheric upwelling radiance ($L^{\uparrow}_{atm}$). Contribution of these three components is expressed by a radiative transfer equation (RTE) as follows:

$$L_m = \tau\varepsilon B(T_s) + \tau(1-\varepsilon)L^{\downarrow}_{atm} + L^{\uparrow}_{atm}, \tag{3.6}$$

where $B(T_s)$ is radiance of the object at temperature T_s according to the Planck's law, ε is the object's emissivity and τ is atmospheric transmittance. It is important to emphasize that all elements in the equation are wavelength dependent. The meaning of the RTE is illustrated in the Figure 3.2, where ρ is reflectance. Kirchhoff's law of thermal radiation implies that reflectance ρ can be rewritten as $(1-\varepsilon)$ for opaque materials.

In order to estimate the land surface temperature (LST) from the RTE (eq. 3.6), it is necessary to remove the influence of the atmosphere. As this is solved during the atmospheric corrections of thermal imagery, estimation of atmospheric parameters is further described in Section 3.3. Even if the atmospheric parameters are taken into account, the RTE cannot be solved if temperature and emissivity are not known. Let us note that RTE should be applied for every band in case of instruments with several thermal bands. Thus, one can obtain system of equations which is undetermined. Several approaches and algorithms were already developed to overcome this problem as can be found in (Li et al. 2013).

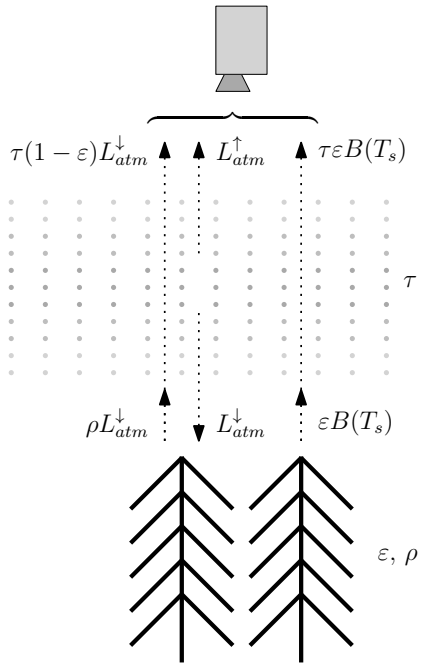

Figure 3.2 The radiance incident to the sensor in the thermal region originates mainly three sources: 1) radiance $\tau\varepsilon B(T_s)$ emitted by object with emissivity ε at temperature T_s attenuated by atmospheric transmission τ; 2) reflected downwelling atmospheric radiance $\tau(1-\varepsilon)L^{\downarrow}_{atm}$ attenuated by atmospheric transmission τ; 3) upwelling atmospheric radiance $L^{\uparrow}_{atm}$ emitted by atmosphere itself.

3.2 Overview of Airborne Thermal Instruments

Brightness temperature measurements are contactless. For ground point measurements pyrometers (IR thermometers) are used. To get spatial information there are two systems of IR thermal imaging:

a) Focal plane arrays (FPA) – mostly thermocameras,

b) Scanning systems – onboard many satellites and hyperspectral sensors.

Thermal broadband cameras use FPA to record spatial information along both dimensions of the array, but only in one spectral band. The response function of thermal broadband cameras usually covers the entire width of one of the atmospheric windows. In other words, the full width half maximum (FWHM) is almost as wide as the atmospheric window will allow. The resolution of thermal broadband cameras varies from 100×100 up to 1024×1024 pixels. Table 3.1 provides a summary of currently used broadband cameras for acquisition of thermal data.

Instruments based on the Fourier Transform Infrared technology (FT-IR) are mainly used for laboratory purposes, but there is also an airborne instrument that takes advantage of this principle. Hyper-Cam LW instrument developed by Telops, Inc. (Canada), which incorporates FPA of resolution 320×256 pixels. Hyper-Cam LW uses both dimensions of the FPA for spatial information record, while spectral information is acquired using an interferometer. The spectral resolution of Hyper-Cam LW is up to $0.25\,\mathrm{cm}^{-1}$.

In case of the pushbroom scanners, the spatial information is recorded along one dimension of FPA while other dimension is used for spectral information (see Section 1.4 for details). Disadvantage of this imaging system is dependence on relative movement between sensor and target. The overview of currently operational pushbroom hyperspectral thermal sensors is shown in Table 3.2.

In addition to the mentioned technologies and instruments, there are many other instruments, which are either not operational or still under development. There are also other acquisition principles that combine already mentioned FPA technologies.

3.3 Thermal Data Corrections and Calibrations

Thermal data corrections are essential for performing accurate analyses and estimation of land surface parameters. Corrections usually consist of instrument calibration, compensating for atmospheric attenuation and reflected atmospheric radiation and geometric corrections. Description of geometric corrections is deliberately omitted here as it follows the same principle as geometric correction of airborne imaging spectroscopy data. Therefore we refer readers to check Section 2.3.3 for details. In this section we rather put more emphasis on radiometric and atmospheric corrections. In general, the instrument acquires thermal data in raw format, which is usually referred to digital numbers (DN). The main goal of these corrections is to define the relationship between DN and land surface leaving radiance or surface temperature. There are many approaches and methods of radiometric correction and data calibration (Lillesand & Kiefer 2000). The choice of relevant method depends on the data and sensor type, as well as acquisition purposes.

Table 3.1 Examples of thermal broadband cameras used on board airplanes and unmanned aerial vehicles.

Name	Spectral range (µm)	FPA resolution (pixels)	Manufacturer/Operator
Thermalimager TI	8–14	768 × 500	Termal Imaging Ltd./Scandat
Digi THERM	7.5–14	640 × 480	IGI GmbH/Gispro Sp.o.o.
FLIR SC645	7.8–14	640 × 480	FLIR Systems. Inc./ARGUS GEO SYSTÉM s.r.o., ENKI, o.p.s.
FLIR SC660	7.5–13	640 × 480	FLIR Systems. Inc./ CzechGlobe
FLIR PM695	7.5–13	320 × 240	FLIR Systems. Inc/ ENKI, po.p.s., ČVUT, Airship.Com
Vario CCAM	7.5–14	640 × 480	Jenoptic Germany/Geodis Brno, s.r.o.

3.3.1 Radiometric Calibration

The first step is converting DN values into radiance, which is called radiometric calibration of the instrument. Commonly used approach consists of measuring two blackbodies at known temperatures. Blackbodies should represent the temperature extremes that can be recorded in the image. It can be assumed, that DN is linearly dependent on amount of incident energy and thus, following equation holds:

$$L = a + b\,\mathrm{DN}, \tag{3.7}$$

where L is the incident radiance to the sensor and a, b are unknown constants. Let us consider the radiance $L(T_{BBC})$ of a cold blackbody and the radiance $L(T_{BBH})$ of a hot blackbody according to the Plank's law. Then constants a and b can be calculated using following equations:

$$a = \frac{L(T_{BBH})\mathrm{DN}_C - L(T_{BBC})\mathrm{DN}_H}{\mathrm{DN}_C - \mathrm{DN}_H} \tag{3.8}$$

$$b = \frac{L(T_{BBC}) - L(T_{BBH})}{\mathrm{DN}_C - \mathrm{DN}_H} \tag{3.9}$$

where DN_C and DN_H are digital numbers measured by sensor viewing cold and hot body respectively. Again, it is important to emphasize that equation eq. 3.7 depends on a wavelength and thus it is necessary to perform radiometric calibrations for every spectral band.

Radiometric calibration can be performed either in laboratory (in case of broadband cameras) or directly before data acquisition (in case of hyperspec-

Table 3.2 Overview of currently operational airborne hyperspectral sensors in the thermal domain.

Name	Full name	Max. No. of bands	Spectral range (μm)	Spectral sampling (nm)	Manufacturer/Operator (Information source)
AHS 80	Airborne Hyperspectral Scanner	80	0.441–13.17	30–500	Argonst (formerly SenSyTech inc., Daedalus inc.)/ e.g. INTA (`http://www.uv.es/~leo/sen2flex/ahs.htm`)
TASI	Thermal Airborne Spectrographic Imager	32/64	8–11.5	125/55	Itres Ltd./ CzechGlobe (`http://www.itres.com/products/imagers`)
AISA Owl		84	8–12	100	Specim Ltd./ unknown (`http://www.specim.fi/index.php/products/airborne/aisaowl`)
SEBASS	Spatially Enhanced Broadband Array Spectrograph System	128	7.5–13.5		The Aerospace Corporation/ unknown
HyTES	Hyperspectral Thermal Emission Spectrometer	256	7.5–12	18	Jet Propulsion Laboratory/ Jet Propulsion Laboratory (`http://hytes.jpl.nasa.gov/`)

tral instruments). In general, the second approach is recommended, since it takes into account an immediate instrument state.

Instruments' DN can be directly converted to temperature instead of radiance values. However, the relationship between temperature and radiance is non-linear and relies on knowledge of the target's emissivity. Therefore several blackbodies with different temperature have to be employed for the calibration. Non-linear relationship between DN and temperature (T) is expressed as

$$\mathrm{DN} = \frac{R}{\exp\left(\frac{B}{T}\right) - F}, \tag{3.10}$$

where R, B and F are unknown constants. This kind of calibration is often used for data acquired by thermal broadband cameras.

3.3.2 Atmospheric Corrections

The atmosphere influences thermal data in three ways. It attenuates the ground-leaving radiance and it is a source of emitted and reflected radiance reaching a sensor. Removal of the atmospheric effects from the thermal data is essential if one wants to retrieve surface temperature or spectral signatures of surface emissivity. The atmospheric effects are included in the radiative transfer equation (eq. 3.6) as atmospheric transmittance (τ), upwelling atmospheric radiance ($L^{\uparrow}_{atm}$) and downwelling atmosphere radiance ($L^{\downarrow}_{atm}$). Atmospheric effects can be corrected for by either modelling the atmosphere using a radiative transfer model or by applying an in-scene based algorithm.

There is a difference between the corrections applied on the broadband and hyperspectral thermal data. Therefore we will first discuss corrections applied on broadband thermal data (tailored to a FLIR broadband camera) and then we will discuss corrections required for pre-processing of hyperspectral thermal data.

Broadband thermal data

Calibrations of broadband thermal data are simpler than of hyperspectral thermal data. If the ultimate purpose of the thermal broadband data is an accurate retrieval of surface temperature, ancillary data describing current atmospheric and environmental conditions have to be supplied simultaneously to the thermal data acquisition. The thermal broadband data can be calibrated directly during the flight, using camera's internal pre-set of calibration parameters, or after the flight. Having a concrete broadband camera in mind (e.g. FLIR), for in-flight, as well as for a post-flight calibration, ancillary measurements of following parameters are required:

- Object's emissivity ε
- relative humidity R_h

- distance from the measured object D_{obj} (i.e. flight altitude)
- reflected temperature T_{refl} from the surroundings
- atmospheric/sky temperature T_{sky}
- temperature of external optics T_{exo}

In the following section we describe how the parameters can be obtained directly or calculated indirectly from in-situ meteorological measurements. The emissivity value can be pre-set to a default value equal to 0.98 as it is an average value for most of vegetated surfaces. Relative humidity, as well as air temperature, can be measured in-situ, 2 m above ground surface according to standard protocols. Air temperature measurements approximate the effective temperature of the surroundings, i.e. reflected ambient temperature T_{refl}. The atmospheric temperature T_{sky} has to be calculated from data measured by infra-red radiometer (pyrgeometer). This device measures emitted sky and ground radiation in infra-red domain (approx. 4.5–50 µm). The atmospheric temperature T_{sky} is estimated as follows:

$$T_{sky} = \sqrt[4]{\frac{R_{ldown} + \varepsilon\sigma \left(T_{rad}\right)^4}{\varepsilon\sigma}}, \tag{3.11}$$

where R_{ldown} represents measured longwave radiation between sky and pyrgeometer, T_{rad} is the radiometer temperature and σ is Stefan-Boltzman constant. Both emissivity values are approximated by the black body values, i.e. $\varepsilon = 1$.

The last of the parameters, the temperature of external optics (T_{exo}) can be set to the same value as measured air temperature on the ground, if the flight altitude does not exceed 300 m. When flying higher, one takes the ambient temperature around the sensor.

Once all the parameters are supplied to the camera, or to the post-processing software, the image calibration is easy and straightforward. It is important to realize that many of the above discussed parameters can vary significantly in time and space. Therefore the most optimal case is to measure them continuously during the flight and at several locations dispersed equally around the test area.

Hyperspectral Thermal Data

The atmospheric corrections are usually based on radiative transfer models of the atmosphere. Similarly as for hyperspectral data in the reflective domain the most widely used one is MODTRAN (Berk et al. 2006). MODTRAN simulates atmospheric transmittance, downwelling and upwelling atmospheric radiance based on input parameters such as vertical profiles of air humidity and temperature, CO_2 concentration, the choice of model atmosphere (if measured profiles are not available), aerosol model or measurements and many others. Some of the model input parameters can be obtained through in-situ measurements. For example sun-photometer measures atmospheric water vapour and aerosols content, radiosondes

are used to measure vertical temperature and water vapour profile of atmosphere, and radiometers for land-leaving radiance. When these measurements are not available, then corresponding information can be obtained from local meteorological stations and/or standard atmosphere models. Other sources of supplementary data can be either hyperspectral airborne image or satellite-based products acquired close to the thermal data overflight.

An example of a software toolbox that allows complex solution for atmospheric correction of data in the thermal, as well as in the reflective domain, is ATCOR (Richter & Schläpfer 2002). ATCOR uses look-up-tables generated by MODTRAN and takes into account terrain topography and sensor parameters. In addition it offers basic temperature-emissivity separation algorithms.

In case of thermal hyperspectral data, various algorithms for estimating atmospheric effects based just on the hyperspectral cube itself were developed. Usually it is applied to one of the following: In-Scene Atmospheric Corrections (ISAC) introduced by (Young et al. 2002) and Autonomous Atmospheric Compensation (AAC) introduced by (Gu et al. 2000). The advantage of using one of these algorithms is that no supporting data are necessary.

Vicarious Calibration

Vicarious calibration is a specific calibration technique where in-situ spectral signatures of natural or artificial surfaces are used to calibrate the image data. This calibration technique performs both radiometric calibration and atmospheric correction at the same time. More specifically, DN values of an airborne thermal image are calibrated to the values of in-situ measured ground-leaving radiance. In-situ spectra can be measured for example with a portable FTIR spectrometer (Model 102, D&P Instruments, US). Field spectra must be collected simultaneously to the airborne image acquisition. Selected surfaces must be large enough to be identified on the image and spectrally homogenous. Vicarious calibration is more suitable for hyperspectral than for broadband thermal data.

Recommended Reading

Kuenzer, C. & Dech, S. 2013. Thermal Infrared Remote Sensing: Sensors, Methods, Applications. *Remote Sensing and Digital Image Processing* 17.

Quattrochi, D.A. & Goel, N.S. 1995. Spatial and Temporal Scaling of Infrared Remote Sensing Data. *Remote Sensing Reviews* 12: 256–286.

4

AERIAL AND TERRESTRIAL LASER SCANNING

Vlastimil Hanzl, Jan Novotný, Miloš Cibulka, and Lucie Homolová

Laser scanning is a remote and proximal sensing technology that allows precise determination of a 3D structure of objects of interest. Laser scanners are active systems that emit light pulses and record reflected energy that comes back (Figure 4.1). The technology itself is well known since 1960's. However, advances in the fields of electronics and informatics very much stimulated the rapid development of laser scanning in the last two decades. The possibility of processing large volume data has effectively opened up laser scanning to a multitude of applications such as topographic, environmental, industrial and cultural heritage 3D mapping.

Laser scanners can be installed on moving airborne platforms (aerial laser scanning – ALS), as well as on fixed ground-based platforms (terrestrial laser scanning – TLS). In the following sections we will briefly introduce basic principles of laser scanning, some commercially available ALS systems, basic post-processing steps applied on point cloud data and mention the most common ultimate product of ALS – digital elevation models (DEM).

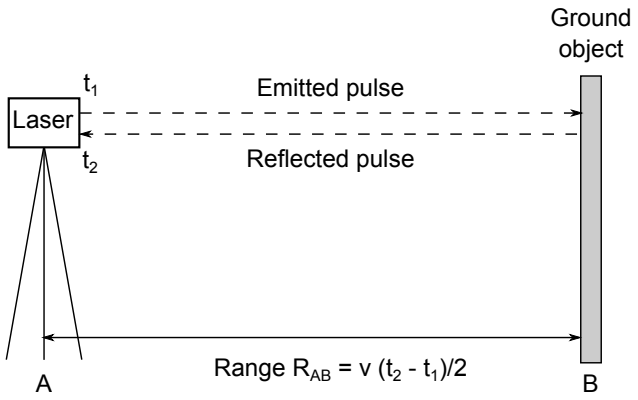

Figure 4.1 Basic principle of laser ranging (measurement of distances) using a time-of-flight method. A distance between a scanner A and an object B (range R_{AB}) is calculated from a difference between time when a light pulse is being emitted (t_1) and time when a reflected pulse is recorded back (t_2) and the speed of light (ν).

4.1 Aerial Laser Scanning

4.1.1 Principle of ALS

A typical aerial laser scanning system consists of following main components:

1. A basic laser ranging unit. It consists of a laser, transmitting and receiving optics, a receiver with a detector and digitizing unit to capture the received signal, and a time counter to measure elapsed time between the emitted and returned signal. The ranging unit measures a slant distance between the scanner and the ground as illustrated in Figure 4.1.
2. An optical scanning mechanism. It determines a ground pattern of measured points. A typical example of the scanning mechanism is an oscillating mirror, which together with an angular encoder, directs a stream of light pulses at known angles at high speed along a line in the across-track direction relative to the flight path. The scanning mechanism allows making successive point measurements along one line (a profile). The forward motion of an aircraft allows forming series of profiles and scanning the entire flight swath of the terrain.
3. A control and data recording unit. It is normally a computer-based device that allows an operator to control scanning settings and process of data recording.
4. An IMU/GNSS unit. Together these constantly measure precise position of the aircraft and orientation of the laser scanner – six parameters obtained at the same time.

5. An imaging device. Often, a digital frame camera (60–80 megapixels) or imaging scanner is integrated with the laser scanner to supply visual information together with 3D point cloud data.

Most of the up-to-date ALS systems have the capability of recording multiple discrete returns from one emitted pulse and the intensity of returned echoes. Nowadays, all principal manufacturers of ALS systems also provide the capability of full waveform digitization, i.e. recording the complete return (Figure 4.2). This feature is particularly useful for vegetation mapping as it allows mapping of multilevel canopies or forest canopy structure (Mallet & Bretar, 2009).

Besides the measurements of range the intensity of the returned pulse is also recorded. This information is dependent on the emitted wavelength, on the reflectivity of a surface, on the scanning angle and atmospheric conditions. Many systems use wavelengths from the near infra-red region, as this region is less affected by atmospheric absorption and many natural surfaces are highly reflective in that region. However, the intensity information has to be interpreted with care. Intensity normalization is required to compensate for different scan angles and variable distances between the scanner and ground objects (i.e. signal received from more distant objects will be weaker than from closer objects with the same reflectance properties) (Jutzi & Gross, 2007). Intensity values appear to be of a limited interest to the users, who focus on positional and elevation data only, but it can be used for classification purposes. Recently, a new multi-wavelength canopy LiDAR system has been developed and successfully tested for vegetation monitoring (Bo et al., 2011; Wei et al., 2012). It measures in four wavelengths (556 nm, 670 nm, 700 nm and 780 nm). The wavelengths were chosen according to nitrogen stresses that induce changes in the optical properties and spectral reflectance of leaves. In addition to assessing plant stress, the information can be particularly useful in separation between different phenological developments of the crops.

4.1.2 Scanning Parameters and Properties of ALS Systems

There are several parameters and properties of the ALS system that a user/operator should be aware of in order to acquire data of desired resolution and quality. Some very important parameters of ALS systems are *pulse repetition frequency* (PRF) and *scan rate*. Both parameters, together with flight altitude and field of view (FOV, i.e. the angular width of the scan swath), determine the actual density of points that are being measured on the ground. The first parameter, PRF is a rate of successive pulses. With increasing PRF, the mean point density on the ground also increases. In earlier types of airborne laser scanners, only one pulse at time could be in air, i.e. the next pulse could be fired only when the previous one returned. This limitation has been overcome by using the technique of "multiple pulses in the air", which was recently adopted by all manufacturers. With the introduction of this technique, maximum PRF increased to 200 kHz and greater,

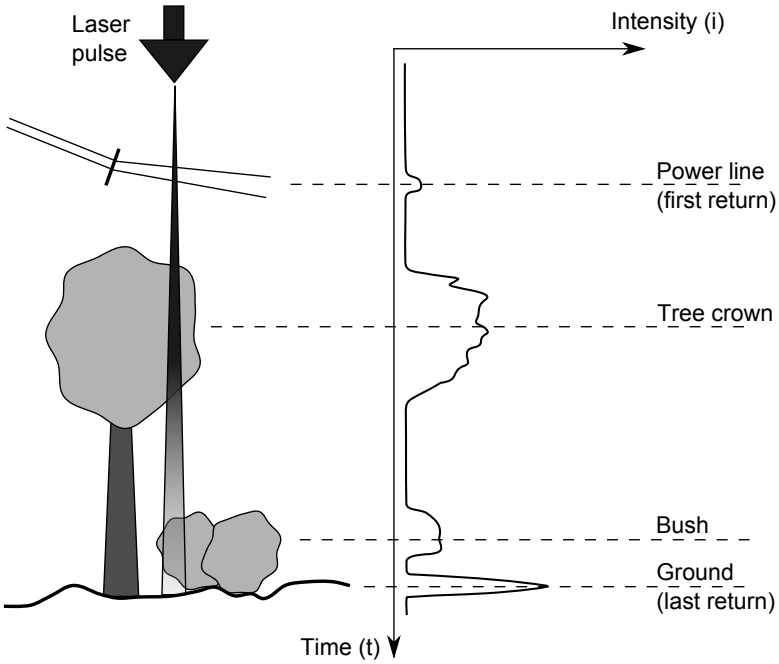

Figure 4.2 Full waveform laser scanning system provides complete digitization of returned signal.

though the actual PRF will still depend on the flying altitude. The second parameter, *scan rate* is the rate of successive profiles measured on ground. It is inversely proportional to the scanner's FOV. Greater the scan rates can also be achieved using dual streams of pulses fired from twin scanners (e.g. Riegl system BP-560, which utilizes two LMS-Q560 scanners, or Peagasus system from Optech).

The scan pattern on ground depends on how the beam sweeps. This depends of scan rate, as well as on the type of optical scanning mechanism. The saw-toothed pattern or sinusoidal pattern is formed using a bi-directional oscillating mirror (Optech or Leica scanners). The equally-spaced grid scan pattern is produced by rotating uni-directional polygon mirror (Riegl scanners). The grid scan pattern with different point spacing across and along track is formed using a glass fiber scanner. Yet another scanning pattern, which is used in the TopEye systems, is the so-called Palmer scan. It uses of nutating mirrors to produce overlapping elliptical scans.

Another important property of a laser scanner is the footprint of the laser beam on the ground. It is a circular or elliptical area and its diameter depends on laser beam divergence and flight altitude. Typical values of beam divergence are between 0.1 and 1.0 mrad. For example, for the beam divergence 0.25 mrad and flight altitude of 1 km the diameter of the footprint is 29 cm. It will increase with increasing flight altitude.

4.1.3 The Scanning Accuracy

All measured ALS data have certain accuracy limitations. The overall accuracy of ALS data lies in the range of 8–20 cm for X and Y coordinates and 8–50 cm for elevation depending mainly on the flight altitude. There are three main sources of errors that influence position accuracy of final laser points. These are errors originating from: i) laser measurements, ii) IMU/GNSS measurements and iii) instrument misalignment. First, distances are measured with an error of about 0.02 m and scan angles are measured with an error of 0.001–0.002 gon (it translates in a positional error of 1.6–3.2 cm at nadir at the flight altitude of 1 km). Second, the largest contribution to the overall error budget originates from the IMU/GNSS measurements. The errors in scanner's platform position eX, eY are about 8–50 cm and eZ is between 8 and 20 cm. Measurements errors in the IMU recorded pitch and roll can be around 5 mgon (it translates in a positional error of 8 cm at the flight altitude of 1 km) and 15 mgon in heading. Third, boresight misalignment (i.e. positional and angular shifts between the IMU/GNSS unit and the laser scanner) and position of GNSS antenna (i.e. vector between a GNSS antenna and the reference point of the IMU/GNSS unit) cause errors in final ALS data that are less than 1 cm. Other possible sources of error are beam divergence, terrain and object characteristics, time synchronization, coordinate system transformations, atmospheric refraction and sensor mounting rigidity. All these sum up to a maximum error contribution of 0–5 cm.

4.2 Overview of Aerial Laser Scanners

Topographic ALS systems can be either multipurpose instruments or designed for rather specific applications. Their applicability is determined by the combination of several basic operational parameters of the ALS, such as maximum operational altitude, maximum scanning rate, etc. For example, corridor mapping and various engineering applications require lower-altitude data with high point densities (several tens of points per square meter) and sub-decimeter accuracies. There is also a demand for data covering large areas that have to be acquired from higher flight altitudes. These kind of data facilitate digital terrain mapping (DTM) at regional and national levels.

Currently, a multitude of commercial and custom-built aerial laser systems is available. The market is, however, dominated by three principal commercial suppliers; Leica Geosystems (Germany), Optech (USA) and Riegl (Austria). In Table 4.1 we summarize the basic parameters of a few selected systems that are currently on the market.

Leica Geosystems (group Hexogen) entered the market in 2001 and currently offers the following systems: ALS70 CM, which is designed for city and corridor mapping, ALS70 HP, which is used for general-purpose mapping and ALS70 HA, which is designed for wide area mapping.

The Optech company has built its series of ALTM (Airborne Laser Terrain Mapper). The first model ALTM 1020 was released in 1993. The current ALTM systems are Pegasus, Orion and Galaxy. Pegasus allows data acquisition at higher PRF, while Orion facilitates low to mid-altitude engineering surveys. In 2014, the Galaxy model was released and it represents the next generation of ALS for a wide range of applications ranging from wide-area mapping to corridor surveys.

Riegl has produced ALS systems since 2003. The model LMS-Q680i is designed for general-purposes, LMS-Q780 is designed for high altitude wide area mapping and LMS-Q1560 is fully integrated ALS for ultra wide area mapping.

Some companies provide custom-built topographic laser systems such as the FLI-MAP system from Furgo Geospatial or the TopEye system from Norwegian Blom (Petrie, 2011).

A special kind of ALS is airborne laser bathymetry, which is used for surveying shallow coastal and inland waters (Mandlburger et al., 2011). The basic difference compared to the above listed topographic ALS systems is that bathymetric laser scanners employ two rangefinders operating at different wavelengths. One operates in the NIR region, where an emitted pulse is reflected back from the water surface. Another one operates in the green region, where an emitted pulse passes through the water column and is reflected back by the bottom of a water body. Differencing the two measurements allows monitoring of water depth to a maximum depth of about 25 m.

In the Czech Republic, as far as we know, there are currently only two topographic airborne laser scanners being operated. In 2014, Argus Geo Systém operated Leica's ALS 50-II and Riegl's LMSQ-680i. Another system from Riegl (LMSQ-780i) has been recently purchased by the AdMaS Centre, Brno University of Technology.

4.3 Terrestrial Laser Scanning

We are going to introduce terrestrial laser scanning (TLS) by comparing it to aerial laser scanning. In principle, TLS differs from ALS in that the TLS scanner is not moving during the data acquisition process. During ALS data acquisition a laser beam is emitted and reflected across the direction of the flight line. However, TLS data are being acquired in the whole hemisphere around the instrument. Therefore a slant distance and the two angles in vertical and horizontal planes are measured simultaneously in order to determine the point coordinates. Terrestrial laser scanners record discrete pulses and do not use full wave digitization except for a few scanners produced by Riegl.

From the point of view of precision and maximum scanning distance, terrestrial laser scanners can be divided into three groups: short-, medium- and long-range scanners. The short-range scanners acquire highly precise data with accuracy of 1 mm typically with maximum distances from 50 to 120 m. They often use a phase

Table 4.1 Overview of basic parameters of selected ALS systems produced by three principal suppliers that are currently available on the market. (Abbreviations: PRF — pulse repetition frequency, FOV — field of view)

Model	Max. altitude (m)	Max. PRF (point/sec)	Max. FOV (°)	Max. scan rate (Hz)
Leica Geosystems (http://www.leica-geosystems.com/en/Airborne-LIDAR_86814.htm)				
ALS70 CM	1,600	500,000	75	200
ALS70 HP	3,500	500,000	75	200
ALS70 HA	5,000	250,000	75	100
Optech (http://www.optech.com/index.php/products/airborne-survey/lidar-systems/)				
Pegasus HD500	2,500	500,000	75	140
Orion C300	1,100	300,000	50	90
Galaxy	4,700	550,000	60	100
Riegl (http://www.riegl.com/nc/products/airborne-scanning/)				
LMS-Q680i	1,650	400,000	60	200
LMS-Q780i	3,050	400,000	60	200
LMS-Q1560	4,700	800,000	60	400

method to measure distances. In the phase method a continuous beam of light is being emitted instead of a pulse. The distance is derived by comparing the emitted and received versions of the sinusoidal wave pattern and measuring the phase difference between them. The most prominent producers of this type of scanner are two German companies, Zoller+Fröhlich and Faro, and Basis Software Inc. from the US. Only a single company -– Callidus from Germany -– has adopted the time-of-flight measurement method (Figure 4.1) for its short-range scanners. All the medium- and long- range scanners use the time-of-flight method (Figure 4.1) for distance measurements. Medium-range scanners can measure distances over medium ranges, typically between 150 and 350 m, whereas long-range scanners can measure well beyond 500 m (1–4 km). Typical accuracy achieved by these systems varies between 5 and 20 mm depending on the maximum measured range. Principal suppliers of medium-range scanners are Leica, Trimble and Topcon. Principal suppliers of long-range scanners are Reigl and Optech.

4.4 Processing of Aerial Laser Scanning Data

Typical steps that are required in order to process ALS data are as follows: 1) calibration of the system, 2) strip adjustment, 3) point filtering and classification, and 4) specific post-processing techniques, depending on the application.

4.4.1 Calibration

In order to determine the accurate position of a point on the earth's surface it is necessary to know the exact position and orientation of the laser scanner. For this purpose the IMU/GNSS unit continuously records the actual position and orientation of the airborne platform. Typically, laser scanning data are acquired with higher frequencies than position ($\approx 10\,\text{Hz}$) and orientation ($\approx 200\,\text{Hz}$) data. Therefore the IMU/GNSS data has to be interpolated and synchronized with corresponding ALS data.

A prerequisite is the knowledge of the spatial relationships between the laser scanner and the IMU/GNSS components. These are: i) a vector from the IMU reference point to the phase center of GNSS antenna and ii) angular rotation between axes of the coordinate system of the scanner and IMU (Figure 4.3). The first one is measured geodetically, the second one is determined during so-called boresight calibration flight. The calibration flight is usually done at the beginning of the data acquisition season or any time when either the scanner or IMU/GNSS unit has been moved.

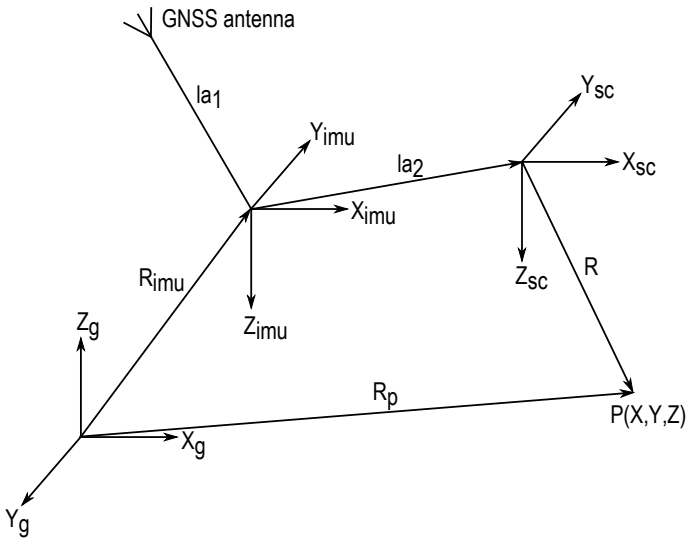

Figure 4.3 Illustration of geometrical relationships between coordinate systems of the IMU unit (X_{imu}, Y_{imu}, Z_{imu}), a laser scanner (X_{sc}, Y_{sc}, Z_{sc}), known geodetic system (X_g, Y_g, Z_g) and a laser point P with unknown coordinates X, Y, Z. Further abbreviations are la_1 – lever arm from GNSS antenna phase center to the origin of IMU coordinate system, la_2 – lever arm from the origin of IMU coordinate system to the origin of scanner coordinate system, R_{imu} – spatial vector between geodetic system and IMU, R_p – spatial vector between geodetic system and the determined point P, R – is distance between scanner and point P.

4.4.2 Strip Adjustment

After calculating the spatial position of points within a single strip (i.e. data acquisition along a more or less straight flight line), the adjustment of adjacent flight strips follows. Typically, the overlap between adjacent flight strips is about 20 % to ensure that entire surface area is covered. Due to residual systematic errors of the laser scanner, the position and height of a single object that has been identified on both adjacent strips will not be absolutely identical. Therefore the flight strips have to be adjusted in order to append them into one point cloud. Usually, software for processing of ALS data allows automatic identification of common objects on two adjacent strips. It calculates a transformation between the two strips using a least squares approach. Always one strip is selected as a base and the others are appended based on the calculated transformation. This is known as relative adjustment of ALS strips. A minimum of three ground control points are then required to transform the entire point cloud into its absolute position in a global coordinate system.

4.4.3 Filtering and Classification

The most common use of ALS data is terrain mapping and therefore classification of ground return points is of the utmost importance. The process of classification of points as ground returns is referred as ground filtering (Figure 4.4). There are several ground filtering techniques described in literature (Sithole & Vosselman, 2004). However, here we will only mention two common approaches and refer to published papers for more details. The first group of filter algorithms is based on the concept of mathematical morphology. It combines two basic operations (opening and closing) on a point cloud to determine the upper and lower surface within a profile (Vosselman, 2000). The second approach works with a progressive densification of the set of ground points. The very first ground points are chosen as local minima in a certain sparse grid. The next points are added to the ground set if they meet specific criteria such as height difference or angular offsets (Axelsson, 2000).

4.4.4 Application Specific Processing Techniques

All further data processing steps are very much application specific. The most common fields where ALS data are used include: 1) digital terrain models (see Section 4.5 for further details), 2) building extraction, 3) forestry applications (see Chapter 9), 4) engineering applications, 5) cultural heritage applications, or 6) mobile mapping. Other processing techniques include, for example, object classification, vectorization, rendering, colouring, and converting point clouds into a raster format. For example, Figure 4.5 illustrates classification of objects in an urban environment.

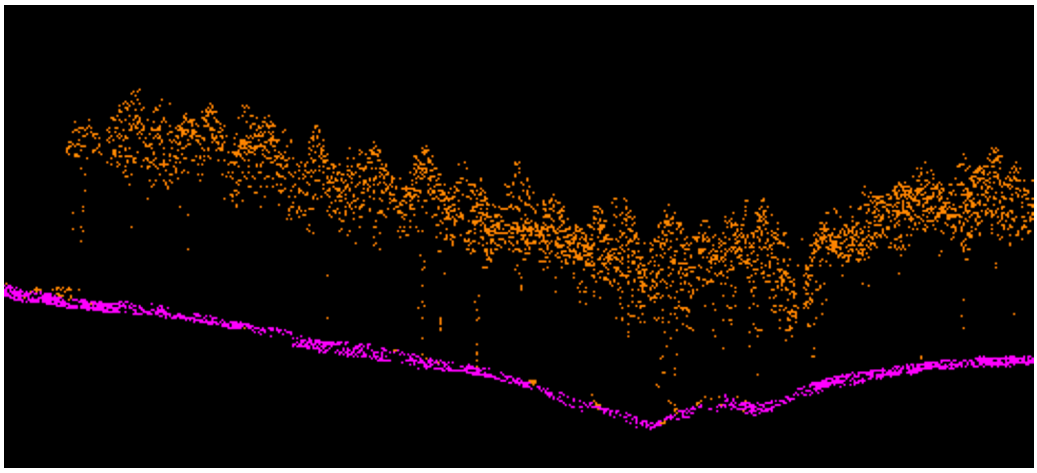

Figure 4.4 Illustration of the ground filtering process. Ground points are presented in violet, the other unclassified points are presented in orange.

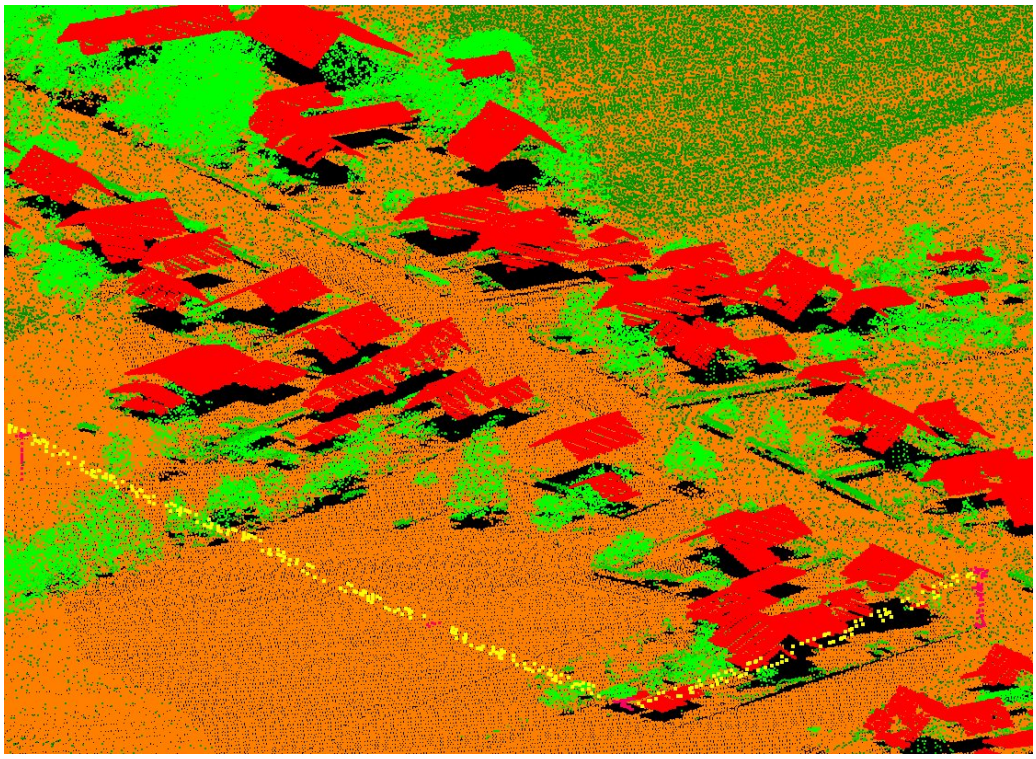

Figure 4.5 Example of a classification of the point cloud into five classes: roofs (red points), trees and high vegetation (light green), low vegetation (dark green), power line (yellow) and bare ground surface (orange).

4.5 Digital Elevation Model and Its Accuracy

4.5.1 Definition of the Terms

First, it is important to clarify differences between digital elevation, terrain and surface models as there seems to be some confusion in the literature how these terms are used in different fields of application. Here, we define digital elevation model (DEM) as a generic term for any kind of digital representation of elevation data. We use digital terrain model (DTM) for bare ground only, free of vegetation, buildings, etc. In contrast, a digital surface model (DSM) is derived from first reflective surfaces including all natural terrain features, vegetation cover and all man-made objects.

4.5.2 DEMs in the Czech Republic

Until recently, ALS data in the Czech Republic were provided by the private sector. Nevertheless, aerial laser scanning at the national level was carried out within the framework of the cooperative project of the Czech Office for Surveying, Mapping and Cadaster (ČÚZK). The Ministry of Defense and the Ministry of Agriculture of the Czech Republic engaged in a project to create a new altimetry of the Czech Republic between 2009 and 2013. The output of the project was the creation of new digital terrain models of the 4^{th} and 5^{th} generation (DTM 4G, DTM 5G) and also a digital surface model of the 1^{st} generation (DSM 1G).

DTM 4G is provided in the form of heights of discrete points in a regular grid of 5×5 m. Its declared accuracy is the mean elevation error of 0.3 m in open areas and 1 m in forested areas. DTM 5G is distributed in the form of a triangulated irregular network (TIN) of selected elevation points. Its declared accuracy is the mean elevation error of 0.18 m in the terrain without vegetation and 0.3 m in forested areas. Currently, DTM 5G covers only a part of the Czech Republic and it is expected that the full coverage will be finished by the end of 2015. DSM 1G is distributed similarly like DTM 5G in the form of TIN. Its mean elevation error is 0.4 m for regular-shape objects (e.g. buildings) and it is 0.7 m for objects with irregular boundaries (e.g vegetation cover). The DSM 1G for the whole republic shall be also finished in 2015.

4.5.3 Accuracy Assessment of DEM

ČÚZK is continuously evaluating the accuracy of the new DEM products. The declared accuracy of all those new products is much higher when compared to previous elevation products (Brázdil, 2012). However, in the forested area, the accuracy can be lower than the declared one due to many factors influencing the signal penetration through forest canopies. A DEM serves as an important geospatial resource for forest planning and management; therefore, it is of high importance to characterize well accuracies of the new DEM products in forest environments.

For this reason an independent verification of the accuracy of the new DTM 5G model and contour lines from ZABAGED (topographic model of CR produced by ČÚZK) in forested areas was performed by Mendel University in Brno (Cibulka & Mikita, 2011; Mikita et al., 2013a). For the purpose of this comparison, European beech and Norway spruce dominant forests were selected and tachymetric measurements were performed there in order to obtain precise coordinates of reference points. Generally, a probability that the reference points can be directly compared with the DTM 5G points is very low. Therefore, an interpolating technique has to be employed in order to derive matching pairs of points that can be compared. In this study, several interpolation techniques were evaluated, namely the methods of weighted inverse distance, minimum curvature, Delaunay triangulation, kriging, natural neighbor and topo-to-raster, as they can have some impact on the accuracy assessment.

Root mean square error (RMSE) calculated between the reference points and interpolated DTM 5G reached values between 0.27 and 0.43 m depending on the interpolation method. The method of weighted inverse distance produced the highest RMSE in both stands (0.43 m for the beech stand and 0.35 m for the spruce stand). Simpler interpolation techniques, such as nearest neighbor and triangulation, produced the lowest RMSE at both stands. The systematic component of the RMSE yielded the value of 0.16 m irrespective of the interpolation method. The positive sign of the systematic error indicates that the terrain derived from the ALS data (DTM 5G) is situated above the real terrain. Most likely, this is caused by the inability of the last laser pulses to penetrate the herbaceous cover, reach the ground and return to the sensor. Comparison with the ZABAGED contour lines yielded much higher values of RMSE (1.6 m for the beech stand and 1.0 m for the spruce stand). However, in highly heterogeneous areas, the maximal deviations can reach the values of up to 7 m (Cibulka & Mikita, 2011).

The results of this independent evaluation confirmed that the ALS-based DTM 5G reaches reasonable accuracies in the forested area. If the systematic error of about 0.16 m could be removed, the results would be fully in accordance with the declared accuracy by ČÚZK for areas with dense vegetation. A possible solution for partly overcoming this problem would be to acquire ALS data during the leaf-off season, which would improve the accuracy in broad-leaf forests.

Recommended Reading

Shan, J. & Toth, C.K. 2009. *Topographic laser ranging and scanning: principles and processing.* CRC Press. Taylor & Francis Group.

Petrie, G. 2011. Airborne topographic laser scanners. *GEO Informatics* 14: 34—44.

5

ASSESSMENT OF WATER QUALITY

Miroslav Pikl, Blahoslav Maršálek, Eliška Maršálková, Marcela Pavlíková, and František Zemek

5.1 Introduction

Water is an essential substance on the Earth. It is a part of many natural and human induced processes. Many of these processes are closely related to some water quality requirements. System for monitoring of water quality vary according to the type of a water body. One of the most serious issues related to water quality is phytoplankton (cyanobacteria and algae) water blooms (Chorus 2001). Massive water blooms occur in many freshwater lakes, slowly running rivers and shallow coastal water due to anthropogenic eutrophication (Paerl & Paul 2012). Recent studies indicate that the occurrence of water blooms has been increasing (Kahru et al. 2007; Duan et al. 2009). Drinking water reservoirs, recreational water bodies and fish ponds are sensitive to phytoplankton development, composition and concentrations. Massive outbreaks cause oxygen depletion when the phytoplankton biomass decays. Additionally, cyanobacteria may produce toxic compounds (cyanotoxins) that can have negative impacts on human health (Rao et al. 2002). The toxins of cyanobacteria are a structurally, functionally and phylogenetically diverse group of compounds with different toxicological charac-

teristics. The most widely spread cyanobacterial toxins found in water blooms of fresh and brackish waters are hepatotoxic cyclic oligopeptides (microcystins and nodularins). For example microcystins have been isolated from planktonic, benthic and soil cyanobacteria species such as *Anabaena*, *Microcystis*, *Oscillatoria* (*Planktothrix*), *Nostoc*, *Anabaenopis*, *Hapalosiphon* (Chorus 2001). The wide spectrum of toxic compounds produced by cyanobacteria is the reason, why a lot of research effort is nowadays focused on mapping of cyanobacteria blooms and the development of early warning systems.

The standard method of phytoplankton quantification is based on laboratory microscopic analyses of water samples that are complemented by spectroscopic assessment of chlorophyll concentrations. However, this method is limited to a certain sampling area, depth horizon and moment in time. More advanced methods of phytoplankton quantification should be able to capture spatial and temporal variability of phytoplankton in a water body. The advanced methods of phytoplankton quantification include:

- Optical in-situ methods (in-situ Flow Cytometry, Analytical Flow Cytometry etc. (Goddard et al. 2005)
- In-situ and on line fluorescence quantification of dominant phytoplankton pigments (Gregor & Maršálek 2004; Izydorczyk et al. 2005; Gregor et al. 2005; Gregor et al. 2007)
- Airborne- and satellite-based optical remote sensing (RS)

The RS mapping of algae and cyanobacteria is usually based on quantitative estimation of pigments concentrations: chlorophyll *a* (C_a) (Vos et al. 2003; Gitelson et al. 2007) and phycocyanin (Pc) (Randolph et al. 2008). Empirical RS methods usually yield better results for areas with higher C_a concentration (Cheng et al. 2013), because low C_a concentrations are typically masked by other absorbing constituents (e.g., dissolved organic matter, suspended inorganic particles). In order to overcome the limitations of the empirical methods, semi-analytical (Gitelson et al. 2007; Le et al. 2009) and physically based (Vos et al. 2003) methods have been developed to estimate concentrations of C_a. These methods describe more precisely influences of other optically active water constituents.

The selection of an appropriate method and of the pre-processing done on the RS data has to be adjusted depending on what type of water body being observed. Typically, RS distinguishes between two types of water bodies: i) open ocean and ii) inland waters and shallow costal water. In case of the open ocean, the water leaving radiance recorded by a RS instrument is affected only by the absorption of water and by the absorbing and backscattering properties of phytoplankton. In case of inland waters there are additional factors which have impact on the radiance recorded by RS sensors such as colored dissolved organic matter, suspended inorganic particles, organic detritus and the scattering properties of the bottom in case of very shallow waters.

Besides monitoring of phytoplankton, remote sensing can be used to assess other properties of water ecosystems. For example, laser scanning can be used for bathymetry of shallow waters (Fernandez-Diaz et al. 2014) or for mapping sediments disposal (Montreuil et al. 2014). Hyperspectral data can be used for depth estimation in shallow waters (Ma et al. 2014), suspended inorganic particles (Giardino et al. 2014) or dissolved organic matter (Zhu et al. 2013). All these parameters are highly relevant for water quality monitoring, however the objective of this chapter is to demonstrate possibilities of airborne imaging spectroscopy to assess C_a and Pc concentrations in Brno reservoir.

5.2 Material and Methods

5.2.1 Study Area

Brno reservoir (49.2414756 N, 16.5064217 E) was our model water body. It covers area of a 256 ha, its retention volume is a 7.6 mil. m^3 and maximum depth a 23 m. Controlling of flood events and tourist recreation were the main reasons for building the dam. The reservoir has been known for its massive cyanobacteria blooms, especially in period 2000–2008, where scums of the biomass occurred every summer. That is why several countermeasures have been successfully applied since then. Because of very intensive recreation activities here, the water quality indicators (C_a, Pc, microscopic composition of phytoplankton, dissolved oxygen, transparency, temperature stratification and conductivity) are being measured by water sampling in a two-week intervals during the vegetation season.

5.2.2 Field Measurements of Water Quality

Field data about water quality were measured from a boat at 10 sample points using transect across the reservoir (hereafter called open water) and at two sites where higher concentrations of algae and cyanobacteria has been observed (hereafter called Zouvalka and dam) on 8^{th} Spetember 2013. The measurements are representative for the top layer of water (0–30 cm), as this is the layer that mostly influences the signal recorded by RS instruments. At each sample point a concentration of C_a and Pc were measured by the YSI probe (YSI Inc., USA). The YSI 6600 V2 probe is a multi-parameter, water quality measurement and data collection system. It has chlorophyll and phycocyanin sensors to determine C_a and Pc concentration based on measurement of light-induced chlorophyll fluorescence at 680 nm and 650–660 nm, respectively.

The YSI probe was equipped with additional sensors to determine conductivity, dissolved oxygen, turbidity and temperature. Furthermore, the proportion of individual species such as green algae, blue-green algae/cyanobacteria, diatoms/dinoflagellates and cryptophytes were determined using a FluoroProbe (bbe Moldaenke, Germany). The FluroProbe emits light at 370 nm, 470 nm,

525 nm, 570 nm and 610 nm to stimulate chlorophyll fluorescence. Fluorescence excitation spectra have specific shapes for functionally similar groups of phytoplankton as these groups contain similar proportions of chlorophyll.

5.2.3 Spectral Data

We collected and analyzed three types of water spectral data, each acquired under different environment conditions. We measured water spectra in the laboratory, in-situ and from an airborne platform.

First, spectral signatures of algae and cyanobacteria water samples with different C_a concentrations were measured in a laboratory using ASD FieldSpec spectrometer (ASD Inc., USA). Two sets of water samples with increasing biomass concentration (number of cells per ml of water) C_a, one for algae and the second one for cyanobacteria, were prepared in the laboratory. Chlorophyll concentration is a function of the biomass. Spectra were measured in the spectral range 400–2500 nm with a spectral sampling step of 1 nm. The constant viewing geometry and illumination conditions were ensured by placing a Petri dish with the water sample on the ASD Turntable (ASD Inc., USA). A white reference plate (Spectralon®) was measured before each sample to calibrate for reflectance.

Second, water spectral properties were measured in-situ from a boat simultaneously with the water sampling (Figure 5.1). The simultaneous measurements are important because spatial distribution of cyanobacteria and algae change rapidly in time mainly because of water surface movement. Field spectra were collected with ASD FieldSpec spectrometer (ASD Inc., USA) in the spectral range of 350–1200 nm with spectral sampling step of 1 nm. The measurements were taken with a bare optical fibre (FOV 25°) perpendicularly to the water surface from the distance of 30 cm. At each sampling point six spectra were collected, each as a result of 25 repeated measurements. Spatial location was recorded by a GPS. A white reference plate (Spectralon®) was measured before each sample to calibrate for reflectance. Field spectra were parabolically corrected to compensate for spectral intensity shifts between the visible and infrared part of spectrum (Beal & Eamon 2009). Corrected spectra were resampled to match the broader spectral resolution of the airborne AISA image data.

Third, an airborne hyperspectral image of the Brno reservoir area was acquired with the pushbroom scanner AISA Eagle (Specim Ltd., Finland) on 8th September 2013. The image was acquired in the range of 400–990 nm with the spectral sampling step of 3 nm. The spatial resolution was 3.5 m. The raw data were radiometrically, geometrically and atmospherically corrected (see details in Chapter2). The AISA image contained noise because of the combination of generally low reflectance signal over water bodies and high spectral resolution. Therefore Savitzky-Golay filter (window size of nine bands and 2nd order polynomial) was applied to smooth the noise (Savitzky & Golay 1964).

Despite the fact that the flight-line was acquired in SE-NW direction and

close to the solar noon, some sunglint effects were present due to surface wind roughening during the acquisition. The sunglint removal was based on a method proposed by Hedley et al. (2005). The method estimates the additional sunglint signal in the NIR band where, in theory, the signal should be equal to zero. After the sunglint removal the image spectra were compared with field spectral measurements and exhibited better fit to in-situ spectra, especially in the near infrared part of spectrum. The results are not presented in this study.

Figure 5.1 Spectral measurement at the dam site with height concentration of algae and cyanobacteria.

5.2.4 Mapping of Phytoplankton Distribution

The spatial distribution of phytoplankton (algae and cyanobacteria) in the Brno reservoir was approximated by mapping C_a and Pc concentrations using airborne hyperspectral data. We used a statistical approach, when relationships between field measured concentrations and associated field spectra were established from data measured and acquired simultaneously on 8^{th} September 2013. We tested two simple spectral indices that have been previously published as suitable for C_a or Pc estimation. First, a simple ratio index R_{700}/R_{675}, proposed by Vinciková et al. (2013), is related to C_a concentration. Second, a simple ratio index R_{700}/R_{600}

was experimentally designed to predict Pc concentration in samples with different C_a/Pc ratios mixed in a laboratory (Mishra et al. 2009). The established linear relationships between the two spectral indices and C_a and Pc concentrations were applied to the whole water reservoir area of the AISA image.

5.3 Results and Discussion

5.3.1 Spectral Differences of Water Samples with Different Cyanobacteria and Algae Concentration Measured in Laboratory

Laboratory spectral measurements of algae and cyanobacteria samples with increasing C_a concentration are presented at Figure 5.2. These show that different C_a concentrations produce spectral signals that are distinct from each other, especially in the chlorophyll absorption bands located at 460 and 680 nm. These two absorption regions are common for both algae and cyanobacteria but cyanobacteria samples with low C_a concentration absorbed more incident light than algae samples with similar C_a concentration. Cyanobacteria also reflected more radiance in the near infra-red region compared to the algae samples. Contrary to algae cyanobacteria also exhibit characteristic pigment absorptions in wavelengths different from chlorophyll e.g. at 620 nm (indicated by a red line at Figure 5.2b). The absorption maxima of phycocyanin is the most frequently used feature to differentiate between cyanobacteria and algae (Jupp et al. 1994; Srivastava et al. 2013).

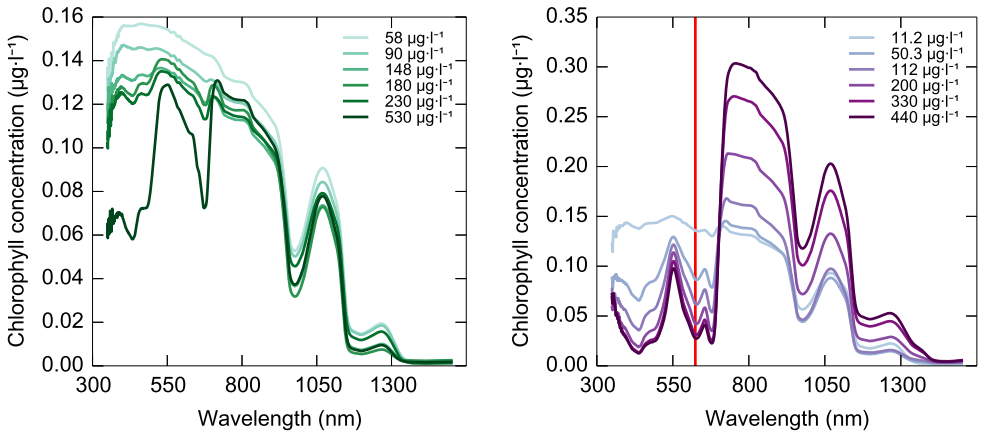

Figure 5.2 Laboratory measured spectral signatures of algae (a) and cyanobacteria (b) solutions with increasing chlorophyll-*a* concentration.

5.3.2 Spatial Distribution of Algae/Cyanobacteria in the Brno Reservoir

The two evaluated spectral indices, R_{700}/R_{675} sensitive to C_a and R_{700}/R_{600} sensitive to Pc, exhibited a linear relationship with the field measured concentrations (Figure 5.3). The achieved accuracy ($R^2 = 0.90$) of the C_a sensitive index corresponded well with results presented by Vinciková et al. (2013). The model based on the Pc-sensitive index explained less variability ($R^2 = 0.73$) than the C_a model (cf. Figure 5.3a and b). The accuracy of the Pc model was lower than that of Mishra et al. (2009). This discrepancy could be related to other factors (water turbidity, dissolved organic matter or contamination of water leaving radiance signal by surrounding vegetation) that could negatively influence our field spectral measurements.

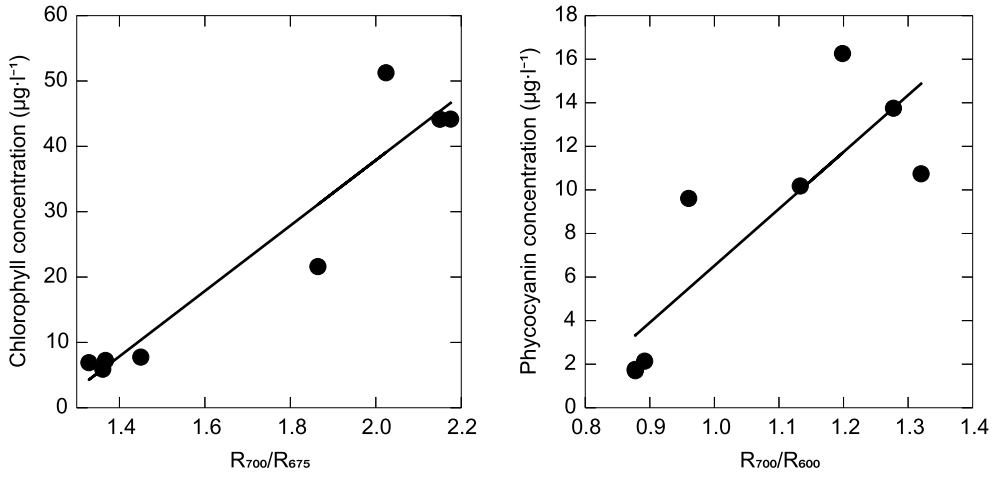

Figure 5.3 Linear relationship between field measured concentration of chlorophyll (a) and phycocyanin (b) and two spectral indices that were calculated from in-situ spectral data.

The chlorophyll and the phycocyanin concentrations were mapped using the following equations:

$$C_a = 50.03 \frac{R_{700}}{R_{675}} - 62.19, \qquad R^2 = 0.90, \tag{5.1}$$

$$Pc = 26.10 \frac{R_{700}}{R_{600}} - 19.58, \qquad R^2 = 0.73. \tag{5.2}$$

The established equations were consequently applied on a per pixel basis to the entire hyperspectral image of the Brno reservoir (Figure 5.4). The maps exhibit similar spatial pattern of C_a, as well as of Pc concentration. This could

be expected, as both pigments correlate to each other (Randolph et al. 2008). The highest concentrations were observed close to the dam, which is the place of the highest accumulation of slowly-floating phytoplankton and the shores that are used for recreational purposes. Both the maps indicate quite low concentrations of C_a and Pc for most of the reservoir area except those close to the dam and at Zouvalka site. This was also confirmed by the field measurements when concentrations of C_a and Pc are higher in the dam area than the remaining sampling locations (Table 5.1). Figure 5.5 shows a contribution of main phytoplankton groups to the total chlorophyll concentration at Zouvalka and dam sites obtained from active FluoroProbe measurements.

Table 5.1 Water quality indicators measured in-situ at Brno reservoir in September 2013.

Locality/Water characteristics	**Number of samples**	**Chlorophyll ($\mu g\,l^{-1}$)**	**Phycocyanin ($\mu g\,l^{-1}$)**
Open water area	6	6.4±0.12	4.45±0.15
Zouvalka	2	20.7	10.2
Dam area	2	32.7	10.7

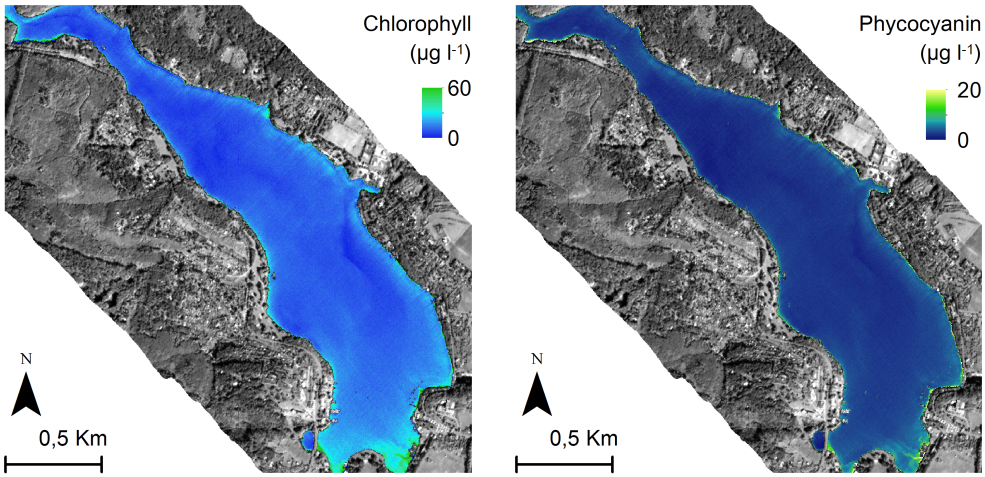

(a) **(b)**

Figure 5.4 Maps of chlorophyll-*a* (a) and phycocyanin concentrations (b) in the Brno reservoir assessed from the AISA hyperspectral images. The dam site is situated at the right lower corner of the map and Zouvalka site above the upper left corner, outside the map area.

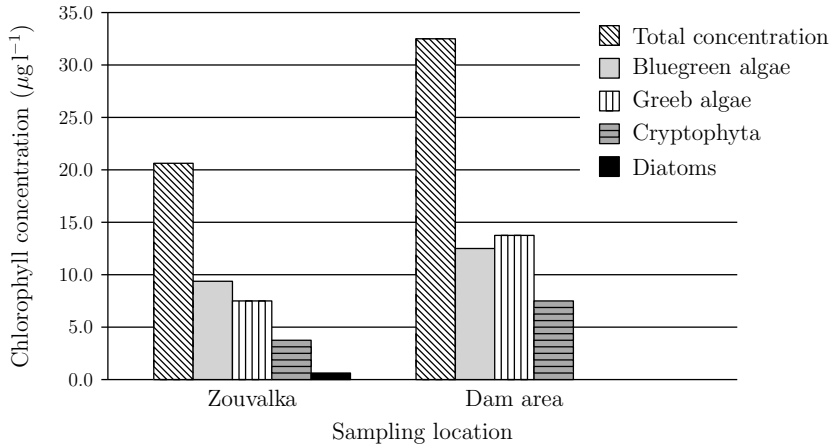

Figure 5.5 Contribution of phytoplankton groups to total chlorophyll concentration at two locations with elevated chlorophyll concentration as measured by FluoroProbe.

5.4 Conclusions

The study demonstrates that airborne hyperspectral data can be used to map spatial distribution of water blooms of algae and cyanobacteria using spectral indices sensitive to chlorophyll and phycocyanin concentrations. The empirical models developed here could be successfully applied on airborne imagery data from different time of data acquisition if the distribution of other optically active substances in water does not differ significantly from the conditions of this study. A solution to the problems of variable conditions would be to build up an integrated framework of complementary field and airborne observations, where rapid measurements of field data would be used to update the existing empirical model. The measurements from such a system could be also used in calibration of physically based radiative transfer (RT) model. And even RT model is typically sensitive to precise parameterization it can be used for water bodies at different sites.

Recommended Reading

Chorus, I. 2001. *Cyanotoxins: occurrence, causes, consequences.* Springer - Verlag Berlin Heidelberg.

Lindell, T., Pierson, D.C., Premazzi, G. & Zilioli, E. 1999. *Manual for monitoring European lakes using remote sensing techniques (Report EUR 18665 EN).* European Communities. Office for Official Publications of the European Communities, Luxembourg.

Richardson, L.L. & LeDrew, E.F. (Eds.) 2006. *Remote sensing of aquatic coastal ecosystem processes.* Springer.

6

MAPPING OF OVERBURDEN SUBSTRATES FOR MINE SITE RE-CULTIVATION

Jan Frouz, Miroslav Pikl, Olga Vindušková, and František Zemek

6.1 Introduction

Open pit coal mining has a severe impact on ecosystems in the mining area. An ecosystem affected by opencast mining is literally erased, either excavated or buried. Overburden (spoil) overlying the coal seam is removed and deposited in heaps leading to disruption of large areas (Bell & Donnelly, 2006). In many cases, overburden material becomes the parent substrate for soil development (Šourková et al. 2005; Karu et al. 2009).

This overburden material comes often from large depth, often over hundred meters. These substrates differ substantially from recent soils. They often have extreme pH (too acidic or too alkaline), extreme texture (gravel, sandy or clay), and in many cases the material is separated in terms of grains of similar size. In some locations overburden material may contain high concentrations of heavy metals and or may have high salt content reflected in high conductivity. The substrates often lack recent organic matter but may contain fossil organic matter of

various origin (Bradshaw 1997).

Contrary to other polluted sites where toxicity appears as a result of the accumulation of exogenous toxic substances, in post-mining sites the toxicity is typically a result of in situ weathering. Weathering, namely pyrite oxidation, decreases pH and may release heavy metals. Weathering may also release other ions that may cause high conductivity of the substrate resulting in toxicity of post mining sites (Bradshaw 1997; Frouz et al. 2005). Determination of potential toxicity of post mining sites is important for prediction of their future development. For example in Sokolov coal mining district in nontoxic sites, vegetation coverage can be reached by proper reclamation in 5-10 years and even spontaneous succession processes lead to vegetation cover in 10–15 years (Frouz et al. 2014), whereas in sites with high pyrite oxidation, vegetation may not appear for next 50 years (Frouz et al. 2014).

Biological tests with overburden material show that its toxicity in Sokolov area is most closely associated with pH, conductivity and polyphenol content. Primary cause of pH decrease is usually pyrite weathering. Pyrite in coal mining sites is usually associated with the coal seam; consequently, toxicity problems are typically the most severe in substrates that contain traces of coal. Identification of coal may thus be a good indicator of toxicity. This effect may be enhanced in materials with low sorption capacity, and low content of basic cations such as in sand or kaolinite. Besides toxicity associated with coal accompanied by pyrite, there may be also other mechanisms causing toxicity, e.g., sites with high conductivity given by high content of carbonates and sulfates may be toxic for plants and soil fauna due to high osmotic pressure (Frouz et al. 2005).

Identification of fossil organic matter (FOM) and characterizing its quality may be important in identifying potentially toxic sites. After reclamation or during spontaneous recovery of the vegetation cover, the content of recent soil organic matter (RSOM) gradually increases (Šourková et al. 2005). This has positive impacts on soil quality (increases porosity, aeration, water capacity of soil and infiltration). RSOM also represents an energy and nutrient source for soil biota (Brady & Weil 1999); moreover, RSOM represents a carbon sink and may reduce the rising concentration of CO_2 in the atmosphere (IPCC 2007).

The amount of RSOM in soils is determined as organic carbon content. However, in mine soils fossil forms of organic carbon such as coal or kerogen can also be frequently found (Vindušková & Frouz 2013). Conventional methods for soil organic carbon determination unfortunately cannot distinguish between recent and fossil carbon forms. The only method suitable for such differentiation is radiocarbon dating. However, this method is very expensive, thus it cannot be used routinely. Proximal remote sensing techniques such as near infrared spectroscopy (NIRS) hold potential to discriminate between recent and fossil carbon forms.

In general, remote sensing techniques are useful in the study of many soil properties (Ben-Dor et al. 1997; Mulder et al. 2011). However, a common problem with the study of soil properties using airborne devices is that soil is

often covered by vegetation and if the soil is bare, the surface layer of the soil is often covered by physical or biological crusts that may have different properties than deeper soil horizons. In this aspect, post mining areas are ideally suited for using remote sensing tools as they have a large area of bare soil which often was quite recently homogenized during the heaping process. Moreover, for many key processes such as erosion or plant establishment, the conditions of the surface layer are more important than conditions in deeper soil.

In this chapter, we illustrate the possible application of remote sensing techniques to map post mining substrates having various types of potential toxicity or even to directly predict the toxicity of post mining sites and estimate content of fossil and recent organic matter.

6.2 Material and Methods

6.2.1 Study Area

Two set of post mining sites were used in this study. The first set consists of 42 sites described in (Frouz et al. 2005). These were sampled in three mining districts: 1. Sokolov – coal-mining district near the towns Sokolov and Chodov (North-West Czech Republic), 2. North Czech coal mining district near Bílina and Ústí nad Labem (North Bohemia), and 3. Lusatian mining district near Cottbus (Eastern Germany). Both Czech areas are brown coal mining district whereas lignite is mined in Germany near Cottbus. In all sites, open cast mines produce large areas of tailings where spoil material was sampled. In both Czech coal-mining districts, claylike tertiary sediments dominated, whereas sand was most frequent in German mining district. This set was used for comparison of chemical and ecotoxicological characterization of substrates with laboratory spectral measurements.

The second set of plots was located in post mining plots near Sokolov (Czech Republic). Average altitude of the study area is about 500—700 m a.s.l. In majority of the heaps, the overburden consists mainly of tertiary clays of Cypris series with alkaline pH. These clays are dominated by kaolinite, illite and montmorillonite, and contain 2–10 % of fossil organic matter. In smaller extent, other substrates are present, namely neutral or slightly acidic tuffites, which are weathered, volcanic ashes of tertiary origin underlying the coal seams, acidic clay substrates dominated with kaolinite, coal and acidic coal rich kaolinite clays, and finally jarosite crusts on tertiary clay substrates. This set, covering a part of the heap of an area about 0.5 ha, was used for comparison of chemical and ecotoxicological characterization of substrates with field measurements of spectra, along with the first set. In addition, this set was used for classification of substrates based on airborne hyperspectral data. In this part of the heap, substrates were mapped by field survey and pH was measured in a regular 25×25 m grid.

6.2.2 Laboratory Chemical and Ecotoxicological Characterization of Substrates

The material for chemical analysis was air-dried and stored in a dark place at room temperature. Soil pH in water was measured using a pH meter with glass electrode, conductivity was measured in filtrated 1:5 spoil water suspension using a conductometer. Two ecotoxicity tests were applied, i.e., germination of plant *Sinapis alba* and enchytraeid toxicity test. *S. alba* germination was tested with a pot experiment similar to that used by Fargasová (Fargasová 1994; Fargasová 1998). The test is based on proportion of seeds that germinate on given substrate. The enchytraeid toxicity test was conducted as described by Frouz et al. (Frouz et al. 2005); this test measures growth of population of potworms in individual substrates from constant number of introduced even-aged potworms.

6.2.3 Spectral Data

A. Laboratory spectral measurements

Spectral signatures of 42 clay substrates collected at the first site were measured in a laboratory. The samples were dried and sieved through 2 mm calibrated sieve. The samples were measured in black Petri dishes with ASD FieldSpec 3: spectral range 350–2500 nm, sampling step 1 nm, full width at maximum half – FWHM 3 nm. The Petri dishes with soil samples were placed on a turntable (ASD Inc.) ensuring that measured spectra were homogenized (average of 50 measurements) and all samples were measured with the same viewing and illuminating geometry. White reference panel (Spectralon®) was used to obtain reflectance data directly. Measured spectra were corrected using dynamic, parabolic linear transformation (Beal & Eamon 2009) in order to compensate the shifts between visible and infrared regions.

To generate a model relating laboratory spectral data with substrate pH or toxicity, two steps were used. In the first step, the correlations between reflectance of substrates at individual wavelengths and pH and toxicity were calculated. Then we identified all local correlation minima or maxima as a function of wavelength. From these, we selected individual wavelengths or mean wavelengths for a certain interval if correlation formed a rather flat plateau. These values were then the subject of multiple regression analysis with forward selection in Statistica 10.

B. Field spectral measurements

Field reflectance measurements (ASD FieldSpec 3) of nine substrates were carried out at 14 homogenous plots in the second test area (Sokolov region). We used the white reference panel (Spectralon®) before and after each substrate measurements to obtain directly surface reflectance signatures. The parabolic linear transformation was carried out on measured spectra.

Each plot spectrum was calculated as an average of about 15 individual measurements as some measurements were identified as outliers. ASD measurements were resampled to fit the spectral resolution of the hyperspectral airborne data described in the next section.

C. Airborne spectral measurements

Airborne hyperspectral data over the second site (Sokolov region) were acquired on August 6th 2008 using AISA Eagle pushbroom hyperspectral system with spatial resolution 0.4 m, spectral resolution of 10 nm within spectral range of 400–1000 nm. Ancillary field data were collected simultaneously with the overflight. Field data supported atmospheric and geometric corrections of airborne images (see Section 2.3 for details).

We used CaliGeo (Spectral Imaging Ltd.) software to carry out the radiometric corrections and orthorectification of the raw AISA Eagle image data. ATCOR-4 software was applied for atmospheric, topographic and BRDF corrections of airborne data.

6.2.4 Mapping of Clay Substrate Composition

We used spectral angle mapper classifier (SAM) to classify soil substrates from the hyperspectral image. SAM is a method for comparing imagery spectra to a spectrum representing the class (Kruse et al. 1993). Training spectra for individual substrate classes were taken from the field ASD measurements described in 6.2.3. The SAM classification was implemented in ENVI using a multiple threshold option. A threshold value was set up for each substrate class. The regions of interest (ROI) were determined based on the known positions of substrates in the area and average value of spectral angle was calculated for a given ROI.

6.2.5 Fossil Organic Matter Characterization Using Near Infrared Spectroscopy

Near infrared spectra were laboratory measured in a spectral range from 1000 to 2500 nm. Artificial mixtures ($n = 125$) of claystone, coal and recent organic matter (from fermentation layer) were measured as well as a set of 14 soils in which recent carbon was previously determined by radiocarbon dating (Karu et al. 2009). The recent carbon content in mixtures was calculated from the proportion of recent organic matter and its total organic carbon content. The total organic carbon content in mixtures was calculated as a sum of organic carbon from claystone, coal and recent organic matter.

Partial least squares (Janik et al. 2007) was used to develop calibration models between reflectance and total organic carbon (Ctot) and recent carbon (Crec) content — first using only the mixtures, then adding also the soil spectra.

6.3 Results and Discussion

6.3.1 Spectral Signatures of Different Clay Substrates Measured in a Lab and Their Relation to Chemistry and Toxicity

Earlier studies (Frouz et al. 2005; Frouz et al. 2011) show that conductivity and pH are major factors contributing to substrate toxicity for representatives of both soil fauna and plants. Using multiple regressions with forward selection, we were able to produce an equation that predicts pH of overburden from laboratory spectroscopic data (Figure 6.1) obtained in three mining sites (Table 6.1). Despite the fact that this approach was very successful in determining pH (the equation is highly significant and explains more than 80 % of data variability), the attempt to explain toxicity the same way was much less successful. Although the resulting equation was also statistically significant it explained only 23 % of data variability. This discrepancy between successful estimate of pH and less successful estimate of toxicity is caused by fact that the toxicity of post-mining sites is quite complex as several environmental factors and their combinations contribute to the final toxicity of the substrate (Frouz et al. 2005; Frouz et al. 2011). The most frequent reason for the toxicity is a low pH. Low pH also increases the solubility of aluminium and other metals which may contribute to the toxicity of substrates. This indicates that the effect of pH may be modified by the presence of metals, namely As. High conductivity caused by the high concentration of cations, namely Na, is another reason for high toxicity. The high conductivity is sometimes accompanied by a high pH. Finally, toxicity is often accompanied by coal, as coal content closely negatively correlates with pH but potentially may affect soil biota also directly through polyphenols in coal (Frouz et al. 2005). This complexity of toxicity is a reason why the attempt to estimate toxicity as a simple function of spectral properties did not meet with much success.

6.3.2 Spatial Distribution of Clay Substrates Using AISA Eagle Images and Their Use for Prediction of Toxicity

Geological substrates forming the overburden have similar chemical properties and toxicity values (Frouz et al. 2005) and are often distinct from other substrates. Because toxicity is very complex problem, as was explained above, it seems to be more promising to use hyperspectral data to classify prevailing overburden substrate and then estimate potential toxicity based on mean values of toxicity for individual overburden substrates. Classification of individual overburden substrate types from airborne hyperspectral data was done using spectral angle mapper. Overall classification accuracy was 71.18 %. Classification results for each substrate are presented in Table 6.2. Clay substrates of the Cypris series were divided for the purpose of classification into yellow and grey subclass. Both dominate the area and these subclasses reached the highest classification accuracy.

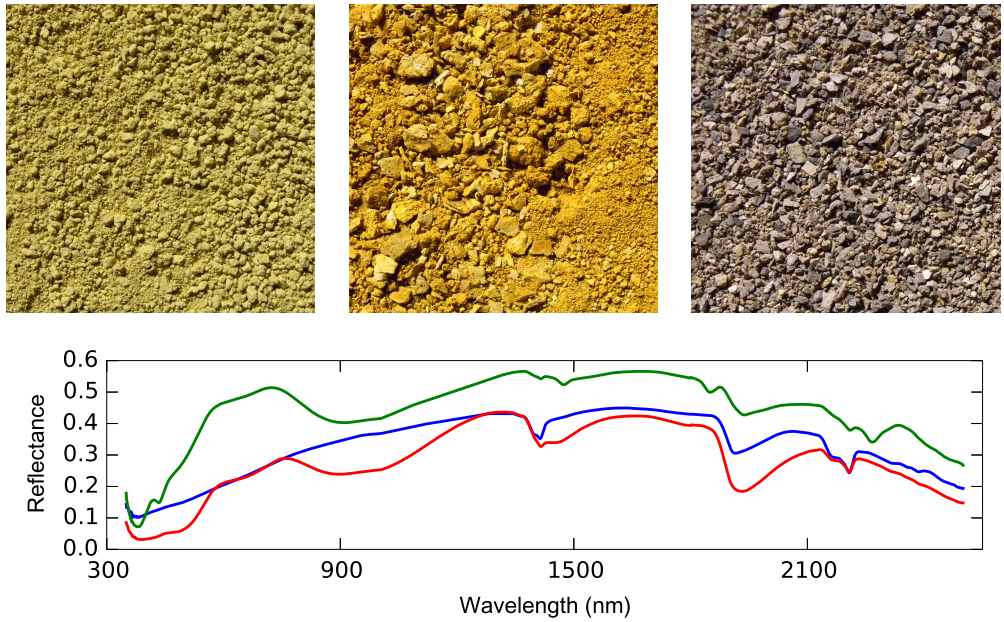

Figure 6.1 Samples and spectra of selected clay substrates: Top left image, green line in plot above – yellow clay (illite + jarosite). Top middle, red line – jarosite crust. Top right, blue line – coal clay (kaolinite + coal)

This classification was then used to produce a map of substrates in about one ha area of Podkrušnohorská heap with large variety of substrates (Figure 6.2). In this area, 14 samples were randomly taken and their toxicity was tested by *Sinapis alba* germination test. The combination of average substrate toxicity with the substrate map obtained from hyperspectral data gives us spatial prediction of substrate toxicity. Comparison of toxicity predicted using hyperspectral data and measured toxicity in these 14 points indicates that predictions of substrate toxicity using hyperspectral data with substrate classification explains about 55 % of data variability. This is greater than toxicity as predicted on basis of pH value extrapolated from regular grid of points, which explains only 21 % of data variability.

The reason why hyperspectral mapping is much more successful in this context is connected with the manner in which the heap was created. Individual piles of material of different origin are heaped in various shapes and in sizes which are below the resolution of the 25×25 m grid. Edges of these piles are very narrow and basically unpredictable by classical interpolation techniques.

Table 6.1 Results of multiple regression estimating substrate (a) pH and (b) toxicity based on laboratory hyperspectral data.

a)

Wavelength	Coefficient	SD[a]	p[a]
intercept	9.46	0.95	< 0.0001
1270	-247.23	156.80	0.1241
435–450	88.59	13.67	< 0.0001
380–385	-105.61	18.59	< 0.0001
350	-7.94	9.10	0.3891
1880–1885	76.09	11.84	< 0.0001
1425–1430	-106.47	17.97	< 0.0001
1249	265.60	160.15	0.1064

b)

Wavelength	Coefficient	SD[a]	p[a]
intercept	0.76	0.23	0.0024
1290	-2.00	0.62	0.0026
435–450	7.09	3.47	0.0481
380–385	-6.48	4.33	0.1427

[a] SD – standard deviation, p – probability

Table 6.2 Classification accuracies for overburden substrates in Podkrušnohorská post mining heap near Sokolov.

Substrate	Producer accuracy[a] [%]	User accuracy[b] [%]
coal clay	97.76	51.82
clay of cypris series – yellow	100.00	99.76
tuffites	48.85	100.00
kaolinitic clays	76.49	99.48
underlying soils	27.27	25.53
clay of cypris series – grey	93.42	85.34
coal with clay	50.00	97.40
coal	60.89	100.00
Jarosite cover on clay	49.02	100.00

[a] Producer accuracy results from dividing the number of correctly classified pixels in each class by the number of training pixels used for that class.

[b] User accuracy results from dividing the number of correctly classified pixels in each category by the total number of pixels that were classified in that class.

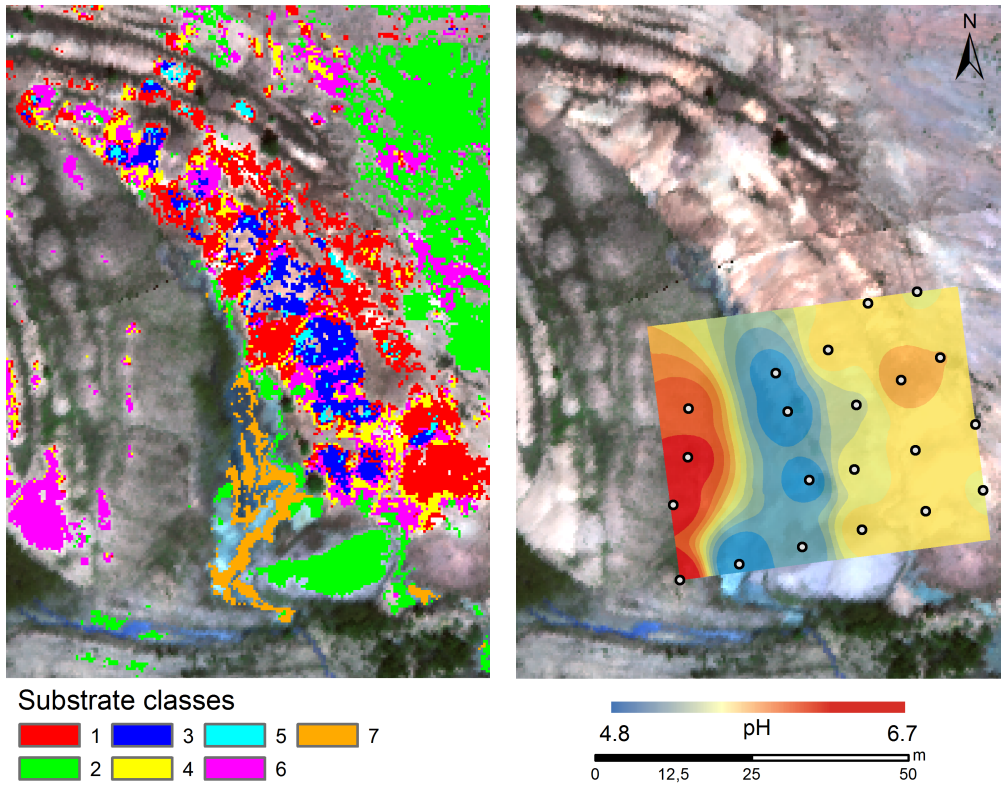

Figure 6.2 Map of substrate classification obtained from hyper spectral data and pH interpolated from field measurements. Numbers in the left mark type of substrate: 1 – coal clay, 2 – clay of cypris serie yellow, 3 – tuffites, 4 – underlying soils, 5 – kaolinite clay, 6 – clay of cypris serie grey, 7 – jarosite. Scale at the bottom shows pH color coding.

6.3.3 Can Near Infrared Spectroscopy Distinguish Between Recent and Fossil Organic Matter in Mine Soils?

To find out if content of recent and fossil organic matter can be predicted from near infrared spectra, predicted values of recent and total organic carbon were compared with their true values (measured by radiocarbon dating and elemental analysis).

Calibration models based only on artificial mixtures could not predict recent nor total organic carbon in soils successfully. However, addition of soil spectra to the calibration improved the predictions considerably – as indicated by root mean square error of cross-validation (RMSECV) and modeling efficiency (EF) comparing explanatory power to model complexity. Models both for recent carbon (RMSECV=0.70, EF=0.95) and total organic carbon (RMSECV=0.85, EF=0.94) were highly successful (Loague & Green 1991; Michel et al. 2009). Parameters of the derived calibrations are similar or better than those reported by other authors who recommend NIRS for measurement of different carbon fractions (Bornemann

et al. 2008; Michel et al. 2009).

The improving effect of soil spectra in calibrations indicates that the spectra of the mixtures and soils differ significantly, i.e. have different spectral features. This is understandable as we may expect that recent organic matter in soils is older and thus more decomposed and fossil organic matter in soils may be modified by weathering and decomposition. The soil samples may be also more variable in mineral composition which may also affect the soil spectra.

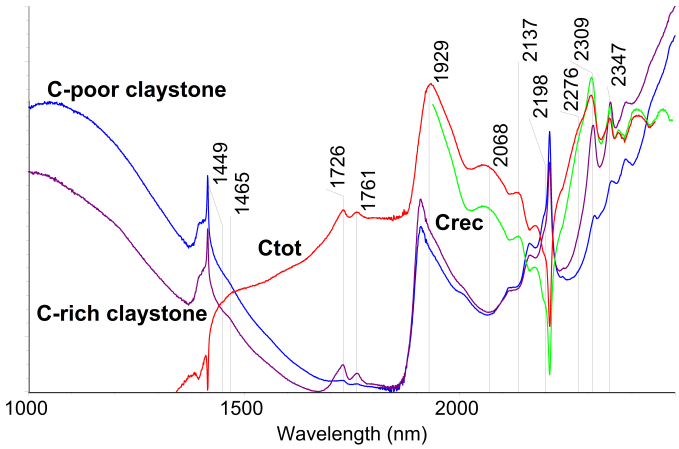

Figure 6.3 First loading spectra of calibrations for total organic carbon (Ctot) and recent carbon (Crec) together with spectra of C-poor and C-rich claystone.

The most important spectral features for the prediction of recent and total organic carbon are depicted as first loading spectra resulting from partial least square regression (Figure 6.3). The peaks observed can be well assigned to characteristic absorptions of soil organic matter in the near infrared region that have been previously described in literature (Ben-Dor et al. 1997; Michel et al. 2009; Stenberg et al. 2010); their assignments are listed in Table 6.3. For example, it is visible even to naked eye that absorption characteristics of aliphatic structures (1726 and 1761) are more pronounced in C-rich than in C-poor claystone. The same features are visible in the Ctot loading spectrum. This corresponds well with the aliphatic character of fossil organic matter in the studied area, which is mainly kerogen of algal origin (Kříbek et al. 1998).

6.4 Conclusions

This contribution demonstrates the usefulness of remote sensing techniques in studying post mining sites and at the same time the large potential of these techniques for practical applications.

Classification of overburden substrates brings much better prediction of spatial

Table 6.3 Band assignment (after Ben Dor et al., 1997; Michel et al., 2009; Stenberg et al., 2010;)

Wavelength (nm)	Assignment	Possible constituent
1449	4ν of C=O	carboxylic acids
1465	OH in water ($\nu_2 + \nu_3$); CH_2	cellulose/lignin/starch/ pectin
1582	OH in water (2ν); H-bonded OH group	pectin/starch/cellulose
1726	2ν of aliphatic C-H stretch	cellulose/lignin/starch/ pectin/wax/humic acid
1761	2ν of aliphatic C-H stretch	cellulose/lignin/starch/ pectin/wax/humic acid
1929	OH in water ($\nu_1 + \nu_3$); 3ν of -C=O and of -COOH, C=O of ketonic carbonyl, $CONH_2$	cellulose/lignin/glucan/ pectin/wax/humic acid
2068	3ν of aromatic C=C, COO-hydrogen bond, C=O	cellulose/glucan/pectin
2137	3ν of aromatic C=C, COO-hydrogen bond, C=O	cellulose/glucan/pectin
2198	3ν of aromatic C=C	starch/lignin/wax/tannins
2276	combination of O-H stretch and C-O of cellulose; combination of C-H stretch and CH_2 deformation of starch	
2309	3ν of aliphatic C-H, aromatic ring stretch	humic acid/wax/starch
2347	3ν of aliphatic C-H	cellulose/lignin/glucan

distribution of substrate toxicity than interpolation of chemical properties that give best correlation with toxicity from field surveys. There can be a potential to improve the prediction of toxicity by including some auxiliary environmental parameters related to orographic features (e.g. latent drainage system, slope).

Near infrared spectroscopy combined with partial-least squares provides accurate estimates of recent and total organic carbon in mine soil samples. This method may offer a simple, rapid, and low-cost alternative to expensive and time-consuming radiocarbon dating.

Recommended Reading

Ben-Dor, E., Chabrillat, S., Dematte, J.A.M., Taylor, G.R., Hill, J., Whiting, M.L. & Sommer, S. 2009. Using Imaging Spectroscopy to study soil properties. *Remote Sensing of Environment* 113: S38–S55.

Boettinger, J.L., Howell, D.W., Moore, A.C., Hartemink, A.E. & Kienast-Brown, S. 2010. *Digital Soil Mapping.* Springer, 473 p.

Brady, N.C. & Weil, R.R. 1999. *The nature and properties of soils.* Prentice Hall, Upper Saddle River.

Mulder, V.L., de Bruin, S., Schaepman, M.E. & Mayr, T.R. 2011. The use of remote sensing in soil and terrain mapping – A review. *Geoderma* 162: 1–19.

Stenberg, B., Viscarra Rossel, R.A., Mouazen, A.M. & Wetterlind, J. 2010. Chapter Five - Visible and Near Infrared Spectoscopy in Soil Science. *Advances in Agronomy* 107: 163–215.

Ussiri, D.A.N., Jacinthe, P.-A. & Lal, R. 2014. Methods for determination of coal carbon in reclaimed minesoils: A review. *Geoderma* 214-215: 155–167.

7

APPLICATION OF REMOTE SENSING IN PRECISION AGRICULTURE

Vojtěch Lukas, Fernando Rodriguez Moreno, František Zemek, Petr Hlavinka, Jan Křen, Daniela Semerádová, and Zdeněk Žalud

In recent years agricultural entrepreneurs farm about 4,264 million ha of land in the Czech Republic, approximately half (54 %) of the total area of the country. The predominant fraction of this area (3 million ha, 71 %) is cultivated as arable land on which individual crops are rotated. The arable land of the Czech Republic with high intensity of crop production has specific traits. Large areas of cultivated fields with a combination of high variability of topographical and geological factors result in higher heterogeneity of soil condition and crop yield. More than 54 % of agricultural land is managed by farms with a size of over 1000 ha (Ministry of Agriculture 2010). Based on a statistical evaluation of the Land Parcel Information System (LPIS), over 40 % of arable land has a field size larger than 20 ha. Crop management in these conditions requires advanced decision making, such as precision agriculture.

Site specific management, known as precision agriculture, is an internationally unified term for directions of land management using new technologies that

began to be developed in the eighties and early nineties of the twentieth century. The aim of precision agriculture is an optimization of production inputs (fertilizers, pesticides, fuel, etc.) based on the local crop requirements and soil condition. Crop management in this way can lead to economically efficient use of agrochemicals and minimization of environmental risks. Site specific management takes into consideration spatial variability within fields and optimizes the production inputs (Figure 7.1), thus fulfilling the objectives of sustainable agriculture (Corwin & Plant 2005).

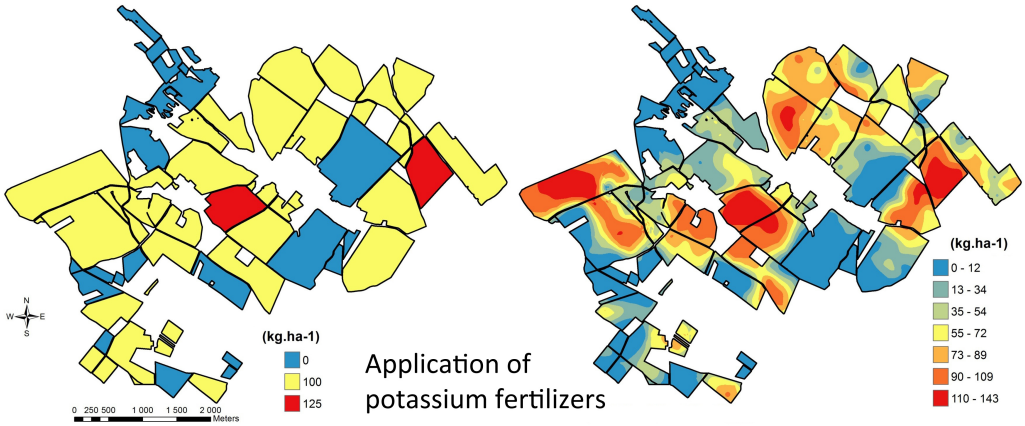

Figure 7.1 An example of uniform (a) versus variable application (b) of potassium fertilizers at the farm with the 1500 ha of arable land. The application rates are tailored according to the nutrient content in soil (adapted after Lukas et al. 2011b).

Basic principles of precision agriculture are not new, the spatial and temporal variability of soil and crop was recognized by farmers many centuries ago. Smaller parcels with natural boundaries allow changing the agrotechnical treatments manually. With a merging of small parcels into large blocks, intensification of production, and mechanization in the middle of the last century, it was no longer possible to take into account the spatial variability without modern technologies. Global navigation satellite systems (GNSS), information and communication technologies (ICT) and satellite/airborne remote sensing, together with geographic information systems (GIS) significantly contribute to collection and processing of information necessary for precision management of agricultural crops.

The importance of evaluation of spatial variability within the fields

Pierce & Nowak (1999) consider assessing variability as the critical first step because "one cannot manage what one does not know". The factors and properties that regulate crop growth and yield vary in space and time. The higher is the spatial variability of a soil conditions (or crop properties), the higher is the potential for precision management and the greater its potential value. The degree

of difficulty, however, increases with higher dynamics of the temporal component.

The consequences of site variability are most reflected in the crop yield. The variability of yield represented by yield maps can serve as input information for decisions about site specific management. If the cause of yield variability is not known, uniform crop management is suggested (Adamchuk et al. 2010, Figure 7.2). Site specific management can be recommended if the spatial structure of yield differences are consistent over multiple years and correspond to some agronomically important phenomena (nutrient supply, topography, land use history, etc.).

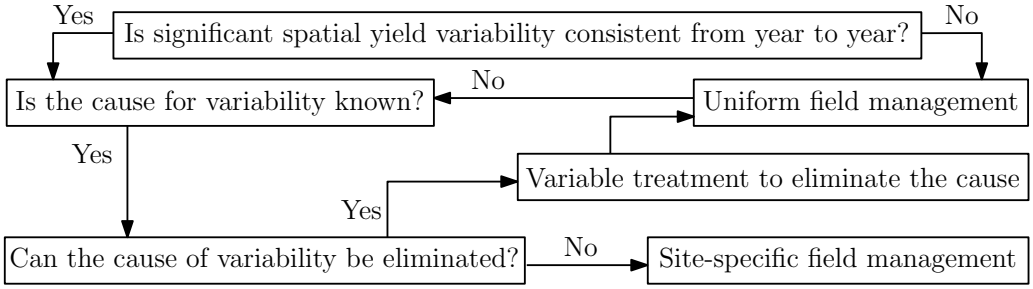

Figure 7.2 Yield-based decision making tree for application of site specific management (adapted after Adamchuk et al. 2010).

7.1 Mapping of Spatial Variability of Soil Properties Within the Fields

The conventional techniques of soil variability mapping are slowly being replaced by indirect methods such as the on-the-go systems (see overview by Adamchuk et al. (2004)) or remote sensing. These methods have better spatial coverage but are less accurate compared to field sampling followed by laboratory procedures (Christy 2008).

For the on-the-go method, soil electrical conductivity (EC) has become one of the most frequently used measurements to characterize field variability for application to precision agriculture (Corwin & Lesch 2003). Soil conductivity is influenced by combination of physical and chemical properties including soluble salts, clay content and mineralogy, soil water content, bulk density, organic matter, and soil temperature (Corwin & Lesch 2005). A number of factors complicate the direct application of EC in site specific management, because the interpretation of EC maps requires the determination of the dominant soil factor (Figure 7.3).

Mapping techniques based on remote sensing data are extensively used. These techniques use the spectral characteristics of the soil surface to infer soil heterogeneity. Baumgardner et al. (1985) presents an overview of spectral properties of soil. Similar to other geophysical methods, remote sensing cannot be used to determine specific soil properties without additional soil survey data. Spectral

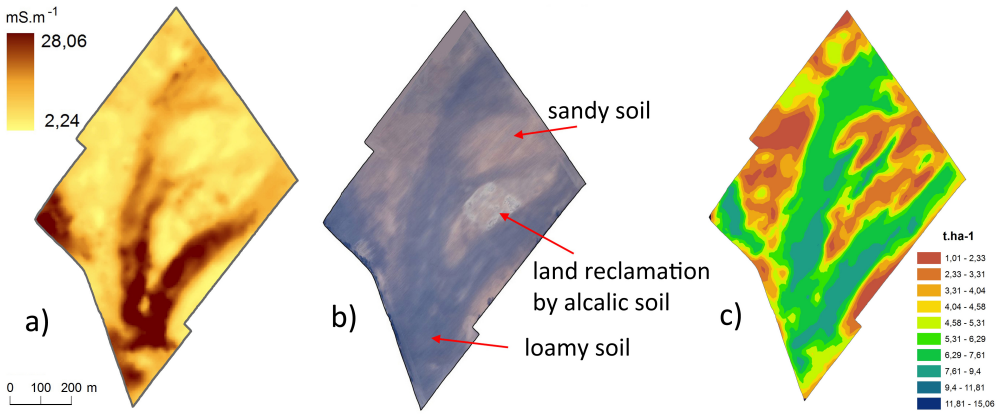

Figure 7.3 Map of soil electrical conductivity (a), aerial image in visible spectrum (b) and yield variability (c) at 52-ha field all showing similar spatial pattern (adapted after Lukas et al. 2011a).

characteristics of the soil surface are influenced by many factors, mainly by content of soil organic matter, soil moisture, soil texture, content of iron oxides (Lilienthal 2003), and surface roughness (Lillesand et al. 2008). Detailed descriptions of the effects of soil factors are given in Baumgardner et al. (1985), Lilienthal (2003), van der Meer & de Jong (2006) and Ben-Dor et al. (2009).

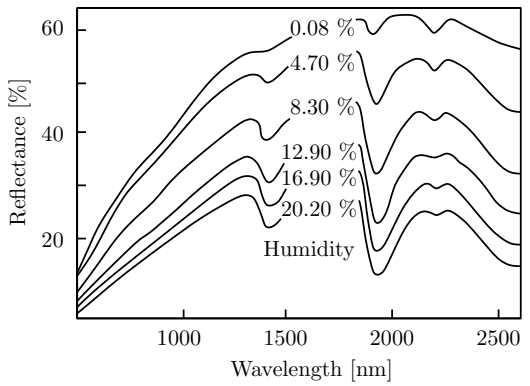

Figure 7.4 The effect of soil moisture on soil reflectance (adapted after Lilienthal 2003).

An increase of soil moisture generally decreases the reflectance, mainly in visible spectrum part (400–700 nm). Wet soil looks darker than dry soil. There are characteristic absorption features of EM in the soil spectral response curve around 1400 and 1900 nm due the water content (Figure 7.4). A higher content of organic matter causes a decrease in the reflectance across the whole VNIR spectrum (Figure 7.5) (Baumgardner et al. 1985).

In the case of soil texture the increasing size of soil particles generally increases

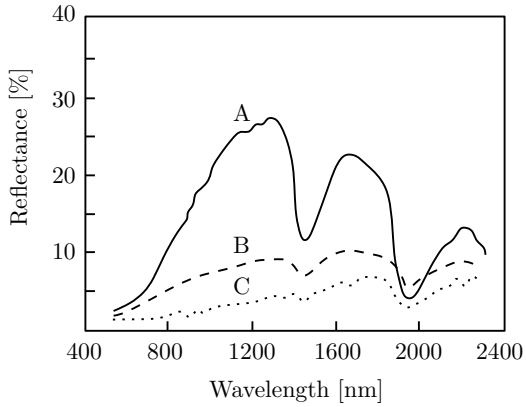

Figure 7.5 Spectral characteristics of soil with different content of soil organic matter (SOM): A – fibric soil with low content of SOM; B – hemic soil; and C – sapric soil with higher SOM content (adapted after Baumgardner et al. 1985).

the soil reflectance in visible spectrum. Loamy soils are darker in comparison to sandy soil. The size of soil particles influences some other soil properties, such as soil moisture and structure, which also affect the resulting soil reflectance. That is why the exact determination of soil texture from RS data is difficult (van der Meer & de Jong 2006). The classification of soil texture from hyperspectral images can be improved by timing remote surveys when the soil is in optimal wet conditions in order to maximize the differences between soil types (Casa et al. 2013).

Although remote sensing and geophysical mapping work on different physical principles they can provide similar results. De Benedetto et al. (2013) show that a combination of both methods can be successfully used to identify areas within the fields having similar production conditions, the so-called management zones.

7.2 Assessment of Crop Variability by Remote Sensing

In agriculture, mapping of vegetation by remote sensing could be used for additional purposes, such as classification of land use, identification of crop species, estimation of nutrition and water status of crops, and prediction of crop yields. The spectral characteristics of plants and canopy stands are described in Chapters 1 and 2. This description is mainly valid for healthy (green) vegetation. For plants under stress or senescence there is typically an increase of reflectance in the red part of the spectrum and a decrease in NIR (Figure 7.6). Spectral measurements are able to detect the changes in vegetation under stress (deficit of water or nutrition, disease infestation), but usually without being able to determine the exact cause of the stress.

The visible and the near infrared part of EM have been used in a number

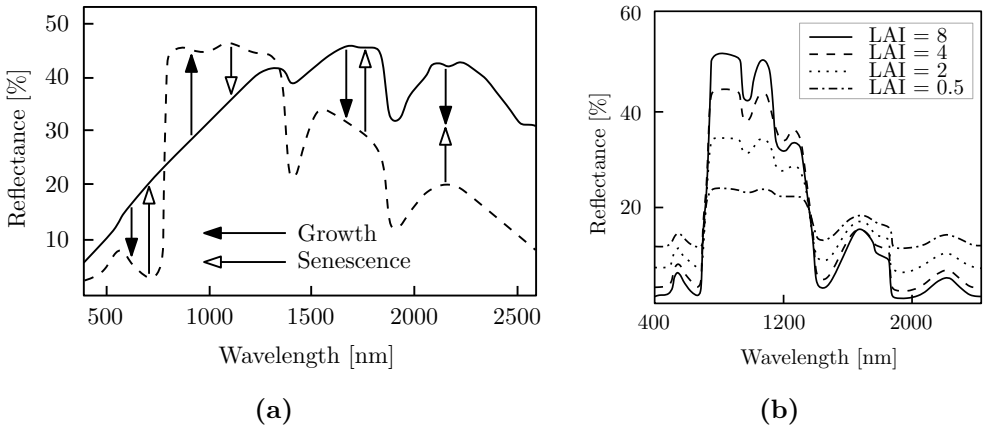

Figure 7.6 Changes in spectral curves of vegetation (adapted after Lilienthal, 2003): (a) during growing and senescence stage and (b) affected by different amount of biomass - leaf area index (LAI).

of studies for linking spectral reflectance and plant biophysical parameters via vegetation indices (VIs). For example Li et al. (2014) present a list of vegetation hyperspectral indices, which can be used for estimation of canopy nitrogen content of winter wheat. In our case study we use four VIs, namely Normalized Difference Vegetation Index (NDVI), Red Edge Inflection Point index (REIP), Photochemical Reflectance Index (PRI), and Water Band Index (WBI) for assessment of homogeneity of crop canopy. Information about many other narrow-band VIs can be found in Chapter 8 (Table 8.1).

NDVI was originally developed for estimating the proportion of vegetation cover in shrubby area from broadband satellite data (Rouse et al. 1974). Normalization partially reduces some disruptive impacts on the imagery data, such as differences in scene illumination, shadows and atmospheric influences, because their effect is similar across the spectral bands. The equation for calculation of NDVI from broadband sensors is:

$$\mathrm{NDVI} = \frac{R_{NIR} - R_{Red}}{R_{NIR} + R_{Red}}, \tag{7.1}$$

where, R_{NIR}, R_{Red} are reflectances in NIR and red bands, respectively. When hyperspectral data are used, only selected bands with specific wavelength are chosen, typically R_{665} and R_{801}. The result of the calculation of NDVI is a dimensionless value from the interval between -1 and 1.

For example, the results of field experiments with winter wheat and spring barley have shown that higher positive NDVI values indicate a higher amount of aboveground biomass, plant weight, increased number of plants per m^2, number of tillers per plant, and improved nutritional status (higher chlorophyll content), all this resulting in higher crop yields (Křen et al. 2009).

The relationship between canopy density and NDVI is not linear because NDVI shows saturation at higher LAI (Baret & Guyot 1991). When reaching a certain level of LAI (or above-ground biomass), the value of broadband NDVI does not reflect the increase of canopy density linearly anymore and they decrease with vegetation senescence (Figure 7.7).

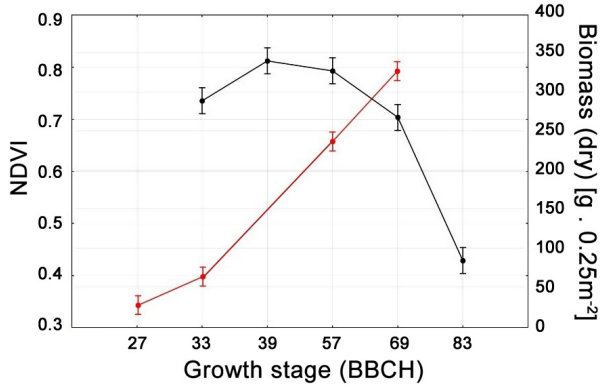

Figure 7.7 Relationship between broadband NDVI and biomass during vegetation period for winter wheat in 2013 (unpublished data from the authors).

One of the vegetation indices often used for estimation of nutrient status of field crops is Red Edge Inflection Point (REIP) or Red Edge Position (REP), which indicates the wavelength of the inflection point in the red edge part of spectrum. The position of this point is generally in the region 680–750 nm. An increase of chlorophyll concentration in plants or amount of biomass causes a shift of inflection point to higher wavelengths (Heege et al. 2008). A positive characteristic of REIP is lower sensitivity to interfering factors such as radiation reflected from soil background and atmospheric effects, together with high sensitivity to crop parameters (chlorophyll content and canopy biomass). Unlike NDVI, the REIP index does not saturate at higher values of LAI.

Several methods have been proposed for calculation of REIP (Miller et al. 1990; Cho & Skidmore 2006) as numerical calculation of the second derivative reflectance curves of vegetation or as linear interpolation according to the empirical equation proposed by Guyot et al. (1988) using four spectral bands:

$$\mathrm{REIP} = 700 + 40\frac{(R_{670} + R_{780})/2 - R_{700}}{R_{740} - R_{700}}\ [\mathrm{nm}]. \tag{7.2}$$

Sensitivity of REIP nitrogen concentration in leaves was observed in many recent studies. Mariotto et al. (2013) find that use of narrowband hyperspectral sensors provide 25 % greater variability in crop modelling and 20 % greater accuracy in crop discrimination compared to broadband sensors. Moreover, 3–7 narrow bands explained over 90 % of the variability in crop models. The results in Heege et al.

(2008) show a shift of REIP by 1 nm corresponds to a difference of 15 kg N applied in fertilizers 6 weeks before observation. However, determination of fertilization rate requires calibration each crop species, variety, vegetation stage and soil (field) conditions.

Gamon et al. (1990) proposed Photochemical Reflectance Index (PRI):

$$\mathrm{PRI} = \frac{R_{531} - R_{570}}{R_{531} + R_{570}}, \tag{7.3}$$

where R_{531} and R_{570} represent leaf reflectance at the subscripted wavelengths. PRI is often considered as a proxy of light use efficiency (LUE) during actual photosynthesis of vegetation. LUE reflects both the stand conditions and "vegetation vitality" at those stand conditions. Estimation of LUE is an important input to the model for calculation of gross primary productivity of ecosystems and carbon balance (Hilker et al. 2008).

The Water Band Index (WBI) is a reflectance index that is sensitive to changes in canopy water status. Its formulation uses the reflectance in the NIR at 900 nm and 970 nm by the specific absorption characteristics of water at these wavelengths and the ability to estimate the depth of light penetration (Penuelas et al. 1993):

$$\mathrm{WBI} = \frac{R_{970}}{R_{900}}. \tag{7.4}$$

As the water content of vegetation canopies increases, the strength of the absorption around 970 nm increases relative to that of 900 nm. Applications include canopy stress analysis, productivity prediction and modelling, fire hazard condition analysis, cropland management, and studies of ecosystem physiology.

7.3 Case Study

The aim of the study is to demonstrate application of airborne imagery spectroscopy in estimation of biomass and nutrition, and water status of cereals crop. The proximal and remote mapping of the crop nutritional status has a long tradition with a success rate ranging from medium to high depending on the conditions of the study. Information about the above-ground biomass provides high reliability for yield estimation, particularly in early growth stages (Křen et al. 2014). Nitrogen is the most important macronutrient for crop development, yield formation and final product quality, but with possible environmental risks from overdosing. A visual analysis of the spectral signatures can identify the differences between crops in different nutritional states, but for decision-making it is necessary to quantify these differences and one of the best ways to do this is to use vegetation indices.

The key objective of the study was to utilize spectral characteristics of crop canopy stand, obtained from hyperspectral imaging in the form of narrowband vegetation indices to estimate the crop parameters relevant for yield formation; in case of cereals mainly aboveground canopy biomass and chlorophyll content.

7.3.1 Data and Methods

For this purposes, a 62-ha field (predominant soil type chernozem) with spring barley in South Moravia region was chosen for ground and aerial survey during vegetation period 2014. The plant samples were taken at BBCH 32 growth stage (stem elongation) for estimation of above-ground biomass. Sampling was carried out in irregular sampling grid with 10 samples distributed within the fields by following the main soil zones. Simultaneously, estimation of nitrogen status of leaves was done by chlorophyll-meter measurement (Yara N-Tester). Yara N-Tester is based on the Minolta SPAD 502, which measures light transmitted by the plant leaf at two different wavelengths, 650 and 940 nm (Arregui et al. 2006). It became a common tool in agronomy praxis for diagnosis of plant N nutrient status and recommendation for nitrogen fertilizers application. Thirty random measurements were recorded to get the representative value in each sampling point, always following the recommendations of the manufacturer of the device. Each sampling point represented a circle of 5 m diameter.

(a) **(b)**

Figure 7.8 (a) Plant sampling of spring barley canopy stand at BBCH 32 and (b) chlorophyll-meter estimation of nutrition status of plants by Yara N-Tester.

The airborne data acquisition was carried out using hyperspectral sensor CASI-1500 (ITRES, Canada) with 96 spectral bands (365–1050 nm) and spatial resolution of 1 m per pixel. Image data were pre-processed for radiometric, atmospheric and geometric corrections. More details about HS data pre-processing can be found in Chapter 2. Vegetation indices were calculated for circle areas around sampling points using a zonal statistic tool. For this study, four indices were selected to verify the estimation of plant parameters: Normalized Difference Vegetation Index (NDVI), Red Edge Inflection Point (REIP), Photochemical Reflectance Index (PRI) and Water Band Index (WBI).

We used pre-processed airborne LiDAR data gridded with the resolution of 1 elevation point per 5 m pixel to calculate DEM and topographic characteristics such as elevation, slope, curvature, aspect and Topographic Wetness Index (TWI).

TWI quantifies soil moisture, giving the highest values to the sinks of a drainage system and lower values to the peaks following this equation:

$$\mathrm{TWI} = \ln\left(\frac{A}{\tan b}\right), \tag{7.5}$$

where A means water accumulation value and b is slope angle at each pixel.

Furthermore, a map of soil bonity units (BPEJ) was used to delineate main soil types within the field. All data were processed in ESRI ArcGIS 10.2 and Exelis ENVI 5.1.

7.3.2 Results and Discussion

Sampling design and differences in spectral signatures of spring barley as obtained from hyperspectral imaging are shown in Figure 7.9. The main differences were recorded in the near infrared and red parts of spectrum, which correspond to crop development.

A correlation analysis was calculated among chlorophyll-meter plant status, aboveground biomass, topographic parameters and selected vegetation indices (Table 7.1). The results showed statistically significant ($p < 0.05$) relationships between observed crop parameters (chlorophyll-meter readings, above-ground biomass) and vegetation indices, except between REIP and biomass, which was non-significant. Chlorophyll-meter readings were significantly correlated ($p < 0.05$) with all examined vegetation indices.

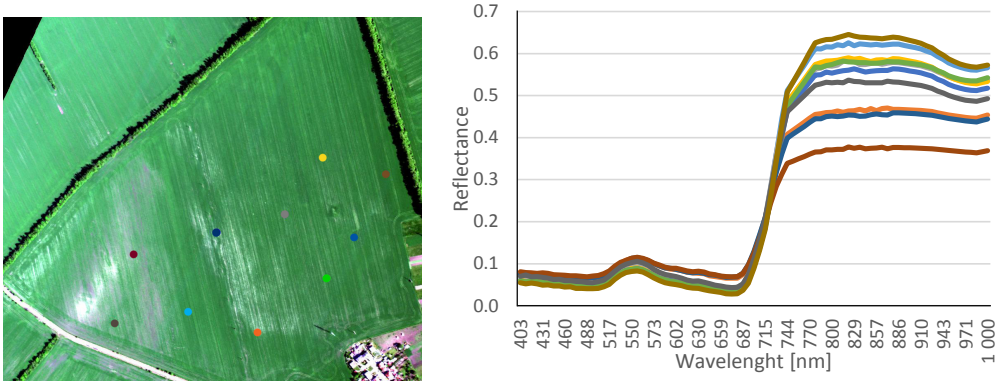

(a) **(b)**

Figure 7.9 (a) CASI image of the spring barely field with sampling points (i.e. colour dots) and (b) corresponding spectral signatures. Spectral curves are colour-coded by sampling point.

A statistically significant correlation ($p < 0.05$) between vegetation indices and field measurements from 10 sampling points enabled us to calculate two regression equations. The first one is between amount of dry biomass and NDVI

Table 7.1 Correlation analysis (Pearson's correlation coefficient) among crop parameters, topographic derivatives and vegetation indices for spring barley field (* indicate statistical significance at $\alpha = 0.05$)

	Elevation	TWI	NDVI	REIP	PRI	WBI
Chlorophyll-meter	-0.671*	0.859*	0.825*	0.637*	0.696*	0.859*
Biomass	-0.845*	0.713*	0.851*	0.311	0.731*	0.846*

Note: TWI – Topographic Wetness Index, NDVI – Normalized Difference Vegetation Index, REIP – Red Edge Inflection Point, PRI – Photochemical Reflectance Index, WBI – Water Band Index

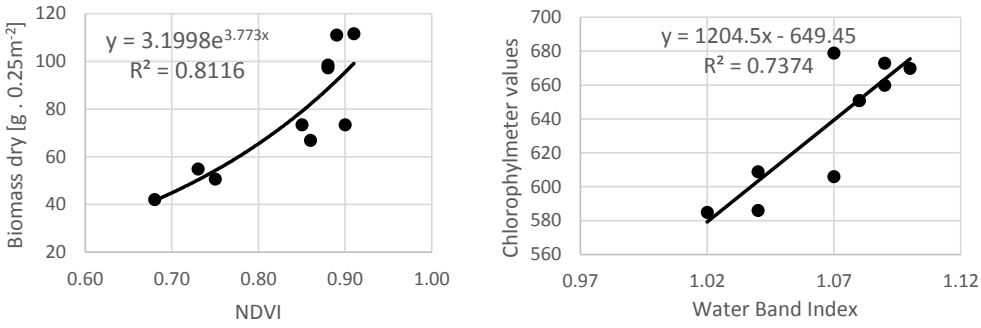

(a) **(b)**

Figure 7.10 Scatterplots of crop parameters and vegetation indices: (a) aboveground biomass vs. Normalized Difference Vegetation Index; (b) chlorophyll-meter values measured by N-Tester vs. Water Band Index

(Figure 7.10a), the second between a proxy of nitrogen content in biomass (i.e. chlorophyll-meter measurements) and WBI (Figure 7.10b). The first regression was used to map spatial distribution of dry biomass within the whole field (Figure 7.11e). The second regression was used to map spatial distribution of the crop nutrition status (Figure 7.11f).

The statistically significant correlation ($p < 0.05$) between WBI and TWI ($r^2 = 0.814$) documents the positive effect of field zones with higher soil moisture (higher TWI) on the crop development, represented by WBI. This effect is highlighted in semi-arid conditions or in dry weather condition, such as occurred during 2014 vegetation period at the observed locality. The influence of topography was also confirmed as significant for crop parameters (TWI in Table 7.1 and Figure 7.11c). This agrees with the results published by Godwin & Miller (2003), where topography is mentioned as one of the most obvious causes of variation found in field crops - it has an effect on soil parameters, which influence crop growth, but from practical point of view it is unchangeable and as a result can be used only to explain variation. An example of interpretation of

crop nutrition parameters by topographic characteristic and soil conditions is presented in a methodology developed by Rodriguez-Moreno et al. (2014). Also, the photochemical reflectance index PRI correlates significantly with dry biomass, as well as with chlorophyll-meter measurements (Table 7.1) and displays a pattern (Figure 7.11d) similar to those two parameters.

The goodness of fit between crop parameters and vegetation indices suggests that traditional extensive plant analysis can be replaced by an estimate in map form derived from airborne high spatial resolution HS data and a limited number of sampling points for calibration and verification.

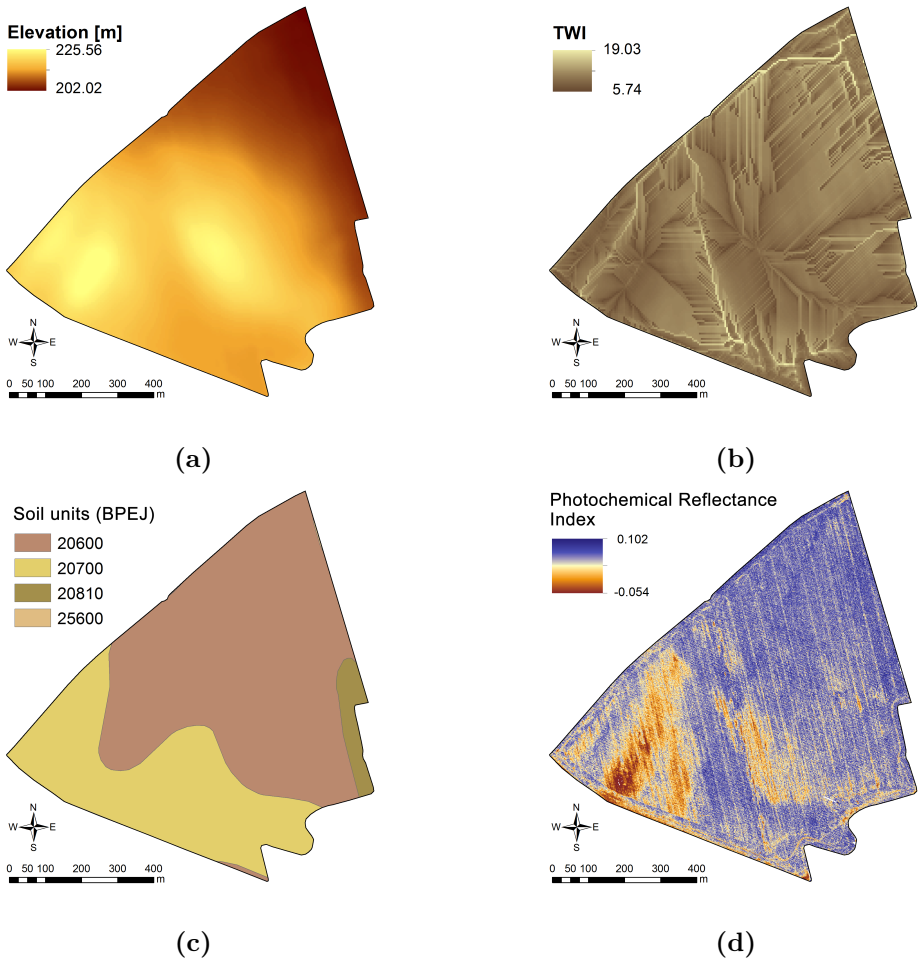

Figure 7.11 Maps of the studied barley field: (a) DEM from LiDAR data, (b) Topographic Wetness Index calculated from DEM, (c) delineation of soil units, (d) Photochemical Reflectance Index derived from hyperspectral data, (e) biomass estimated from Normalized Difference Vegetation Index (NDVI) and (f) estimation of chlorophyll-meter values (i.e. proxy of nitrogen content) based on the Water Band Index (WBI).

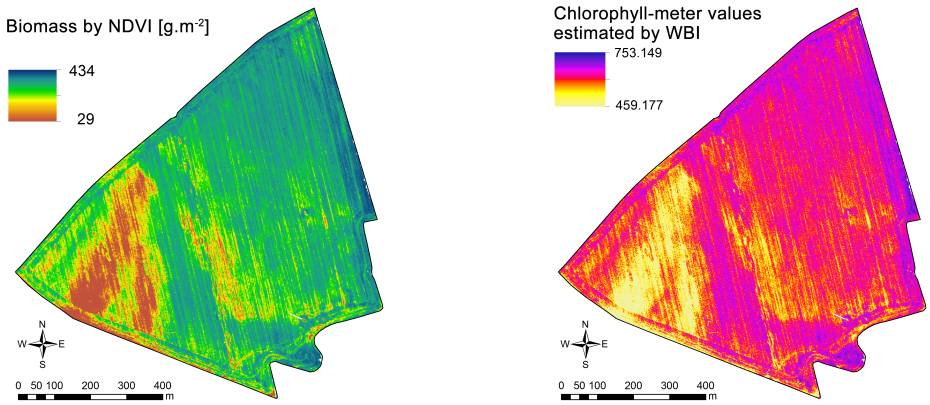

(e) (f)

Continued Figure 7.11

7.4 Conclusions

Hyperspectral imaging proved its ability to identify spatial variability of spring barley crop parameters, important for yield formation. Narrow band vegetation indices were used to estimate above-ground canopy biomass and chlorophyll-meter values for the whole field using 10 calibration points. Results in the form of maps could be used for site specific decision making in precision agriculture.

Acknowledgement:
The experimental work of this study was supported by research projects NAZV QI111A133 "Improvement of cereal variety potential realisation using temporal and spatial analysis of stand spectral characteristic" and MSMT LD14121 "The possibilities of using remote sensing to determine actual evapotranspiration of selected field crops."

Recommended Reading

Heege, H.J. 2013. *Precision in crop farming. Site Specific Concepts and Sensing Methods: Applications and Results.* Springer.

Oerke, E.-C., Gerhards, R., Menz, G. & Herbert, G. W. 2010. *Precision crop protection - the challenge and use of heterogeneity.* Springer, Dordrecht; Heidelberg.

Oliver, M., Bishop, T. & Marchant, B. 2013. *Precision Agriculture for Sustainability and Environmental Protection.* Taylor & Francis.

Pierce, F.J. & Nowak, P. 1999. Aspects of Precision Agriculture. *Advances in Agronomy* 67: 1–85.

8

CHLOROPHYLL MAPPING OF CONIFEROUS FORESTS

Lucie Homolová, Růžena Janoutová, Jan Hanuš, and Zbyněk Malenovský

8.1 Introduction

Life on the Earth is driven by photosynthesis. Photosynthetic activity of bacteria, algae and higher plants is controlled by photosynthetic pigments (chlorophylls, carotenoids and anthocyanins). The most important of these pigments are chlorophylls *a* and *b* (C_{ab}) as they directly control the amount of absorbed solar radiation available for the photosynthesis. Therefore low Cab concentration can limit plants' photosynthesis. Furthermore Cab is an indirect measure of plant nutrient status as much of leaf nitrogen is incorporated in chlorophyll macromolecules and a moderately strong correlation between N and C_{ab} exists across various species (Homolová et al. 2013). Plant chlorophyll content can be therefore considered as an indicator photosynthetic activity that reflects plant fitness, or conversely, an exposure to environmental stress factors. However, what makes C_{ab} so appealing from the perspective of remote sensing is the fact that C_{ab} molecules strongly absorb incoming solar radiation in the visible part of the EM spectra. This enables non-destructive quantification of plant C_{ab} content as indicator of photosynthetic activity using spectral data measured by means of proximal or remote sensing (Filella & Penuelas 1994; Datt 1998; Ustin et al. 2009).

Methods of quantitative estimation of plant C_{ab} using proximal and remote sensing data can be divided into two major groups: empirical and physical approaches (Liang 2004). Empirical approaches build on a simple regression relationship established between field measured C_{ab} and reflectance data. (Curran et al. 2001; Gitelson et al. 2003; Main et al. 2011). Physical approaches use radiative transfer models (RTM) to simulate plant-light interactions and thereby providing an explicit link between an output (top-of-canopy reflectance) and input (biochemical and structural) characteristics of the main scattering elements – leaves (Jacquemoud et al. 2009). Chlorophyll content is one of the main parameters of RTMs that can be effectively retrieved from RS data by inverting RTM (Baret & Buis 2008). In this chapter we will first introduce different approaches to estimation of leaf chlorophyll content and then illustrate them on a specific example of C_{ab} estimation of Norway spruce trees from very high resolution hyperspectral data (Malenovský et al. 2013).

8.2 RS-based Methods of Chlorophyll Estimation: A Mini-Review

Empirical approaches use statistical methods to establish a relationship between a limited set of field measurements and spectral data. Spectral data can be in the form of reflectance values or, more often, the reflectance data are in some way first transformed. The most common transformations for imaging spectroscopy data are calculating first or second derivatives, continuum removal or combining individual spectral bands into an index (le Maire et al. 2008; Schlerf et al. 2010). A large number of chlorophyll sensitive vegetation indices (VI) have been developed at the leaf, as well as the canopy level, from the reflectance data. Le Maire et al. (2004) and subsequently Main et al. (2011) evaluated the performance of about 70 chlorophyll sensitive VIs. Table 8.1 brings an overview of a few C_{ab}-sensitive VIs, which shows the large variability of VI types. Among many vegetation indices, those that are based on the shape of spectral continuum are particularly suitable for use with hyperspectral RS data as good estimator of C_{ab} content.

Another spectral indicator, which has been often associated with plant health status, and therefore logically to chlorophyll content, is the position of the red-edge inflection point (REIP) (Mutanga & Skidmore 2007). Hyperspectral data are most suitable for an accurate determination of the REIP. However, the role of REIP as a reliable estimator of plant chlorophyll content seems to be slightly controversial. On one hand Broge and Leblanc (2001) compared the performance of several broadband and narrowband VI (including three methods of REIP extraction) for C_{ab} estimation and concluded that RIEP indicators were surprisingly too sensitive to variations of canopy, background and atmospheric parameters. The REIP performed well only at high vegetation densities. Similarly, le Maire et

al. (2004) reported that RIEP indices were outperformed by traditional, simpler C_{ab}-sensitive VIs. On the other hand, Main et al. (2011) emphasized in their comparative study that REIPs were the most consistent and robust indices for C_{ab} estimation.

The greatest advantage of the empirical methods is that they are computationally fast, easy to establish and usually they are rather accurate at the local scale, where field measurements are available. A big disadvantage of these methods is that they often lack cause-effect relationships. Consequently, predictive statistical relationships are less robust as they are usually site, species and time specific (Colombo et al. 2003; Gökkaya et al. 2014).

Limitations of empirical retrieval methods can be partly overcome by using physically-based retrieval methods (Asner et al. 2003). Leaf-level RTM simulate leaf reflectance and transmittance properties. Canopy-level RTM effectively scale the leaf optical properties to the level of plant canopy (e.g. agricultural fields, forests). Among the leaf-level RTMs, the PROSPECT model (Jacquemoud & Baret 1990; Feret et al. 2008) is probably the most widely used model to simulate leaf optical properties. This is due to its simplicity and low number of input parameters (see Figure 8.2 and Section 8.3). Other leaf-level models such as LIBERTY (Dawson et al. 1998), LEAFMOD (Ganapol et al. 1998), SLOP (Maier et al. 1999) or DLM (Stuckens et al. 2009) are less often used. There has been a large number of canopy RTMs developed and they span from a relatively simple ones to complex, computationally demanding 3-D models. A good overview of currently used canopy RTMs is provided at the website of RAdiation transfer Model Intercomparison (RAMI, `http://rami-benchmark.jrc.ec.europa.eu`). Among the canopy-level RTMs, the SAIL model (Verhoef & Bach 2007; Jacquemoud et al. 2009) is the most frequently used model to scale-up leaf level optical properties to the canopy level. The main reason why the combination of PROSPECT-SAIL is so popular for interpretation of RS data is its simplicity in terms of input parameters (Jacquemoud et al. 2009) and its solid performance for structurally simple canopies (Widlowski et al. 2007). The SAIL model was primarily designed for homogenous canopies such as crops. However, it can be also applied to forests if the architecture is close to the assumption of homogenous foliage turbid media, i.e. the combination of dense and structurally uniform forests and larger pixel size of RS data (Sampson et al. 2003; Laurent et al. 2011). Other types of canopy RTM that attempt to reproduce the complex architecture of trees and forests are naturally more suitable to interpret RS data acquired over forested areas. Examples of 3D canopy RTMs are: DART (Gastellu-Etchegorry et al. 1996; Gastellu-Etchegorry et al. 2004), whose application is introduced later on, FLIGHT (North 1996), Raytran (Govaerts & Verstraete 1998) and many others (we recommend to visit the RAMI website).

Plant properties such as chlorophyll content can be retrieved from RS data by inverting a RTM (Baret & Buis 2008; Croft et al. 2013). Several direct and indirect inversion techniques have been developed and we will briefly introduce

them in the following sections.

The direct inversion methods use iterative numeric approaches to find values of the RTM input variables that minimize or maximize a cost function, while satisfying some constraints. Many optimization algorithms exits, but in RS studies one often encounter, for example the Quasi-Newton optimization (Combal et al. 2002) or the simplex method (Gascon et al. 2004). Direct inversions face two major limitations. First, an initial guess on values of input variables is needed, which might imply that a local, rather than general solution is found. Second, direct inversions can be computationally and time demanding as the RTM runs every iteration. Therefore their applicability is significantly restricted by the complexity of the employed RTM and by the size of RS images (Combal et al. 2002; Kimes et al. 2002).

The indirect inversion methods that use look-up tables (LUT) are more frequently applied on an operational basis compared to the direct inversions. In the LUT inversion, a RTM is run in forward mode and sets of pre-computed spectral signatures with corresponding input variables are stored in a database, called a look-up table. To find the solution to the inverse problem, the LUT is sorted according to a cost function allowing global search, i.e. avoiding a local solution. The cost function represents a statistical distance between measured (R_{MES}) and simulated (R_{LUT}) reflectance at wavelength λ and the classical example frequently applied in RS studies is the minimization of a root mean square error (*RMSE*):

$$RMSE = \sqrt{\frac{1}{n}\sum_{i=1}^{n}\left(R_{MES,\lambda} - R_{LUT,\lambda}\right)^2}. \tag{8.1}$$

However, in case of outliers and non-linear behaviour between canopy parameters and spectral reflectance, the key assumption for using *RMSE* is violated (Leonenko et al. 2013). Therefore Leonenko et al. (2013) and Rivera et al. (2013) suggested alternative cost functions coming from various fields of statistics and mathematics to provide more robust way to retrieve canopy parameters.

Certainly the greatest advantage of LUT inversion is that it is a simple and computationally efficient approach to retrieving vegetation parameters from RS data. Combal et al. (2002) compared three inversion approaches (iterative optimization using Quasi-Newton algorithm, LUT inversion and artificial neural networks) to retrieve four vegetation parameters (C_{ab}, leaf area index, fractional cover and fraction of absorbed photosynthetically active radiation) from the spectral data simulated by RTMs. The LUT inversion was evaluated as the fastest retrieval approach, especially when a priori information was used to restrict the size of the LUT. On the other hand, the LUT-based approach required a large amount of operations and computer memory because of the need to sort the LUTs. The main problem associated with the LUT inversion is that the given solution might not be the unique one as different sets of input parameters can correspond to almost similar spectra. This is often called the ill-posed inversion problem (Combal et al.

Table 8.1 Selection of chlorophyll-sensitive vegetation indices. For a complete overview see le Maire et al. (2004) and Main et al. (2011). Abbreviations: R_λ – reflectance at wavelength λ, D_λ – first derivative at wavelength λ, C – canopy scale, L – leaf scale.

1. Simple reflectance (or first derivative) ratios		
Index	**Scale**	**Reference**
R_{750}/R_{710}, D_{730}/D_{706}, D_{705}/D_{722}	C	(Zarco-Tejada et al. 2003; Zarco-Tejada et al. 2004)
$R_{695}/R_{420}, R_{695}/R_{760}$, $R_{710}/R_{760}, R_{695}/R_{670}$	L	(Carte, 1994)
$R_{750}/R_{550}, R_{750}/R_{700}$	L	(Gitelson & Merzlyak 1994)
2. Normalized difference		
Index	**Scale**	**Reference**
$(R_{925} - R_{710})/(R_{925} + R_{710})$	C	(le Maire et al. 2008)
$(R_{800} - R_{550})/(R_{800} + R_{550})$	C	(Gitelson et al. 1996)
$(R_{680} - R_{430})/(R_{680} + R_{430})$	L	(Penuelas et al. 1994)
3. Three-band indices		
Index	**Scale**	**Reference**
$R_{672}/(R_{550}R_{708})$, $(R_{850} - R_{710})/(R_{850} - R_{680})$	L	(Datt 1998; Datt 1999)
$(R_{734} - R_{747})/(R_{715} + 726)$	L	(Vogelmann et al. 1993)
MRCI: $(R_{754} - R_{708})/(R_{708} - R_{681})$	C	(Dash & Curran 2004)
mND_{705}: $(R_{750} - R_{705})/(R_{750} + R_{705} - 2R_{445})$ mSR_{705}: $(R_{750} - R_{445})/(R_{705} - R_{445})$	C	(Sims & Gamon 2002)
4. Combined indices		
Index	**Scale**	**Reference**
TCARI/OSAVI, TCARI: $3[(R_{700}–R_{670})– -0.2(R_{700}–R_{550})(R_{700}/R_{670})]$, OSAVI: $1.16(R_{800}–R_{670})/(R_{800}–R_{670} + 0.16)$	C	(Haboudane et al. 2002)
MCARI/OSAVI, MCARI: $[(R_{700}–R_{670})–0.2(R_{700}–R_{550})](R_{700}/R_{670})$	C	(Daughtry et al. 2000)

Continued Table 8.1

5. Indices based on spectral continuum, integral indices		
Index	**Scale**	**Reference**
$\int_{400}^{700} R_\lambda \, \mathrm{d}\lambda$	C	(Zarco-Tejada et al. 2001)
$\int_{680}^{780} D_\lambda \, \mathrm{d}\lambda$	L	(Filella & Penuelas 1994)
$\int_{705}^{750} \frac{R_\lambda}{R_{705}-1} \, \mathrm{d}\lambda$	L	(Gitelson & Merzlyak 1994)
NAOC643-795	C	(Delegido et al. 2010)
6. Red edge inflection point		
Index	**Scale**	**Reference**
REIP – four point interpolation: $700 + 40[(\frac{R_{670}+R_{780}}{2} - R_{700})/(R_{740} - R_{700})]$	L	(Guyot & Baret 1988)
REIP – inverted Gaussian fitting	L/C	(Miller et al. 1990)
REIP – Lagrangian technique	L	(Dawson & Curran 1998)
REIP – linear extrapolation	L	(Cho & Skidmore 2006)
7. Other indices		
Index	**Scale**	**Reference**
Curvature index: $R_{675}R_{690}/R_{683}^2$	C	(Zarco-Tejada et al. 2003)
Double difference: $(R_{749}–R_{720})–(R_{701}–R_{672})$	L	(le Maire et al. 2004)
Red edge symmetry: $(R_{718}–R_{675})/(R_{755}–R_{675})$	C	(Chang-Hua et al. 2010)
$(R750–R_{800}/R_{695}–R_{740})–1$	L	(Gitelson et al. 2003)

2002). This can be alleviated by regularization of the inverse problem, i.e. considering only those solutions that are in the proximity of the true value. The most often implemented regularization step is to consider a priori knowledge that is available about the unknown input RTM parameters (Combal et al. 2002) or to use neighbourhood radiometric information of the pixel (Atzberger 2004; Houborg et al. 2009; Laurent et al. 2013). Some additional steps to stabilize a solution are to determine an optimal size of the LUT (Weiss et al. 2000), to average a number of top solutions (Weiss et al. 2000; Darvishzadeh et al. 2008; Rivera et al. 2013) and to select only important, uncorrelated spectral bands (Schlerf & Atzberger 2006; Darvishzadeh et al. 2008).

Another group of indirect inversion algorithms used in RS are so-called machine learning algorithms. They are applied on a LUT database simulated by a RTM to generate an adaptive, nonparametric relationship between an input (i.e. reflectance) and output (i.e. vegetation parameters). In remote sensing, ma-

chine learning algorithms are mainly employed for image classification and pattern recognition (Mas & Flores 2008). However, they also show strong potential for estimation of continuous vegetation parameters (Schlerf & Atzberger 2006; Verrelst et al. 2012b). Among the machine learning algorithms, artificial neural networks (ANN) are probably the most often used (Atzberger 2004). ANN can handle potential noise in spectral data quite well, but it can be difficult and time consuming to train a proper ANN architecture. Other machine learning algorithms that are considerably less used in RS estimation of vegetation parameters are e.g., support vector machines, kernel ridge regression and Gaussian processes (Verrelst et al. 2012b). According to recent work of Verrelst et al. (2012a; 2012b), Gaussian processes seem to be a very promising method as it outperformed other modern machine learning algorithms.

8.3 Chlorophyll Content Retrieval of Norway Spruce

The objective of this chapter is to demonstrate applications of some methods that were introduced in Section 8.2 to estimate chlorophyll content in Norway spruce forest. In this case study, which is based on Malenovský et al. (2013), we employ radiative transfer modelling, artificial neural networks and vegetation indices to assess C_{ab} content of Norway spruce trees. The flowchart (Figure 8.1) provides an overview of the methodology, which is further introduced in the following sections.

8.3.1 Experimental Test Site and Ground Measurements

An immature Norway spruce plantation that was selected for this case study is part of the CzechGlobe's permanent experimental research station Bílý Kříž in the Moravian-Silesian Beskydy mountains (18.54°E, 49.50°N, 936 m above sea level). This spruce stand can be characterised as follows: an average canopy height about 12 m, an average stem diameter about 13 cm and leaf area index about 8. In 2004 an extensive field and airborne campaign took a place, during which we sampled spectral, biochemical and structural properties of spruce needles. In total 10 sample trees were investigated in detail. We sampled one branch at the top (sunlit) and at the bottom (shaded) of a tree. From each branch shoots of three most recent age-classes were collected resulting in 6 needle samples per tree. Each needle sample was analysed for C_{ab} content and specific leaf area in a laboratory according to standard protocols verified by Lhotáková et al. (2007). An average value of C_{ab} content per tree was then calculated as a weighted average of 6 samples according to biomass distribution inside spruce crowns.

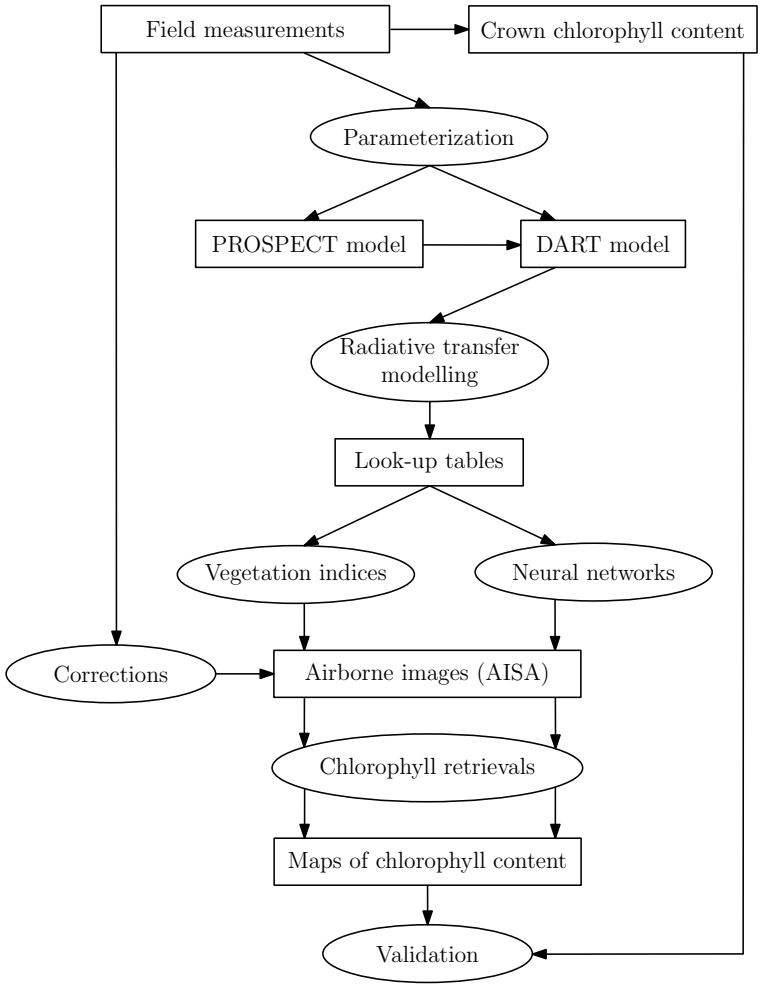

Figure 8.1 The conceptual work flow of the C_{ab} retrieval from hyperspectral data by means of radiative transfer modelling.

8.3.2 Remote Sensing Data

Airborne hyperspectral data were acquired by a pushbroom VNIR airborne imaging spectroradiometer AISA Eagle (Specim Ltd., Finalnd) on September 18$^{\text{th}}$ 2004. In total 64 spectral bands between 400 and 980 nm were acquired with an average spectral sampling distance of 10 nm. The image spatial resolution was 0.4 m. The AISA images were radiometrically corrected using factory calibration coefficients in the CaliGeo software (AISA processing toolbox provided by Specim Ltd., Finland). Further, the atmospheric corrections and nadir image normalization were carried out using ground-measured spectra of five fabricated Lambertian calibration panels in the Atcor-4 software (Richter & Schlapfer 2002). The pixel size of 0.4 m allowed us to detect individual spruce crowns and even to differen-

tiate the sunlit and the shaded crown parts by applying a supervised maximum likelihood classification. For the retrieval of C_{ab} content we used only sunlit crown parts as they provide higher signal-to-noise ratio than shaded pixels.

8.3.3 Radiative Transfer Modelling

The radiative transfer models used in this study were a leaf level model PROSPECT (Jacquemoud & Baret, 1990) coupled with a canopy model DART (Gastellu-Etchegorry et al., 1996). The PROSPECT model was adjusted to spruce needles by Malenovský et al. (2006). Figure 8.2 shows a simple graphical representation of both models. For a better illustration of how complex RT modelling can be in terms of input parameters, in Table 8.2 we bring an overview of the PROSPECT-DART input parameters used in this study. A detailed description of how individual DART input parameters were obtained is provided in Malenovský et al. (2008; 2013). RTM was used to build up a database of simulated canopy reflectance values (look-up tables).

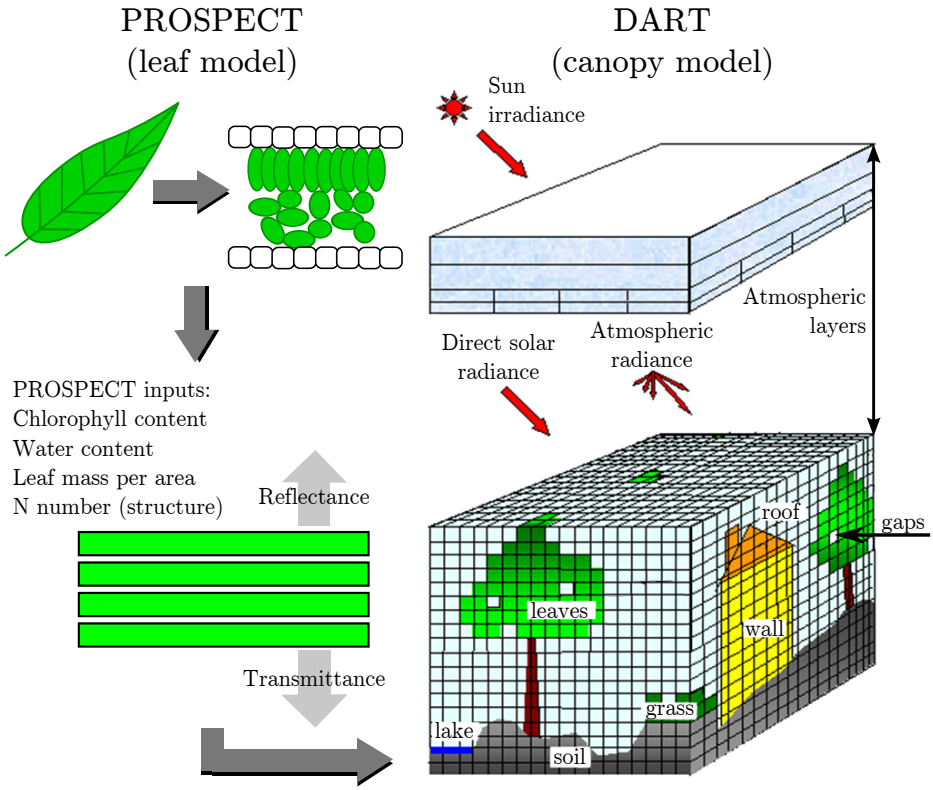

Figure 8.2 Simplified representation of the PROSPECT and the DART radiative transfer models used in this study. (Source: The scheme of DART was modified from CESBIO (2013) and the scheme of PROSPECT was designed by authors)

8.3.4 Retrieval Methods

We used the database of simulated top-of-canopy reflectance values (LUT database) to estimate spruce crown C_{ab} from the AISA image data. We implemented three types of C_{ab} retrievals: i) band ratio vegetation indices, ii) vegetation index based on the spectral continuum, and iii) a machine learning algorithm – artificial neural networks. In the first two cases, the PROSPECT-DART simulated LUTs were used to establish a statistical relationship between the C_{ab} and the vegetation indices. In the last case, the look-up tables were used to train the neural network.

Band ratio vegetation indices

In this case study, we used three, previously developed vegetation indices: 1) Normalized Difference optical index ($ND_{925\&710}$), which was recommended by le Maire et al. (2008) as the best index for C_{ab} retrieval of broadleaf canopies from the Hyperion data; 2) Simple reflectance Ratio index ($SR_{750/710}$), which was used by Zarco-Tejada et al. (2004) to estimate C_{ab} of Jack pine canopies; 3) a combination of two indices TCARI and OSAVI, which was originally designed by Haboudane et al. (2002) for crop canopies (see their equations in Table 8.1).

Vegetation index based on spectral continuum

This index was developed by Malenovský et al. (2013) and it benefits from the shape of spectral continuum that hyperspectral data offer. Its design is schematically explained in Figure 8.3. The index design employs a continuum removal (CR) transformation (Kokaly & Clark 1999) that enhances the specific absorption feature of C_{ab} in the red part of the electromagnetic spectra. For the continuum removal transformation it is crucial to include the most sensitive C_{ab} absorption wavelengths and to avoid at the same time the negative interferences of the canopy structure. Therefore the CR interval starts in the middle of the red chlorophyll absorption feature at the wavelength of 650 nm and ends in the middle of the red edge region at the wavelength of 720 nm. The index was then calculated as the Area Under Curve of CR reflectance between 650 and 720 nm ($AUC_{650–720}$) normalized by the CR Band Depth at 670 nm (CBD_{670}).

Artificial neural networks

Artificial neural networks belong to the group of machine learning algorithms that can be employed for a look-up table based inversion of RTM (Combal et al. 2002). A suitable ANN architecture was evaluated in the MATLAB neural network toolbox (The MathWorks, Inc., USA) and established to be a two-layer feed-forward back-propagation ANN. The first (input) layer was composed of six neurons corresponding to the six simulated AISA spectral bands (listed in Table 8.2) and associated with a tan-sigmoidal transfer function. A linear transfer function was assigned to the second (output) layer that contained only one neuron producing

the C_{ab} estimate. The most crucial step of the ANN approach is the proper training of the selected network. One fourth of the PROSPECT-DART simulated LUT entries were randomly selected to train the network. The high-speed processing Levenberg–Marquardt optimization algorithm was applied for the network training. The performance of the training was evaluated using another fourth of the LUT entries. The best performing ANN (i.e. not over-fitted and with the lowest possible root mean square error and highest R^2) was employed to retrieve C_{ab} from the AISA sunlit crown pixels.

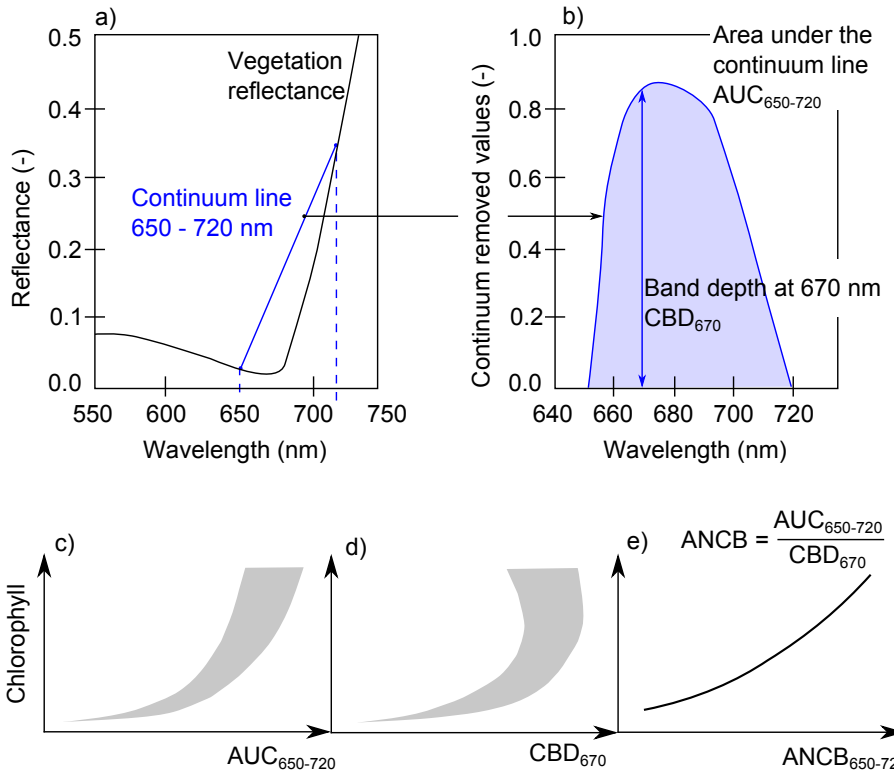

Figure 8.3 Figures (a) and (b) show the concept of the continuum removal transformation. The remaining plots only schematically depict the sensitivity of area under curve $AUC_{650-720}$ (c), continuum band depth at 670 nm (CBD_{670}), and $ANCB_{650-720}$ index (e) towards varying chlorophyll values.

8.3.5 Results and Discussion

Figure 8.3c indicates that the area integrated under the simulated continuum removed curves between 650 and 720 nm ($AUC_{650-720}$) is exponentially related to C_{ab}. Due to the early saturation these exponential relationships cannot be exploited to estimate C_{ab} values above 40 µg cm^{-2}. The grey area in Figure 8.3c shows that multiple AUC values correspond to one C_{ab}. This is due to variations

in canopy cover and leaf area index. Figure 8.3d indicates the band depth of the strongest chlorophyll absorption at 670 nm (CBD_{670}), is also insensitive to C_{ab}. But the ratio of both, $AUC_{650-720}/CBD_{670}$, exhibits a strong nearly linear relation to C_{ab} (Figure 8.3e). This formulation gives basis of the new optical index called 'Area under continuum-removed curve Normalized to the Chlorophyll absorption Band depth between 650 and 720 nm' ($ANCB_{650-720}$). The index can estimate C_{ab} of sunlit Norway spruce crowns independently from the LAI variation. The relationship between C_{ab} and $ANCB_{650-720}$ is follows:

$$\ln(C_{ab}) = 7.40 - \frac{7984.01}{(ANCB_{650-720})^2}, \qquad \left(R^2 = 0.99, p < 0.001\right). \tag{8.2}$$

$ANCB_{650-720}$ compared to the other three vegetation indices exhibits fairly superior performance (Figure 8.4). All three relationships are statistically significant, but only $ANCB_{650-720}$ and TCARI/OSAVI seem not to be influenced by leaf area index and canopy cover (note the narrow dispersion of points for each C_{ab} level). A map of chlorophyll content as obtained from the $ANCB_{650-720}$ index (eq. 8.2) is showed in Figure 8.5.

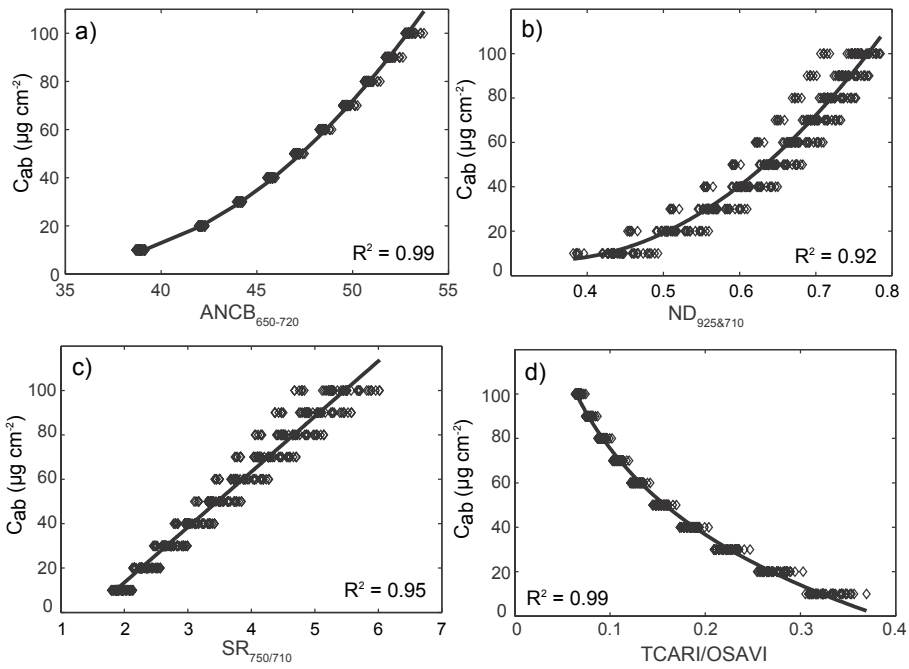

Figure 8.4 Relation between C_{ab} and vegetation indices (a) newly designed $ANCB_{650-720}$, (b) normalized difference $ND_{925\&710}$, (c) simple ration $SR_{750/710}$ and (d) TCARI/OSAVI.

Table 8.2 Input parameters of PROSPECT-DART radiative transfer model to simulate spruce stand top-of-canopy reflectance.

	DART input parameters (F/V)[a]	**Symbol**	**Units**	**Values**
Sun position	Zenith angle (F)	θ_s	[°]	47.8
	Azimuth angle (F)	Φ_s	[°]	183.4
Forest scene parameters	Voxel size (F)		[m]	0.2
	Horizontal dimensions (F)	x, y	[m]	6.0, 6.0
	Slope (F)		[°]	13.5
	Number of tree crowns (F)			4–7
	Canopy closure (V)	CC	[%]	75–95 (in steps of 10)
	Leaf area index (V)	LAI	[m^2m^{-2}]	4.0–9.0 (in steps of 1.0)
Average tree parameters mean (std. dev.)	Trunk height below crown (F)		[m]	0.38 (0.13)
	Trunk height within crown (F)		[m]	8.08 (0.76)
	Trunk diameter below crown (F)		[m]	0.17 (0.02)
	Trunk diameter within crown (F)		[relat]	0.41 (0.03)
	Total tree height (F)		[m]	10.45 (0.88)
	Crown type (F)			Conical
	Crown height (F)		[m]	10.08 (0.76)
	Crown bottom radius (F)		[m]	1.60 (0.24)
	Number of crown levels (F)			10
	Average leaf angle (F)	ALA	[°]	37 (7)
	Mean Twig area index (F)	TAI	[m^2m^{-2}]	0.082 (0.017)
	Average twig angle (F)	ATA	[°]	35
	Percentage of full leaf cells in crown (F)		[%]	48
PROSPECT inputs for leaf optical prop.	Chlorophyll content (V)	C_{ab}	[µg·cm^{-2}]	10–100 (in steps of 10)
	Water content (F)	C_w	[cm]	0.036–0.048
	Dry matter content (F)	C_m	[g·cm^{-2}]	0.012–0.023
	N parameter (F)	N	[-]	2
Simulated spectral bands in DART	Central wavelengths of visible (VIS) Bands (F)	λ_{VIS}	[nm]	652.1, 661.4, 670.7, 680.1, 689.4
	Central wavelengths of near infrared (NIR) bands (F)	λ_{NIR}	[nm]	698.7, 708.1, 717.4

[a] F/V denotes whether the given input parameter was kept fixed (F) or varied (V) for the purpose of the generation look-up tables.

The ANN was trained on continuum-removed reflectance values. Therefore, ANN produced very similar range of values and spatial patterns as $ANCB_{650-720}$ (Figure 8.5). The subtraction of the ANN C_{ab} map from the $ANCB_{650-720}$ C_{ab} map revealed an absolute mean difference of only 1.8 µg cm^{-2}. The mean differences between ANN and the other three indices are much larger, i.e. -9.01 µg cm^{-2} for $ND_{925\&710}$, -4.30 µg cm^{-2} for $SR_{750/710}$, and 13.29 µg cm^{-2} for TCARI/OSAVI. The comparison of retrieved C_{ab} values with ground-measured C_{ab} of spruce crowns is shown in Figure 8.6. The highest R^2 of 0.72 with the lowest *RMSE* (2.27 µg cm^{-2}) were obtained for $ANCB_{650-720}$ (results for ANN not shown as they are almost identical to $ANCB_{650-720}$). The second most accurate retrieval was performed with $SR_{750/710}$, followed by $ND_{925\&710}$, both underestimating C_{ab} by 4.16 and 9.07 µg cm^{-2}, respectively. The least accurate method is the TCARI/-OSAVI estimation (R^2 = 0.41 with an *RMSE* equal to 12.30 µg cm^{-2}), despite its fair performance on simulated LUT database (cf. Figure 8.4d). A visual investigation of the C_{ab} map revealed that the systematic overestimation of the TCARI/OSAVI retrieval is caused by pixels with lower reflectance located at the edge of spruce crowns. These pixels are more likely affected by the background reflectance or they might contain a higher proportion of shadows than the one simulated by the RT models.

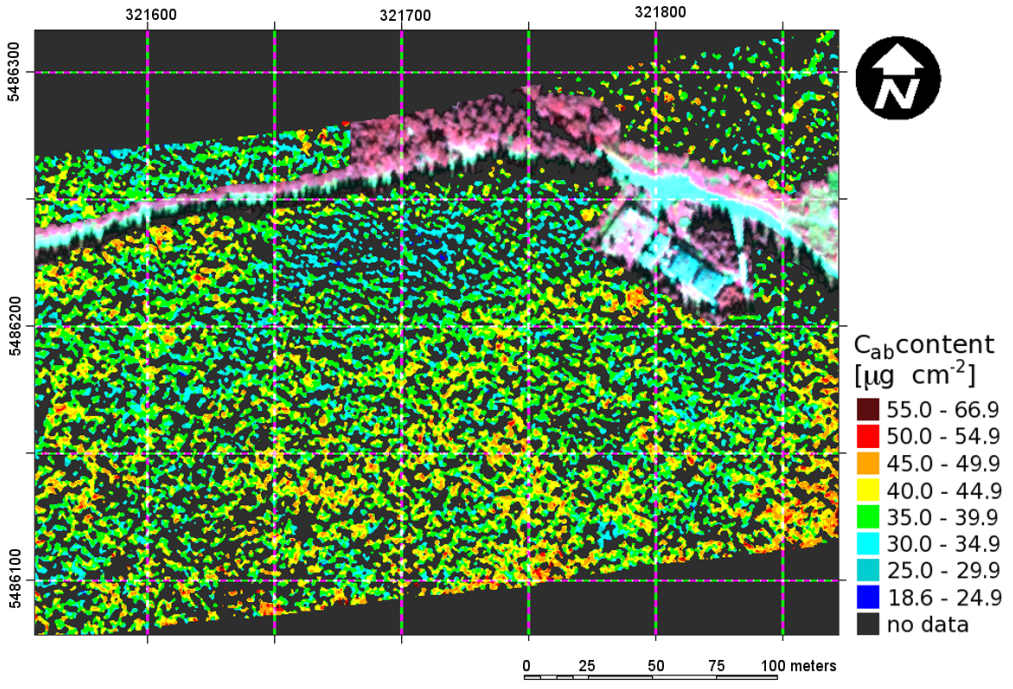

Figure 8.5 Map of chlorophyll content of Norway spruce forest as estimated by the $ANCB_{650-720}$ index.

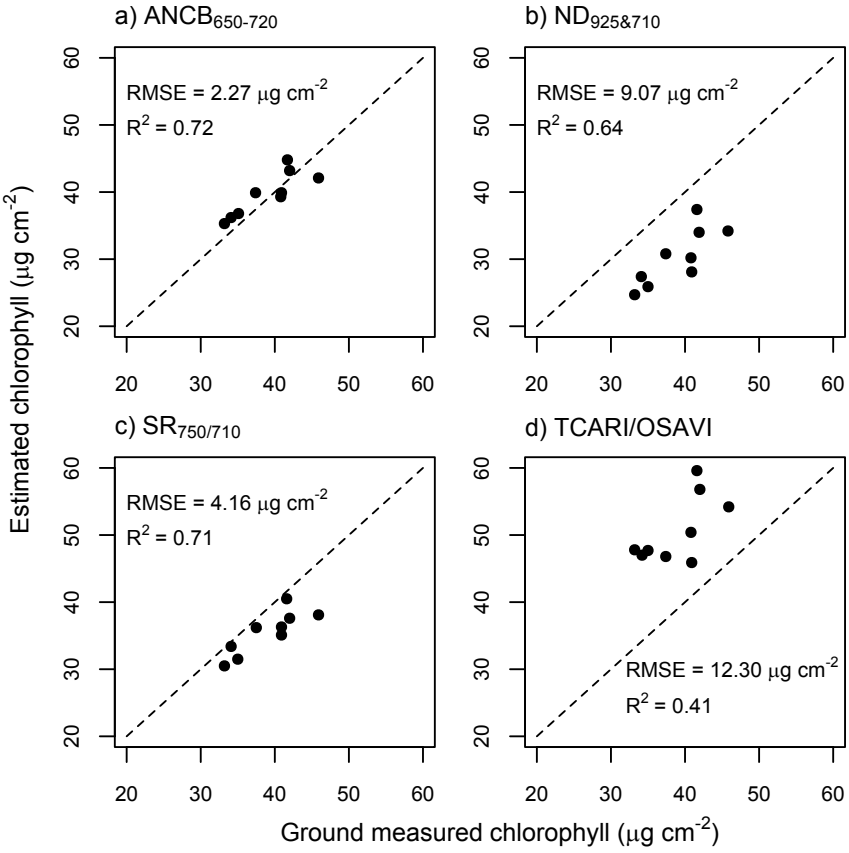

Figure 8.6 Comparison of chlorophyll estimated values by means of vegetation indices (a) $ANCB_{650-720}$, (b) $ND_{925\&710}$, (c) $SR_{750/710}$ and (d) TCARI/OSAVI and ground measured chlorophyll of individual Norway spruce trees.

8.4 Conclusions

In this chapter we introduced a variety of RS-based approaches available for estimation of plant properties. More specifically, we described a case study where radiative transfer modelling in combination with vegetation indices and artificial neural networks were employed to estimate chlorophyll content of Norway spruce canopies. Results show that approaches using the shape of spectral signatures (a vegetation index and artificial neural networks applied on continuum removed spectra) are successful in retrieval of chlorophyll content of spruce crowns. Both approaches outperformed traditional ratio-based vegetation indices. The neural networks approach was slightly more accurate that the $ANCB_{650-720}$ index, but more laborious and computationally intensive. The $ANCB_{650-720}$ index is there-

fore fast and robust estimator, if applied to airborne images of sub-meter spatial resolution, which allows elimination of spectrally impure or noisy (e.g. deeply shadowed) canopy pixels.

Recommended Reading

Jacquemoud, S., Verhoef, W., Baret, F., Bacour, C., Zarco-Tejada, P.J., Asner, G.P., Francois, C. & Ustin, S.L. 2009. PROSPECT + SAIL models: A review of use for vegetation characterization. *Remote Sensing of Environment* 113: S56—S66.

Liang, S. 2004. *Quantitative remote sensing of land surfaces.* John Wiley & Sons, Inc., Hoboken, New Jersey.

Main, R., Cho, M.A., Mathieu, R., O'Kennedy, M.M., Ramoelo, A. & Koch, S. 2011. An investigation into robust spectral indices for leaf chlorophyll estimation. *ISPRS Journal of Photogrammetry and Remote Sensing* 66: 751-–761.

Malenovský, Z., Homolová, L., Zurita-Milla, R., Lukeš, P., Kaplan, V., Hanuš, J., Gastellu-Etchegorry, J.-P. & Schaepman, M.E. 2013. Retrieval of spruce leaf chlorophyll content from airborne image data using continuum removal and radiative transfer. *Remote Sensing of Environment* 131: 85-–102.

Ustin, S.L., Gitelson, A.A., Jacquemoud, S., Schaepman, M., Asner, G.P., Gamon, J.A. & Zarco-Tejada, P. 2009. Retrieval of foliar information about plant pigment systems from high resolution spectroscopy. *Remote Sensing of Environment* 113: S67—S77.

9

APPLICATIONS OF AIRBORNE LASER SCANNING IN FORESTRY

Jan Novotný, Tomáš Mikita, Martin Machala, and Lucie Homolová

9.1 Introduction

Rapid technical advances currently make airborne laser scanning (ALS) one of the most promising technologies for the retrieval of detailed information about forests on different scales, i.e., from individual trees to the plot/stand level to inventories at the national level. ALS data has proven superior qualities compared to other types of optical data used for forest inventory (Hyyppä & Hyyppä 1999).

ALS data for forestry applications can be of two types. Discrete multiple return systems provide data of individual backscattered returns and their intensities from different canopy layers. Full waveform systems record the continuous backscattered signal from a return (Heinzel & Koch 2011; Wulder et al. 2012). ALS data provide a solid basis for a wide range of applications and analysis in forestry. The most common product of ALS is the digital terrain model (DTM) (see Section 4.5 for details). A DTM helps forest managers and engineers to design and optimize the forest road network and to plan a harvesting system or

protection against erosion. Furthermore, ALS data alone, or in combination with multispectral or hyperspectral images, can serve as underlying spatial information for classification of forest types (Machala & Zejdová 2014) and possibly of individual tree species (Yu et al. 2014). The most interesting and promising way that ALS data can support forest management is to derive forest inventory parameters. It is possible to estimate parameters at the stand level such as stand borders, mean canopy height, canopy density, as well as to detect individual trees and to derive their height, crown dimensions and diameter breast height (*DBH*) (Heurich et al. 2003; Holopainen & Hyyppä 2003; Maltamo 2004). ALS therefore is an efficient substitute for time-consuming and spatially constrained field work in obtaining essential forest inventory parameters. ALS-derived forest parameters can be further used to estimate forest stand biomass, timber volume etc.

There are two approaches to deriving forest parameters from the ALS data: area-based (ABA) and individual tree detection-based (ITD) approaches. In the case of ABA, percentiles and other distribution-related features of the laser backscattered signal are used to predict stand parameters, such as mean tree height, mean diameter and basal area. The prediction, however, is based on empirical statistical techniques that ultimately require accurate field data on selected forest parameters to establish a predictive relationship (Yu et al. 2010). These methods are used for commercial forest inventories in Scandinavian countries (Holopainen et al. 2014). The ITD approach is based on detection of individual tree crowns, their heights and crown dimensions from a raster canopy height model (CHM, which is calculated as the difference between digital surface and terrain models). All other tree and forest stand parameters are estimated by means of statistical models based on species-specific allometric equations that are most frequently using tree height and tree density as inputs.

Forest inventory based on ITD is less often put into practice, because data with high point densities are required in order to accurately detect and delineate individual trees under various forest conditions (Vastaranta et al. 2011). Densities between 5 and 10 points per m^2 are required for ITD compared to less than 1 point per m^2 in case of the ABA approach. A great advantage of ITD over ABA is that it provides true stem distribution enabling better predictions of timber assortments (Holopainen et al. 2010). Another advantage is that the amount of expensive fieldwork is significantly reduced compared to that which is necessary when applying the ABA approach. It is easier to establish allometric equations per species from individual tree measurements than for entire mixed stand. ITD still relies on some field data in order to optimize the predictive models for specific habitat conditions. Recent comparison of ABA and ITD approaches for boreal forests indicated that both approaches achieve similar accuracy in estimation of forest stand parameters (mean height, *DBH* and volume). The ITD approach showed slightly better results, but economic costs of data acquisition and processing were higher than of the ABA approach (Yu et al. 2010).

ALS is commonly used for forest inventories in Scandinavian countries (Carson

et al. 2004; Næsset 2004), but the current situation in the Czech Republic is very different. A complete inventory of forest stands in the Czech Republic is a part of the Forest Management Plan (Forest act 289/1995 No.). Forest management plans are created for a period of 10 years by means of field surveys and qualified estimates of tree species, tree heights, *DBH* and stock of wood. Neither ABA nor ITD forest inventory approaches using ALS data have been widely tested in the Czech Republic. The main restriction is that suitable allometric models for timber and biomass volume estimation are missing. Compared to the Scandinavian countries, forests in the Czech Republic are of richer species composition and this implies that the allometric models have to be tailored to multiple species. However, we are strongly convinced that the ALS technology will sooner or later find its way into current forestry practices. It has great potential to refine the estimation of forest inventory parameters and support management planning leading to sustainable forest management.

In the following sections we will introduce in greater depth the use of ALS data for: i) classification of forest types, ii) detection and delineation of individual trees, and iii) estimation of forest inventory parameters (tree height, *DBH* and stand volume). It is important to mention that all the examples below are based on different ALS data from different forest sites in the Czech Republic. Rather than give details on data acquisition and processing, we will introduce each topic from a more general point of view. Therefore, more technical details on classification of forest types can be found in Machala & Zejdová (2014), on tree detection and delineation in Novotný (2014), and on estimation of forest inventory parameters in the Czech Republic in Mikita et al. (2013b).

9.2 Forest Segmentation and Classification

In general, the classification of RS data into information classes (types of land cover) is a very broad task. Typically, optical multispectral or hyperspectral image data are used, but recently also ALS data are employed for classification. In forestry, the target classes are types of forest – broadleaf vs. coniferous, age composition classes, or tree species in the most detail.

Classification methods can be divided into two broad groups, pixel-based and object-based methods. Pixel-based methods work with raw or radiometric values of individual pixels grouping them into appropriate classes based on their similarity. Object-based methods first segment an image into objects (groups of adjacent pixels with similar values). The segmented objects then have ordinary properties, such as mean value of pixels within an object and its standard deviation and geometric properties, such as shape, size, length etc. All the object properties can be then effectively used for object classification into thematic classes. For forestry application, object based image analysis (OBIA) can offer a more sophisticated

alternative compared to the pixel-based approaches by treating individual crowns as objects.

Although the OBIA technique has been primarily developed for classification of raster image data, e.g. classification of broadleaf vs. coniferous trees by Alberti et al. (2013), managed vs. natural forests by Dickinson et al. (2014), it can be extended by including ALS data. In the case where only ALS data are available the OBIA classification technique can still be applied on rasterized ALS products such as DTM, DSM and CHM (Machala & Zejdová 2014). In such a case, it is better not to rely on a CHM alone (Figure 9.1a), but to include other thematic layers that can be directly calculated from a DTM or CHM. Examples of additional data layers to support the OBIA classification process are: a slope model (Figure 9.1b), a curvature model, and a range model (difference between largest and smallest values of adjacent cells). All these layers can be used as inputs for classification similar to how bands of multispectral imagery are used. Various software packages capable of OBIA are available on the market today.

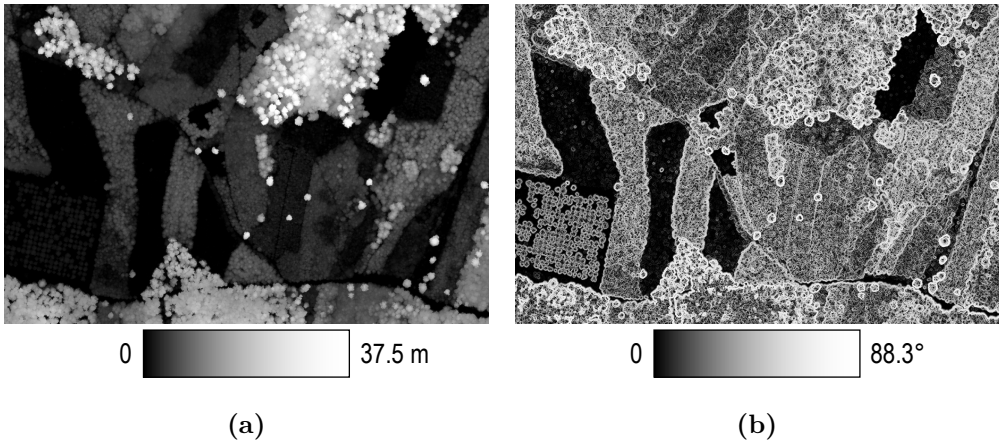

Figure 9.1 (a) Canopy height model derived from ALS data acquired with Leica ALS50-II (2.5 pt/m^2) for mixed forest study area and (b) corresponding slope model with spatial resolution of 0.5 m.

Specialized OBIA modules are included in major software packages such as Idrisi, ENVI, ERDAS, and eCognition. A typical workflow in eCognition begins with a multi-resolution segmentation process followed by classification. During the segmentation, user-defined weights are assigned to each input layer and the amount and the shape of gained segments is controlled by setting scale, shape and compactness parameters. The result of this process is an image segmented into objects (Figure 9.2a). Only then are all information classes that should be distinguished declared and an operator defines training areas (i.e. representative image objects) for each information class. The Nearest Neighbour classifier is employed to group objects into pre-defined classes. Figure 9.2a illustrates the result of such an OBIA classification of mixed broadleaf forest.

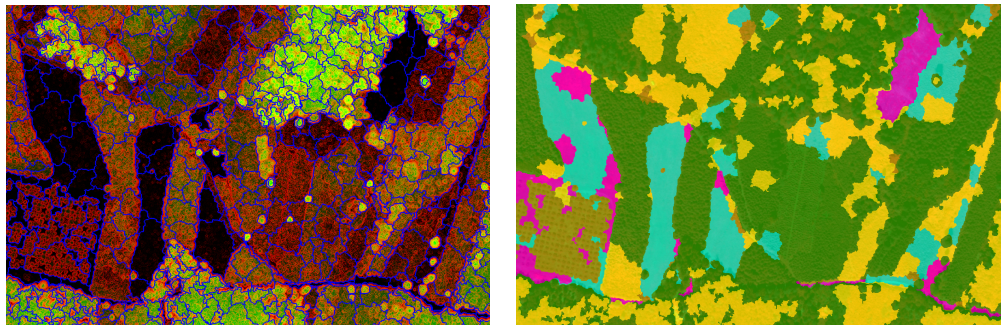

(a) **(b)**

Figure 9.2 (a) Image objects (blue borderlines) created by the multiresolution segmentation process in eCognition Developer software and (b) final result of corresponding object-based classification. The classes are: broadleaf forest – yellow, coniferous forest – green, plantation – brown, young stands – cyan and bare terrain – pink. The images show the same area as at Figure 9.1.

An indispensable part of each classification workflow is an accuracy assessment. This is usually done by comparison of the classification results with ground truth data, which can be either collected during the field survey or based on other data source, e.g. orthophoto imagery. The result of this comparison is calculated in the form of an error matrix showing how many pixels were classified incorrectly and what is the overall accuracy. Considering the results shown in Figure 9.2, the overall accuracy of the object-based classification purely based on ALS data was calculated to be equal to 82 % and the Kappa Index of Agreement (KIA) equal to 70 %. For the sake of completeness, the classification accuracy of the same study area when using the combination of spectrozonal aerial imagery (red, green, blue and NIR bands) with CHM derived from ALS data reached nearly 90 % and KIA to 85 % (Machala & Zejdová 2014). Those results show that OBIA technique can deliver highly accurate classification of forest types when imagery and ALS data are combined, as well as when ALS data are used on their own.

9.3 Individual Tree Detection and Delineation

Attempts on tree crown detection and delineation from remotely sensed data started in 1990's as the first high resolution airborne optical imagery became available. The current trend, however, is to employ ALS data or to combine both, laser scanning and optical images. In Table 9.1 we bring a brief overview of studies that use different kinds of RS data for crown detection and delineation.

A canopy height model (CHM=DSM–DTM) is the key input for tree detection and delineation. Figure 9.3a shows a CHM of a beech dominated forest. The spatial resolution of a CHM, as well as of the underlying digital terrain and

surface models, are key factors influencing the accuracy of tree detection. The spatial resolution should be in correspondence with the average size of crowns, as well as with the point density of ALS data. According to our experience, a tree becomes detectable if its diameter exceeds four pixels and the point density of underlying ALS data is higher than $3\,\mathrm{pt/m^2}$ (optimum is somewhere between 5 and $10\,\mathrm{pt/m^2}$). A CHM usually contains salt-and-pepper noise and therefore it is highly recommended to apply a low-pass filtering (median or Gaussian filters) to smooth the CHM. Furthermore, larger non-forested areas should be masked out as they might hamper the detection and delineation algorithms. The method

Table 9.1 Overview of published studies reporting tree crown detection and delineation using different types of airborne remote sensing data.

Type of remote sensing data	**Example studies (dominant tree species and country of the study)**
Optical RS (multispectral or hyperspectral images)	Culvenor (2002) (Eucalyptus species; Australia) Pitkänen (2001) (Scots pine, birch species, European larch and Norway spruce; Finland) (Erikson 2003) (Scots pine, birch species, Norway spruce and European aspen; Sweden) Pouliot et al. (2005) (White spruce; Canada) Bunting & Lucas (2006) (Brigalow and Eucalyptus species; Australia) Hirschmugl et al. (2007) (Scots pine, Norway spruce and oak; Austria)
Airborne laser scanning	Brandtberg et al. (2003) (Oak species, red maple and yellow poplar; USA) Chen et al. (2006) (Blue oak; USA) Koch et al. (2006) (English oak, hornbeam, Douglas fir, European beech, silver fir, etc.; Germany) Gupta et al. (2010) (Scots pine, oak , hornbeam, European beech, silver birch and Norway spruce; Germany) Korpela et al. (2010) (Scots pine, Norway spruce and birch species; Finland)
Combination of airborne laser scanning and optical RS data	Leckie et al. (2003) (Douglas fir; Canada) Breidenbach et al. (2010) (Scots pine, Norway spruce, trembling aspen and birch species; Norway)

for detecting positions of individual trees from CHM is rather straightforward. Tree tops correspond to local maxima in the CHM (or minima if an inverse CHM is used). Local maxima are found using a sliding window. The size and shape of the sliding window fundamentally influence the detection results. Considering

the natural shape of trees, we would recommend using a circular shape for the sliding window rather than rectangular. The size of the sliding window should be set adaptively based on the expected size of analysed crowns. It is necessary to search for the tops of higher trees with a larger sliding window and for the tops of smaller trees with a smaller one. The expected size of crowns can be modelled via an allometric equation for the actual tree species or can be estimated via mathematical image processing techniques (e.g., search for semivariance sills or slope breaks on several transects laid through the inspected CHM).

Once the centres of individual trees are found, we can move to the next step of crown delineation. We introduce here three delineation algorithms: inverse watershed, valley-flowing and seed region growing. A brief review of other delineation algorithms is provided in Bunting & Lucas (2006). First, the inverse watershed algorithm is adopted from hydrological applications of drainage basins. In this algorithm, the CHM is inverted, local maxima become minima and the structure is then "flooded" from these minima points. Borders of individual crowns are drawn on the watershed ridges (Figure 9.4a). Second, the valley-following approach is based on the similarities between a forest canopy and a mountainous area. Tree tops are found as local maxima. The boundaries of crowns are derived from a network of local minima. A complex rule-based algorithm is used in order to connect local minima into a network and remove dead ends (Gougeon 1995). The third approach is called seeded region growing (Novotný 2014). Tree tops are identified as local maxima again. From these pixels crowns are "grown" by adding neighbourhood pixels until certain condition is met. The algorithm stops when the height drops under a pre-set minimal limit and/or when two neighbour crowns touch. It is necessary to grow all the trees simultaneously if we want to reach the correct encounter of the neighbouring crowns. Figure 9.4 illustrates the differences of crown delineation as obtained from the inverse watershed and region seed growing algorithms. The performance of the seed region growing algorithm for tree detection and delineation of deciduous and coniferous forests was evaluated by Novotný (2014). The ALS system Riegl Q680i was used to collect data with varying point density (10–50 $\mathrm{pt/m^2}$) at three forest sites. As Table 9.2 indicates, despite the varying point density, the seed region growing algorithm shows very consistent results across the forest types with different species composition, height and age.

9.4 Calculation of Individual Tree Parameters from ALS

The method for calculating tree parameters from ALS using the individual tree detection-based approach is based primarily on correct detection of individual tree crowns and calculation of corresponding tree heights. Species-specific allometric equations are then used to calculate other tree parameters, such as *DBH*,

Table 9.2 Evaluation of the seeded region growing algorithm for crown detection and delineation at three forest types of different age and height. Total number of detected trees, and accuracy of tree detection and delineation is reported.

Site description and forest characterization			**ALS data**	**Detection and delineation results**		
Site	**Forest type**	**Canopy height [m]**	**Point density [pt/m^2]**	**No. of detected trees**	**Tree detection**	**Tree delineation**
Bílý Kříž (Moravian-Sillesian Mts)	Immature Norway spruce	11.9 ± 3.8	50	5305	85.1 %	76.8 %
Rájec (Czech-Moravian Highlands)	Mature Norway spruce	27.6 ± 4.1	10	4538	87.5 %	79.0 %
Štítná (Bílé Karpaty)	Mature Europan beech	26.9 ± 2.6	50	6204	83.5 %	80.8 %

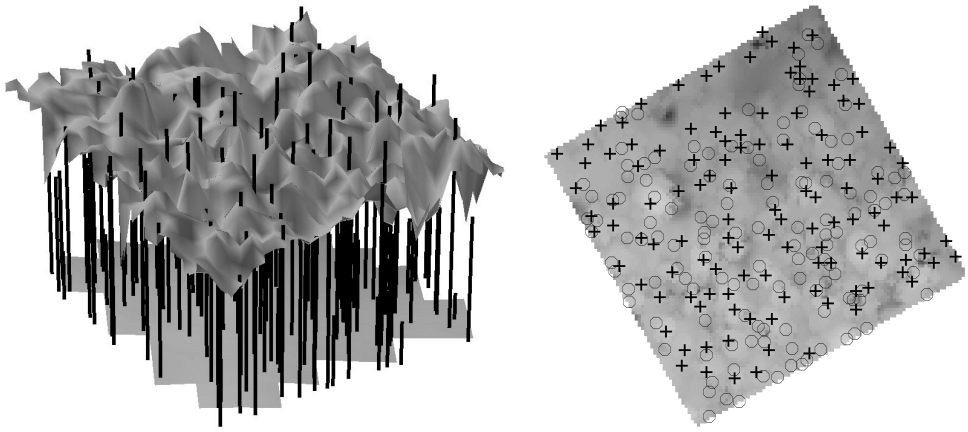

(a) **(b)**

Figure 9.3 (a) Example of an interpolated canopy height model. (b) Comparison of trees detected from ALS data (+) with field geodetic measurements of their location (∘). The results are based on ALS acquired over beech dominated forests with the scanning point density of $5\,\mathrm{pt/m^2}$.

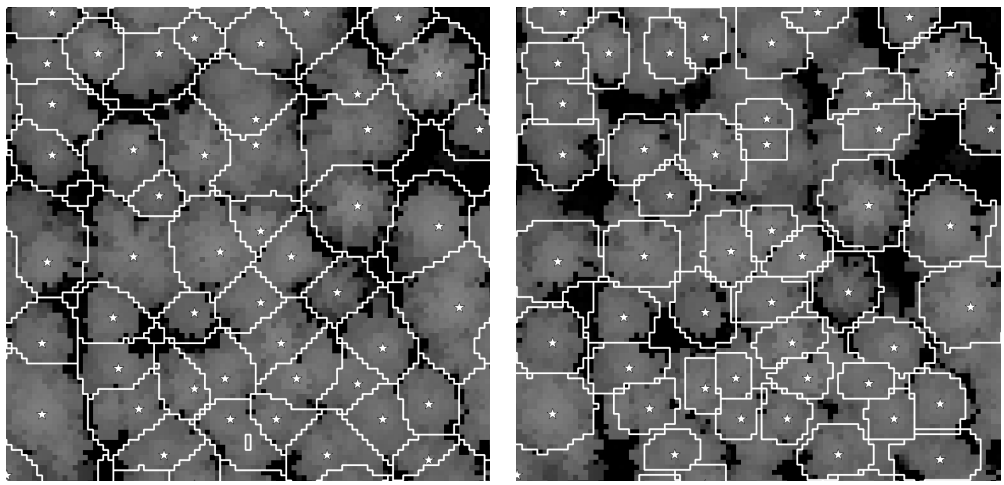

(a) **(b)**

Figure 9.4 Crown delineation results as obtained from (a) inversed watershed and (b) seeded region growing algorithms. The results are based on ALS acquired over a mature beech forest in Štítná nad Vláří. The scanning point density was $50\,\mathrm{pt/m^2}$ and the spatial resolution of CHM was 0.5 m.

timber volume. These parameters can be subsequently integrated and up-scaled to the level of entire stands. The estimation accuracy of individual tree parameters is almost solely dependent on the accuracy of tree detection and tree height

estimation. Absolute accuracy of tree height estimates from ALS is around 1 m (van Leeuwen & Nieuwenhuis 2010), but many studies agree that tree heights are almost always underestimated by 1 to 5 m (Hyyppä & Inkinen 1999; Kwak et al. 2007; Mikita et al. 2013b). The main factors influencing the accuracy of tree detection and tree height estimation is the ground point density of ALS data. In the case of lower point densities, the probability that a tree top will be omitted increases. Inaccuracies may also occur when sublevel trees are not detected (Yu et al. 2010; Mikita et al. 2013b). Other tree parameters, such as *DBH* can be estimated achieving accuracies between 0.025 and 0.065 m (Korpela et al. 2010; Holopainen et al. 2010). Forest stand parameters, such as standing volume reaches accuracies from 5 % up to 35 % (Maltamo et al. 2009; Vauhkonen et al. 2010; Tonolli et al. 2011).

Calculation of individual tree parameters (tree height, *DBH* and timber volume) is demonstrated here with a case study of Mikita et al. (2013b). For the purpose of the study, ALS data with density of $4\,\mathrm{pt/m^2}$ were acquired with the Leica ALS50-II system over a European beech dominated forest located at the Training Forest Enterprise Křtiny (Mendelu). Simultaneously, geodetic and forest inventory surveying was performed to measure exact location, height and *DBH* of about 600 trees, which was used for evaluation purposes.

For tree detection, the inverse watershed segmentation was used and tree heights were directly calculated from the corresponding CHM. The positional accuracy of the exact tree location was about 0.6 m and the overall accuracy of the tree height estimation was about 5.5 m. The low accuracy of height estimation can be attributed to the fact that small trees in the sublevel could not be well detected from the ALS data. However, when only tall trees were considered ($h > 25\,\mathrm{m}$) the accuracy increased to about 1.4 m. The cell size of the CHM raster and the selection of an interpolation method used to create DTM and DSM also had considerable impact on the accuracy of tree detection and height estimation.

Other tree parameters, diameter at breast height (*DBH*) and timber volume (V), were calculated based on existing allometric equations that were adjusted using the actual field measurements. Both equations use tree height (h) as an input parameter. For *DBH* calculation the adjusted Michajlov's function (Michajlov 1943) was used:

$$DBH = \frac{12.29}{3.78 - \ln(h - 1.3)}. \tag{9.1}$$

Calculation of timber volume of individual trees (V) was based on a model developed in Slovakia (Petráš & Pajtík 1991). The model is established on relationships between allometric parameters obtained by destructive techniques (cut tree, measurements of trunk, branches) and those obtained by nonedestructive field measurements, such as tree height, *DBH*). Due to the dominance of beech

in the research plots, coefficients derived for beech were used as follows:

$$V = \left[0.54 - \frac{0.31}{h} + \frac{44.33}{h^2} - \frac{235.97}{DBH} - \frac{0.001DBH}{h} - 1.86 \cdot 10^{-5}\frac{h^2}{DBH} - \right.$$
$$\left. -8.8 \cdot 10^{-7} hDBH^2 - 6.0 \cdot 10^{-9} hDBH^3\right] \frac{\pi hDBH}{40000}. \quad (9.2)$$

A comparison with the forest management plan indicated that the estimated volumes fall into the range reported in the plan.

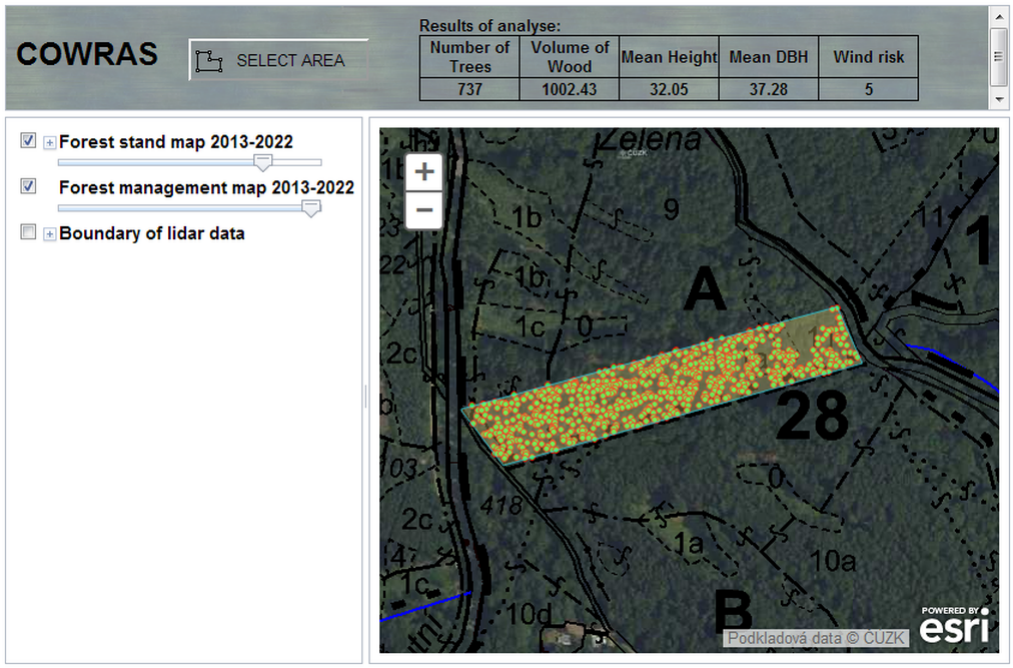

Figure 9.5 Graphical user interface of the COWRAS tool (with tree parameters and wind risk assessment in the table).

9.5 Outlook

The potential of ALS data for forestry applications is wide, but its usage for current forestry practice in the Czech Republic is still very limited. As demonstrated in this chapter, several attempts to analyse ALS data in the context of forestry application have been already made. These are mainly research activities that are limited to small areas and to answer specific research questions. One of the limitations explaining why ALS data are not that widely used is that data processing and subsequent analysis require special software, basic knowledge

of processing techniques and GIS software. All this puts great demands on potential users in public administration (environmental agencies, forest managers, etc.). There are several user-friendly software packages supporting ALS data analysis such as freeware Fusion (`http://forsys.cfr.washington.edu/fusion/fusionlatest.html`) or commercial ENVI Lidar (`http://www.exelisvis.com/docs/using_envi_lidar_Home.html`). There exist also freeware web-based geoprocessing tools for ALS data such as COWRAS (Clearcut Optimization and Wind Risk Assessment; `http://arcgis.mendelu.cz/topex/`). Its user interface is shown at Figure 9.5. The tool has been developed for optimization of clearcuts (their location, shape, size, and orientation) with subsequent wind risk assessment. It primarily works with ALS data previously processed to the form of DSM, DEM and CHM. COWRAS identifies individual trees, and calculates their height, DBH and volume (as described in 9.4). Information about each tree in a clearcut can be exported and summarized in a table. By removing all trees from a user-defined clearcut, evaluation of wind risk damage based on topographic exposure of uncovered forest stand edges is predicted. The web-based implementation of such a geoprocessing tool allows the use of sophisticated ALS processing methods and GIS analysis by ordinary users.

Acknowledgement:
Parts of this chapter were supported by the research project of the Internal Grant Agency of the Faculty of Forestry and Wood Technology, Mendel University in Brno No. 68/2013 "Development of custom solution of remote sensing by unmanned aircraft vehicles and their practical usage in forestry."

Recommended Reading

Maltamo, M., Næsset, E. & Vauhkonen, J. 2014. *Forestry Applications of Airborne Laser Scanning.* Springer

van Leeuwen, M. & Nieuwenhuis, M. 2010. Retrieval of forest structural parameters using LiDAR remote sensing. *European Journal of Forest Research* 129: 749–770.

10

SURFACE TEMPERATURE REGIME OF THE LANDSCAPE

Petra Hesslerová and Jan Pokorný

10.1 Introduction

Temperature is a state variable characterizing whether or not a body will be in thermal contact with another body in thermal equilibrium (i.e. whether it will take the heat, hand it over or a heat exchange will not be accomplished). If there is no heat exchange between bodies, they have the same temperature. For the purpose of this chapter it is necessary to distinguish between surface radiation (brightness) temperature and air temperature measured in a standard way in meteorology (see Chapter 3 and (Norman & Becker 1995). On a sunny day a radiation temperature of bare surface can be as much as 20°C higher than the air temperature.

Dissipation, in the classical thermodynamics called energy loss, is irreversible transformation to a different kind of energy, especially heat. Classical thermodynamics describes principles in which thermal energy is converted into movement at the price of irreversible losses – dissipation. Carnot described the efficiency of a machine and distinguished "useful" exchange energy and "dissipated" energy that is irreversibly lost (entropy). A Carnot engine, operating as a closed system, is attempting to reach thermodynamic equilibrium – when temperatures are equal, the machine stops. The machine can be set in motion by the delivery of

additional external energy.

The Earth's biosphere is receiving energy from the Sun; the outer layers of the atmosphere receive during a year 1321–1412 $\mathrm{W\,m^{-2}}$. Living systems have evolved as open systems and due to the input of solar energy, are far from thermodynamic equilibrium. They shape, improve. Unlike the Carnot machine, living systems connect into more organized structures. Prigogine in the 60's of the last century created new non-linear (non-equilibrium) thermodynamics to describe the self-organization of open systems far from thermodynamic equilibrium. He introduced the concept of "dissipative structure" to emphasize the difference (paradox) between a closed system (machine) and living system. In classical thermodynamics, the dissipation of heat is always associated with energy waste and degradation of the system. In open systems, especially in living systems, dissipation becomes a source of order, a process of increasing organization. We may consider as a pioneering work in this field a series of public lectures delivered by physicist Erwin Schrödinger called "What is Life?" (see Schrödinger 1944).

Living systems, ecosystems (dissipative structures) compensate for temperature differences, generally "life abhors gradients" (Schneider & Sagan 2005). Temperature differences that arise due to the uneven level of irradiation are a precondition for the life development. The ability of ecosystems to balance temperatures is shown e.g. by differences in temperature between day and night in the desert and in the forests of the same geographical zone. The relatively low surface temperature and temperature equalization between places and between day and night (in space and time) are manifestations of the active role of ecosystems. (Ripl 1995) proposed a conceptual Energy-Transport-Reaction (ETR) model, which includes three basic processes of dissipation of solar energy (temperature equalization) that are mediated by water:

- Evaporation and condensation
- Dissolution and precipitation of salts
- Decomposition of water into oxygen and hydrogen, and reversing formation of water molecules (photosynthesis and respiration)

What processes influence the temperature of ecosystems?

Solar energy comes at a certain point of the Earth's surface in daily pulses (night and day), seasonal pulses and long term periodic variations from occur as a result of changes in the shape of Earth's orbit around the Sun and from changing of solar activity. In the short term clouds play crucial role – on a clear day Earth's surface receives up to 1000 $\mathrm{W\,m^{-2}}$, on a cloudy day the amount of solar radiation decreases to under 100 $\mathrm{W\,m^{-2}}$, i.e. a tenth. Solar radiation that comes to the surface is partially reflected, and partially absorbed, some of that energy heating the Earth's surface and some of it being absorbed by organisms and used in biological processes. From a heated surface air that flows up (sensible heat); part of the

solar energy is used for evaporation of water (latent heat of evapotranspiration) and a part goes into the ground (soil heat flux). A relatively small amount of solar energy is bound by the process of photosynthesis into biomass. Table 10.1. shows the ranges of values of the main processes of energy flows in ecosystems. The intensity of these processes varies during the season and during the day by the input of solar energy. Processes are interconnected and they tend to reduce gradients, thus reducing the temperature differences. Evapotranspiration is the most effective process of converting solar energy, reaching values of hundreds of $\mathrm{W\,m^{-2}}$. The uptake of one molecule of carbon dioxide results in one molecule of oxygen being excluded, along with a few hundred molecules of water as water vapour.

The temperature in the landscape is the result of reflection of solar radiation, radiation exchange between the sky and the other bodies and massive flows of energy in the biosphere mediated by water. The distribution of temperature is an indicator of the effectiveness of the use of solar energy.

Table 10.1 Energy transformations in ecosystems take the following values:

Reflection of shortwave radiation	5–25 % from the incident radiation
Primary production (photosynthesis)	Units of $\mathrm{W\,m^{-2}}$
Evapotranspiration	Hundreds of $\mathrm{W\,m^{-2}}$
Decomposition of organic matter in the soil at a negative balance of primary production	Units to tens of $\mathrm{W\,m^{-2}}$
Heating of growth biomass	Units to tens of $\mathrm{W\,m^{-2}}$
Solar radiation on the outer atmosphere during the year	1321–1412 $\mathrm{W\,m^{-2}}$
Radiative forcing since the year 1750	1–3 $\mathrm{W\,m^{-2}}$ (0.2 $\mathrm{W\,m^{-2}}$) is expected in next 10 years

10.2 Aims

This study, which is based on Hesslerová et al. (2013), demonstrates a combined method of airship scanning of surface temperature (T_s) and ground measuring of air temperature (T_a) in a varied agricultural landscape, to show the daily dynamics of T_s and T_a at localities with different land cover. The aims of the study were:

1. to record and quantify the differences in spatial and temporal dynamics of T_s during a hot summer day within a cultural landscape of high land cover variability (forest – alder stand – wet meadow – harvested meadow – bare field – asphalt – water),

2. to compare daily dynamics of the surface temperature T_s of the studied localities with air temperature T_a and demonstrate the differences between these temperatures,
3. to discuss and point out how landscape planners and engineers may affect local climate by dealing with water and vegetation.

10.3 Methods

10.3.1 Site Description

Seven localities with different land cover types were chosen, southeast of the village of Domanín (about 5 km southeast of the town of Třeboň, Czech Republic):

- Locality 1 (HM) — harvested mesic meadow covered with drying out grass of about 10 cm length. Dominant species were *Alopecurus pratensis* L. and *Arrhenatherum elatius* (L.) J. Presl & C. Presl.
- Locality 2 (WM) — wet meadow with high underground water level, dominant species: *Phalaris arundinacea* L. and *Carex* sp., cover height of approx. 1 m.
- Locality 3 (AS) – alder stand, floodplain community of *Alnus glutinosa* L. and *Prunus avium* L., shrubs and smaller trees of up to 3 meters high.
- Locality 4 (F) – mixed forest represented mainly by pine trees (*Pinus sylvestris* L.) and oaks (*Quercus robur* L.); estimated age 60 years, average cover height 10–15 meters.
- Locality 5 (SV) – bare field (loamy-clay soil), less than 50 % of the area covered by sparse grass vegetation.
- Locality 6 (W) – open surface water. Shallow pond with maximum depth of 1.5 m and intensive fish farming.
- Locality 7 (A) – asphalt surface of a road.

10.3.2 Remote Sensing Measurement of Surface Temperature T_s

The measurements were carried out on July 9th 2010. The nine-meter long airship (operated by AirshipClub.com) was equipped with an advanced navigation and control systems that allowed it to fly in an automatic mode along a precisely defined route navigated by GPS (for details see (Jirka et al. 2011)). It flew about 250 m above the ground, the swath being about 200 m. In order to monitor the surface temperature throughout the light part of a sunny day, the area was scanned by both thermal and visible cameras simultaneously, sixteen times (at 04:50, 05:30, 06:00, 07:10, 08:10, 09:10, 10:40, 13:15, 14:00, 15:10, 16:10, 17:10,

18:10, 18:40, 19:10, 20:10 GMT+1). The thermographic camera IR FPA ThermaCAM TM PM695 (FLIR System Sweden) measures and images infrared radiation emitted from an object in the spectral range from 7.5 µm to 13 µm with the spatial resolution of 320 × 240 pixels (pixel size of 30 cm) and thermal sensitivity of 0.08°C at 30°C. The radiation detected by the camera is influenced by objects' emissivity, reflected radiation from the surroundings and absorption and emission of radiation from the atmosphere. The precise temperature measurement is subject to accurate compensation of different sources of radiation. The calibration requires the following parameters: the object's emissivity, reflected surrounding temperature, distance between the object and camera, relative humidity and atmospheric temperature (see details in Section 3.3.2). The calibration parameters were obtained from the screens situated within the area of interest; the emissivity parameters as standard table values.

10.3.3 Meteorological Data

Air temperature (T_a) was measured at 2 meters above the soil surface at 10-minutes intervals (T_a, °C, $T + R_h$ probes, accuracy ±0.1°C) on five of the seven studied localities. Individual T_a measurements at different localities exhibited subtle differences (due to different land cover types) and therefore only one reference T_a value for the whole study area was calculated as their average.

The locality "harvested meadow" was equipped also with CNR1 net radiometer (Kipp & Zonen) for radiation balance analysis of solar and far infrared radiation (in $\mathrm{W\,m^{-2}}$). Incident (R_{sdown}) and reflected global solar radiation (R_{sup}) in shortwave region was measured by CM3 pyranometer (Kipp & Zonen, spectral range from 0.31–2.8 µm), far infrared radiation (5–50 µm) was measured by two CG3 pyrgeometers, one for measuring radiation coming from the sky (R_{ldown}), the other for measuring radiation coming from the soil surface (R_{lup}). All these data were used to set-up and to calibrate the thermal camera.

10.3.4 Data Processing

To record the daily dynamics (i.e. from 4:50–20:10 GMT+1) of surface temperature from thermal images, we focused on the following variables:

- Mean daily surface temperature (T_{savrg}) — mean surface temperature of a locality measured in 16 scans from 04:50 to 20:10.
- Mean surface temperature of a locality in time t (T_{st}).
- Mean minimum surface temperature, mean maximum surface temperature (T_{smin}, T_{smax}) – temperature extremes recorded during the time of measurement (4:50–20:10 GMT+1).
- Surface temperature difference (D_s) – the difference between T_{smax} and T_{smin}.

- Surface temperature fluctuation (expressed by values of standard deviation) – shows the variability of temperature at a locality at a certain time (surface temperature heterogeneity of a locality SD_{st}) or throughout the day (mean daily variability SD_{sd}).

The variables were calculated from the thermal images and converted into ASCII data format. To reduce the huge data files while maintaining all characteristics of the original data, we applied a random data selection. A random permutation of the elements of 'x' (or '1:x') was used. As a representative sample, 1000 values (pixels) for every locality and time were chosen. Box plots were used in the figure depicting the course of the surface temperature.

10.4 Results and Discussion

Surface temperature and its daily dynamics in the studied localities with different types of land cover were found to be significantly distinctive during a hot sunny day. The surface temperature values for individual localities are listed in Table 10.2. The most distinct differences were found between the localities with dry or sparse vegetation and those with fully functional vegetation and sufficient water supply. Temperature characteristics of the ecosystems with no or non-functional vegetation largely resembled the asphalt surface (T_{smax} 47.6°C, D_s 31.4°C), whereas those with dense vegetation were influenced by the presence and phase transition of water (water surface: T_{smax} 29°C and D_s only 9°C due to high heat capacity of water). The localities covered with dense bushy or tree vegetation showed relatively well balanced daily temperature dynamics (Figure 10.1) with low temperature extremes and slow temperature morning increase or afternoon decrease. The impact of vegetation and water presence on the ecosystem temperature dynamics was nicely demonstrated on the wet meadow locality which showed much more balanced temperature compared to the nearby harvested meadow covered with dry vegetation.

The importance of water for the ecosystem temperature balance is connected not only with the physical characteristics of liquid water but also with high latent heat of its liquid-gas transition. This process via evapotranspiration provides the living systems with highly effective thermoregulative mechanism (2.5 MJ kg^{-1} at 20°C are spent during evaporation and released during condensation). The cooling and warming effects of water liquid-gas transition can be multiplied within the vegetation, especially within high forest stands, thanks to higher temperature and structural variability (Makarieva et al. 2006; Hesslerová & Pokorný 2010a,b; Kedziora 2010; Eiseltová et al. 2012; Hesslerová et al. 2013).

The T_a measured in the 5 meteorological screens within the studied area did not differ much during the insolated part of the day (Table 10.2). During the midday, the differences between the screens was around 1°C or even less; the maximum difference was measured before sunset (19:10 and 20:10), when it reached 6°C (be-

Table 10.2 Mean surface temperature (T_s) characteristics of the studied localities measured by thermal camera from 4:50 to 20:10 in sixteen scanning times. (Abbreviations: T_{smin} – temperature minimum, T_{smax} – temperature maximum, D_s – temperature difference, T_{savrg} – mean temperature, SD_{sd} – surface temperature variability throughout the day).

Locality[a]	T_{smin}	T_{smax}	D_s	T_{savrg}	SD_{sd}
HM	9.3	44.2	34.8	28.0	10.98
WM	10.0	31.9	21.9	22.6	6.78
AS	10.1	28.9	18.8	21.7	5.95
F	12.0	29.0	17.0	22.8	5.77
SV	13.2	37.2	24.0	26.4	7.70
W	20.4	29.3	8.9	25.6	3.41
A	16.1	47.6	31.4	33.0	10.19

[a] HM – harvested meadow, WM – wet meadow, AS – alder stand, F – forest, SV – sparse vegetation, W – water, A – asphalt

tween asphalt and wet meadow screens) and 4.6°C (asphalt and field). Whereas T_a was relatively similar at different places in the studied area (Table 10.3), the maximum difference of T_s between the different studied land covers reached almost 20°C in the early afternoon (Table 10.3 and Figure 10.2). The substantial difference in $T_s - T_a$ at localities with different land cover, both in values and the characteristics of the daily courses imply that it is essential to consider the relations between T_s and T_a site specifically.

In general, high irradiation causes surface temperature to be higher than air temperature 2 m above the surface (Pal Arya 2001; Katsiabani et al. 2009; Gallo et al. 2011). However $T_s - T_a$ strongly varies according to the land cover type and can reach even negative values. Also, the daily courses of these variables differ. Whereas the surface temperature peaks around 12:30 simultaneously with the maximum intensity of irradiance, the air temperature peaks later in the afternoon between 16:00 and 17:00 (Table 10.3 and Figure 10.2). Large differences in $T_s - T_a$ of almost 15°C at the maximum of incoming irradiance (Table 10.3) were found at the localities with sparse or dry vegetation. At the same time T_s of the localities covered with dense vegetation well supplied with water (wet meadow, alder stand and forest) was even slightly lower than T_a. Even though the comparison of T_s and T_a could have been influenced by the different height of the compared stands (air temperature was measured 2 m above the meadow whereas the forest was 10–15 m tall), the temperature differences were large enough to express the influence of functional vegetation on T_s increase. Moreover, taking into account the fact that T_a commonly changes in adiabatic lapse rate of 0.6 to 1°C/100 m of elevation, the differences of T_a above a meadow and an adjacent forest stand should not be large.

Table 10.3 Comparison of mean air (T_a) and surface (T_s) temperatures at seven studied localities during the day of measurement. SD_a – standard deviation of air temperature.

			Mean surface temperature (T_s) of the localities (by remote sensing) [°C]						
Time	**Mean T_a at 2 m [°C]**	SD_a	**Harvested meadow**	**Wet meadow**	**Alder stand**	**Forest**	**Sparse vegetation**	**Water**	**Asphalt**
4:50	10.5	1.13	9.3	10.0	10.1	12.0	13.2	20.4	16.1
5:30	11.8	0.81	13.4	12.2	12.9	12.7	14.9	20.7	16.4
6:00	15.2	0.68	16.7	14.6	13.8	14.3	16.5	20.4	19.1
7:10	18.5	1.16	22.6	18.4	17.2	17.1	20.6	21.0	24.7
8:10	22.0	1.02	31.0	23.0	21.2	20.6	26.2	22.9	31.2
9:10	25.0	0.71	35.1	25.0	22.8	22.0	28.8	23.4	34.8
10:40	28.0	0.49	42.0	29.4	26.7	26.1	34.9	26.0	42.6
13:10	30.1	0.51	44.2	31.9	28.9	29.0	37.2	27.7	47.6
14:00	30.0	0.97	42.6	31.7	28.7	28.6	36.2	29.1	46.6
15:10	30.7	0.64	39.9	30.0	27.6	28.3	35.2	28.7	44.9
16:10	31.0	0.52	35.5	28.9	26.4	27.9	32.5	29.3	41.9
17:10	31.1	0.88	31.6	26.4	26.0	27.1	30.6	28.3	38.8
18:10	31.0	0.64	26.0	23.3	23.4	26.4	27.1	28.1	33.8
18:40	28.6	1.62	23.5	22.1	22.4	26.1	25.0	28.3	31.9
19:10	26.7	2.11	19.8	19.2	20.4	24.4	23.1	27.2	29.7
20:10	20.6	1.62	15.4	16.2	18.7	22.5	21.1	27.4	27.6

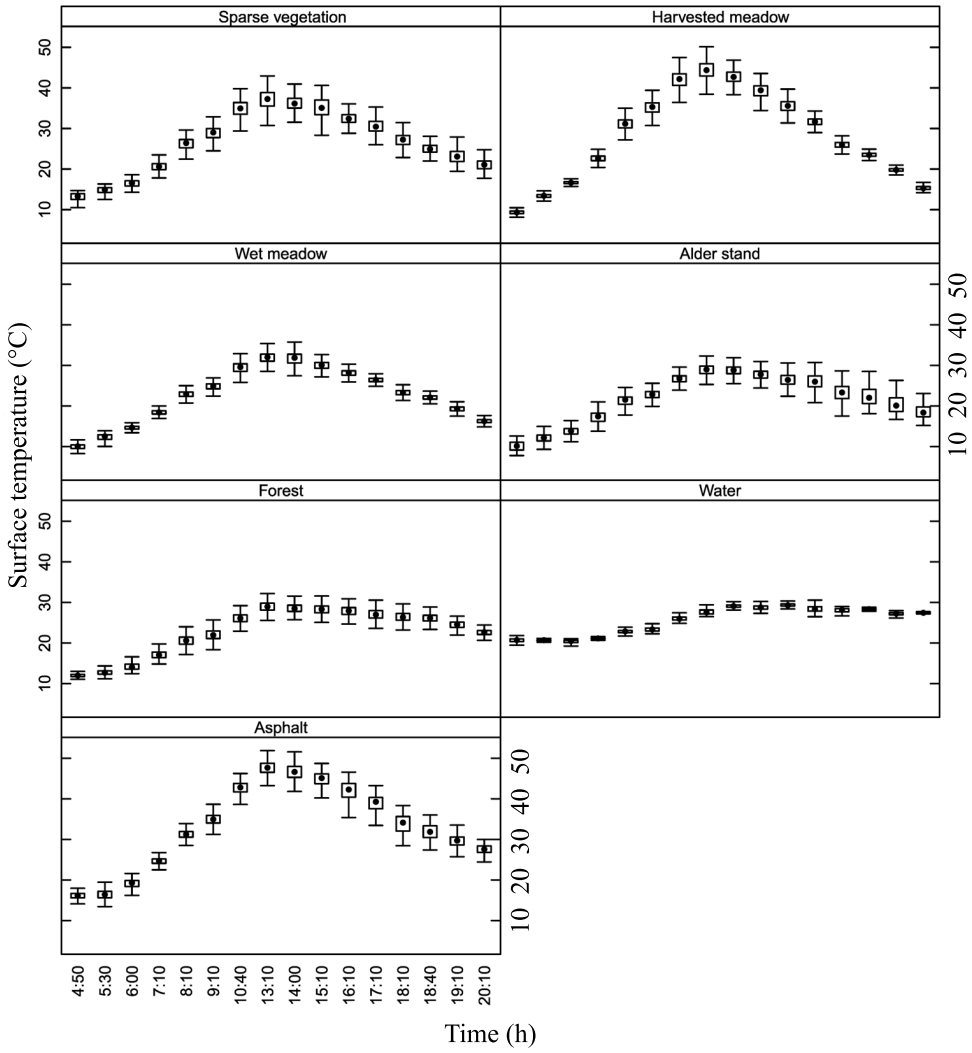

Figure 10.1 Daily courses of surface temperature (T_s) on seven studied localities. Each point is calculated from 1000 randomly selected pixel values. Points describe the median of the data, boxes are lower and upper quartiles and whiskers show 1.5 times of interquartile range of the data or maximum and minimum values. Extreme values are not shown in the graph.

The difference of T_s and T_a is usually mentioned in meteorological and climatological textbooks; however, the consequences resulting from this difference do not frequently appear in climate change discussions and recommendations and, what is the most important, are not commonly considered in climate change mitigation strategies. The large differences between both temperatures and between the sites with high temperature differences cause high temperature gradients –

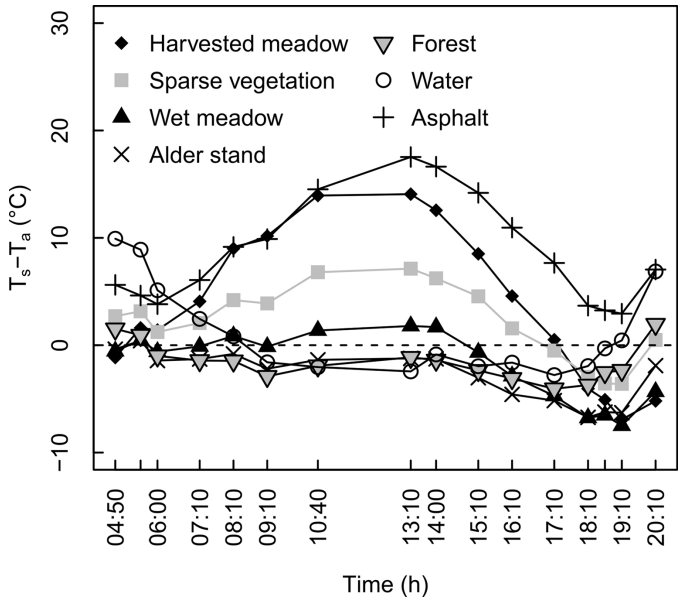

Figure 10.2 Diurnal changes of the difference between surface (T_s) and air (T_a) temperatures for seven land cover surfaces.

the consequence is higher turbulent heat flux, higher wind speeds and drainage of the landscape. A landscape without water converts the majority of incoming solar radiation into sensible heat, that it responsible for its heating. Our results show that water and its presence in the landscape – not only in the form of water bodies, but mainly its content in vegetation and soil, is able to balance temperature differences, keep surface temperature lower and therefore not lose water through a increase in evaporation over precipitation.

The relation between vegetation and T_s is common knowledge – everybody knows that on a hot sunny day the air is cooler in a forest than on the concrete surface. It is the surface temperature that living organisms are in contact with, and which contributes to the microclimate within ecosystems that is crucial for the functioning of biological systems. Our results show that under high irradiance (maximum incoming solar energy was equal to $890\,\mathrm{W\,m^{-2}}$) the differences in T_s are extreme even within a highly varied agricultural landscape.

Intensification of agriculture and urbanization significantly disrupts the flows of energy. Due to landscape drainage, removal of functional and permanent vegetation (not only deforestation but also the loss of hedgerows, scattered vegetation, wetlands, wet meadows and preferences of thermophilous crops), leads to overheating of the landscape and its degradation; this may result in rapid removals of nutrients. The surface temperature of agriculture landscape during late ripening and above all after crops harvesting, has the same values as the industrial and mining landscape (Hesslerová & Pokorný 2010b). Therefore land managers (own-

ers, farmers, foresters, fishermen) should be considered as significant controllers of the solar energy distribution, i.e. "local climate constructors" namely through reasonable water and vegetation management.

Recommended Reading

Hesslerová, P., Pokorný, J., Brom, J. & Rejšková-Procházková, A. 2013. Daily dynamics of radiation surface temperature of different land cover types in a temperate cultural landscape: Consequences for the local climate. *Ecological Engineering* 54: 145–154.

Quattrochi, D.A. & Luvall, J.C. 2004. *Thermal Remote Sensing in Land Surface Processing.* CRC Press.

REFERENCES

Adamchuk, V.I., Ferguson, R.B. & Herbert, G.W. 2010. Soil heterogeneity and crop growth. *Precision Crop Protection - the Challenge and Use of Heterogeneity*, editors E.C. Oerke, R. Gerhards, G. Menz & R.A. Sikora, 3–16, Springer, Dordrecht; Heidelberg [u.a.].

Adamchuk, V.I., Hummel, J.W., Morgan, M.T. & Upadhyaya, S.K. 2004. On-the-go soil sensors for precision agriculture. *Computers and Electronics in Agriculture* 44: 71–91.

Adler-Golden, S.M., Matthew, M.W., Bernstein, L.S., Levine, R.Y., Berk, A., Richtsmeier, S.C., Acharya, P.K., Anderson, G.P., Felde, J.W., Gardner, J.A., Hoke, M.L., Jeong, L.S., Pukall, B., Ratkowski, A.J. & Burke, H.h.K. 1999. Atmospheric correction for shortwave spectral imagery based on MODTRAN4. *SPIE Proceedings on Imaging Spectrometry*, vol. 3753, 61–69.

Alberti, G., Boscutti, F., Pirotti, F., Bertacco, C., De Simon, G., Sigura, M., Cazorzi, F. & Bonfanti, P. 2013. A LiDAR-based approach for a multi-purpose characterization of alpine forests: an italian case study. *iForest - Biogeosciences and Forestry* 6: 156–168.

Arregui, L.M., Lasa, B., Lafarga, A., Irañeta, I., Baroja, E. & Quemada, M. 2006. Evaluation of chlorophyll meters as tools for N fertilization in winter wheat under humid mediterranean conditions. *European Journal of Agronomy* 24: 140–148.

Asner, G., Hicke, J. & Lobell, D.B. 2003. Per-pixel analysis of forest structure: Vegetation indices, spectral mixture analysis and canopy reflectance modeling. *Remote sensing of forest environments. Concepts and case studies*, editors M. Wulder & S. Franklin, 209–254, Kluwer Academic Publishers, Boston.

Atzberger, C. 2004. Object-based retrieval of biophysical canopy variables using artificial neural nets and radiative transfer models. *Remote Sensing of Environment* 93: 53–67.

Axelsson, P. 2000. DEM generation from lasr scanner data using adaptive TIN models. *International Archives of Photogrammetry and Remote Sensing* 33: 110–117.

Baldridge, A., Hook, S., Grove, C. & Rivera, G. 2009. The ASTER spectral library version 2.0. *Remote Sensing of Environment* 113: 711–715.

Baltsavias, E.P. 1999. Airborne laser scanning: existing systems and firms and other resources. *ISPRS Journal of Photogrammetry and Remote Sensing* 54: 164–198.

Baret, F. & Buis, S. 2008. Estimating canopy characteristics from remote sensing obsrvations: Review of methods and associated problems. *Advances in Land Remote Sensing: System, Modeling, Inversion and Application*, editor S. Liang, 173–201, Springer.

Baret, F. & Guyot, G. 1991. Potentials and limits of vegetation indices for LAI and APAR assessment. *Remote Sensing of Environment* 35: 161–173.

Barnsley, M., Settle, J., Cutter, M., Lobb, D. & Teston, F. 2004. The PROBA/CHRIS mission: a low-cost smallsat for hyperspectral multiangle observations of the earth surface and atmosphere. *IEEE Transactions on Geoscience and Remote Sensing* 42: 1512–1520.

Baumgardner, M.F., Silva, L.F., Biehl, L.L., Stoner, E.R. & Brady, N.C. 1985. Reflectance properties of soils. *Advances in Agronomy*, vol. Volume 38, 1–44, Academic Press.

Beal, D. & Eamon, M. 2009. Preliminary results of testing and a proposal for radiometric error correction using dynamic, parabolic linear transformations of "stepped" data (PCORRECT.EXE). Tech. rep., Analytical Spectral Devices, Inc.

Bell, F. & Donnelly, L. 2006. *Mining and its Impact on the Environment*. Taylor & Francis, London.

Ben-Dor, E., Chabrillat, S., Dematt, J.A.M., Taylor, G.R., Hill, J., Whiting, M.L. & Sommer, S. 2009. Using imaging spectroscopy to study soil properties. *Remote Sensing of Environment* 113: S38–S55.

Ben-Dor, E., Inbar, Y. & Chen, Y. 1997. The reflectance spectra of organic matter in the visible near-infrared and short wave infrared region (400–2500 nm) during a controlled decomposition process. *Remote Sensing of Environment* 61: 1–15.

Berk, A., Anderson, G., Acharya, P., Bernstein, L.S.,

Muratov, L., Lee, J., Fox, M., Adler-Golden, S.M., Chetwynd, J.H., Hoke, M.L., Lockwood, R., Gardner, J.A., Cooley, T., Borel, C.C., Lewis, P.E. & Shettle, E. 2006. MODTRAN5: 2006 update. *Proc. SPIE* Vol. 6233, 62331F.

Berk, A., Bernsten, L. & Robertson, D. 1989. MODTRAN: A moderate resolution model for LOWTRAN7. Tech. rep., Air Force Geophysics Laboratory, Hanscom AFB, MA.

Bo, Z., Wei, G., Shuo, S. & Shalei, S. 2011. A multi-wavelength canopy LiDAR for vegetation monitoring: System implementation and laboratory-based tests. *Procedia Environmental Sciences* 10, Part C: 2775–2782.

Bornemann, L., Welp, G., Brodowski, S., Rodionov, A. & Amelung, W. 2008. Rapid assessment of black carbon in soil organic matter using mid-infrared spectroscopy. *Organic Geochemistry* 39: 1537–1544.

Bradshaw, A. 1997. Restoration of mined lands—using natural processes. *Ecological Engineering* 8: 255–269.

Brady, N.C. & Weil, R.R. 1999. *The nature and properties of soils*. Prentice Hall, Upper Saddle River.

Brandtberg, T., Warner, T.A., Landenberg, R.E. & McGraw, J.B. 2003. Detection and analysis of individual leaf-off tree crowns in small footprint, high sampling density lidar data from the eastern deciduous forest in north america. *Remote Sensing of Environment* 85: 290–303.

Breidenbach, J., Næsset, E., Lien, V., Gobakken, T. & Solberg, S. 2010. Prediction of species specific forest inventory attributes using a nonparametric semi-individual tree crown approach based on fused airborne laser scanning and multispectral data. *Remote Sensing of Environment* 114: 911–924.

Broge, N.H. & Leblanc, E. 2001. Comparing prediction power and stability of broadband and hyperspectral vegetation indices for estimation of green leaf area index and canopy chlorophyll density. *Remote Sensing of Environment* 76: 156–172.

Brázdil, J. 2012. Technická zpráva k digitálnímu modelu reliéfu 5. generace (DMR 5G). (in Czech). Tech. rep., Český zeměměřičský úřad (Czech Office for Surveying, Mapping and Cadastre).

Bunting, P. & Lucas, R. 2006. The delineation of tree crowns in australian mixed species forests using hyperspectral compact airborne spectrographic imager (CASI) data. *Remote Sensing of Environment* 101: 230–248.

Campbell, J.B. & Wynne, R.H. 2011. *Introduction to remote sensing (5th edition)*. The Guilford Press, 72 Spring Street, New York NY 10012.

Carson, W.W., Andersen, H.E., Reutebuch, S.E. & McGaughey, R.J. 2004. LiDAR applications in forestry: An overview. *Annual ASPRES Conference Proceedings*, Denver, USA.

Carter, G. 1994. Ratios of leaf reflectances in narrow wavebands as indicators of plant stress. *International Journal of Remote Sensing* 15: 697–703.

Casa, R., Castaldi, F., Pascucci, S., Palombo, A. & Pignatti, S. 2013. A comparison of sensor resolution and calibration strategies for soil texture estimation from hyperspectral remote sensing. *Geoderma* 197–198: 17–26.

CESBIO 2013, DART user's manual (release may 24, 213).

Chang-Hua, J., Yong-Chao, T., Xia, Y., Wei-Xing, C., Yan, Z. & Hannaway, D. 2010. Estimating leaf chlorophyll content using red edge parameters. *Pedosphere* 20: 633–644.

Chen, Q., Baldocchi, D., Gong, P. & Kelly, M. 2006. Isolating individual trees in a savanna woodland using small footprint lidar data. *Photogrammetric Engineering & Remote Sensing* 72: 923–932.

Cheng, C., Wei, Y., Sun, X. & Zhou, Y. 2013. Estimation of chlorophyll-a concentration in turbid lake using spectral smoothing and derivative analysis. *International Journal of Environmental Research and Public Health* 10: 2979–2994.

Cho, M.A. & Skidmore, A.K. 2006. A new technique for extracting the red edge position from hyperspectral data: The linear extrapolation method. *Remote Sensing of Environment* 101: 181–193.

Choi, K.Y. & Milton, E.J. 2001. A model-based approach to correcting spectral irradiance data using and upward-looking airborne sensor (CASI ILS) .

Chorus, I. 2001. *Cyanotoxins: occurrence, causes, consequences*. Springer-Verlag Berlin Heidelberg.

Chorus, I., Bartram, J., Falconer, I.R. & Salas, H.J. 2000. Health risks caused by freshwater cyanobacteria in recreational waters. *Journal of Toxicology and Environmental Health, Part B* 3: 323–347.

Christy, C.D. 2008. Real-time measurement of soil attributes using on-the-go near infrared reflectance spectroscopy. *Computers and Electronics in Agriculture* 61: 10–19.

Cibulka, M. & Mikita, T. 2011. Přesnost digitálního modelu reliéfu vytvořeného z dat leteckého laserového skenování v lesních porostech (in Czech). *Geodetický a kartografický obzor* 57: 264–267.

Cohen, W.B. & Goward, S.N. 2004. Landsat's role in ecological applications of remote sensing. *BioScience* 54: 535–545.

Colombo, R., Bellingeri, D., Fasolini, D. & Marino, C.M. 2003. Retrieval of leaf area index in different vegetation types using high resolution satellite data. *Remote Sensing of Environment* 86: 120–131.

Combal, B., Baret, F., Weiss, M., Trubuil, A., Mace, D., Pragnere, A., Myneni, R., Knyazikhin, Y. & Wang, L. 2002. Retrieval of canopy biophysical variables from bidirectional reflectance: Using prior information to solve the ill-posed inverse problem. *Remote Sensing of Environment* 84: 1–15.

Corwin, D.L. & Lesch, S.M. 2003. Application of soil electrical conductivity to precision agriculture: Theory, principles, and guidelines. *Agronomy Journal* 95: 455–471.

Corwin, D.L. & Lesch, S.M. 2005. Apparent soil electrical conductivity measurements in agriculture. *Computers and Electronics in Agriculture* 46: 11–43.

Corwin, D.L. & Plant, R.E. 2005. Applications of apparent soil electrical conductivity in precision agriculture. *Computers and Electronics in Agriculture* 46: 1–10.

Croft, H., Chen, J.M., Zhang, Y. & Simic, A. 2013. Modelling leaf chlorophyll content in broadleaf and needle leaf canopies from ground, CASI, landsat TM 5 and MERIS reflectance data. *Remote Sensing of Environment* 133: 128–140.

Culvenor, D.S. 2002. TIDA: an algorithm for the delineation of tree crowns in high spatial resolution remotely sensed imagery. *Computers & Geosciences* 28: 33–44.

Curran, P.J., Dungan, J.L. & Peterson, D.L. 2001. Estimating the foliar biochemical concentration of leaves with reflectance spectrometry testing the

kokaly and clark methodologies. *Remote Sensing of Environment* 76: 349–359.

Darvishzadeh, R., Matkan, A. & Dashti Ahangar, A. 2012. Inversion of a radiative transfer model for estimation of rice canopy chlorophyll content using a lookup-table approach. *IEEE Journal of Selected Topics in Applied Earth Observations and Remote Sensing* 5: 1222–1230.

Dash, J. & Curran, P.J. 2004. The MERIS terrestrial chlorophyll index. *International Journal of Remote Sensing* 25: 5403–5413.

Datt, B. 1998. Remote sensing of chlorophyll a, chlorophyll b, chlorophyll a+b, and total carotenoid content in eucalyptus leaves. *Remote Sensing of Environment* 66: 111–121.

Datt, B. 1999. Visible/near infrared reflectance and chlorophyll content in eucalyptus leaves. *International Journal of Remote Sensing* 20: 2741–2759.

Daughtry, C.S.T., Walthall, C.L., Kim, M.S., de Colstoun, E.B. & McMurtrey, J.E. 2000. Estimating corn leaf chlorophyll concentration from leaf and canopy reflectance. *Remote Sensing of Environment* 74: 229–239.

Dawson, T.P. & Curran, P.J. 1998. Technical note a new technique for interpolating the reflectance red edge position. *International Journal of Remote Sensing* 19: 2133–2139.

Dawson, T.P., Curran, P.J. & Plummer, S.E. 1998. LIBERTY: Modeling the effects of leaf biochemical concentration on reflectance spectra. *Remote Sensing of Environment* 65: 50–60.

De Benedetto, D., Castrignanò, A., Rinaldi, M., Ruggieri, S., Santoro, F., Figorito, B., Gualano, S., Diacono, M. & Tamborrino, R. 2013. An approach for delineating homogeneous zones by using multisensor data. *Geoderma* 199: 117–127.

Delegido, J., Alonso, L., González, G. & Moreno, J. 2010. Estimating chlorophyll content of crops from hyperspectral data using a normalized area over reflectance curve (NAOC). *International Journal of Applied Earth Observation and Geoinformation* 12: 165–174.

Dickinson, Y., Zenner, E. & Miller, D. 2014. Examining the effect of diverse management strategies on landscape scale patterns of forest structure in pennsylvania using novel remote sensing techniques. *Canadian Journal of Forest Research* 44: 301–312.

Duan, H., Ma, R., Xu, X., Kong, F., Zhang, S., Kong, W., Hao, J. & Shang, L. 2009. Two-decade reconstruction of algal blooms in china's lake taihu. *Environmental Science & Technology* 43: 3522–3528.

Eiseltová, M., Pokorný, J., Hesslerová, P. & Ripl, W. 2012. Evapotranspiration – a driving force in landscape sustainablility. *Evapotranspiration - Remote Sensing and Modeling*, 305 – 328, InTech.

Erikson, M. 2003. Segmentation of individual tree crowns in colour aerial photographs using region growing supported by fuzzy rules. *Canadian Journal of Forest Research* 33: 1557–1563.

Fargasova, A. 1994. Effect of Pb, Cd, Hg, As, and Cr on germination and root-growth of sinapis-alba seeds. *Bulletin of Environmental Contamination and Toxicology* 52: 452–456.

Fargasova, A. 1998. Root growth inhibition, photosynthetic pigments production, and metal accumulation in Sinapis alba as the parameters for trace metals effect determination. *Bulletin of Environmental Contamination and Toxicology* 61: 762–769.

Feret, J.B., Francois, C., Asner, G.P., Gitelson, A.A., Martin, R.E., Bidel, L.P.R., Ustin, S.L., le Maire, G. & Jacquemoud, S. 2008. PROSPECT-4 and 5: Advances in the leaf optical properties model separating photosynthetic pigments. *Remote Sensing of Environment* 112: 3030–3043.

Fernandez-Diaz, J., Glennie, C., Carter, W., Shrestha, R., Sartori, M., Singhania, A., Legleiter, C. & Overstreet, B. 2014. Early results of simultaneous terrain and shallow water bathymetry mapping using a single-wavelength airborne LiDAR sensor. *IEEE Journal of Selected Topics in Applied Earth Observations and Remote Sensing* 7: 623–635.

Filella, I. & Penuelas, J. 1994. The red edge position and shape as indicators of plant chlorophyll content, biomass and hydric status. *International Journal of Remote Sensing* 15: 1459–1470.

Frouz, J., Dvorščík, P., Vindušková, O. & Cienciala, E. 2014. Plant production, carbon accumulation and soil chemistry at post-mining sites. *Soil Biota and Ecosystem Development in Post Mining Sites*, editor J. Frouz, 88–103, CRC press, Boca Raton, FL.

Frouz, J., Hrčková, K., Lána, J., Krištůfek, V., Mudrák, O., Lukešová, A. & Mihaljevič, M. 2011. Can laboratory toxicity tests explain the pattern of field communities of algae, plants, and invertebrates along a toxicity gradient of post-mining sites? *Applied Soil Ecology* 51: 114–121.

Frouz, J., Krištůfek, V., Bastl, J., Kalčík, J. & Vaňková, H. 2005. Determination of toxicity of spoil substrates after brown coal mining using a laboratory reproduction test with enchytraeus crypticus (oligochaeta). *Water, Air, & Soil Pollution* 162: 37–47.

Gallo, K., Hale, R., Tarpley, D. & Yu, Y. 2011. Evaluation of the relationship between air and land surface temperature under clear- and cloudy-sky conditions. *Journal of applied Meteorology and Climatology* 767 – 775.

Gamon, J.A., Field, C.B., Bilger, W., Björkman, O., Fredeen, A.L. & Peñuelas, J. 1990. Remote sensing of the xanthophyll cycle and chlorophyll fluorescence in sunflower leaves and canopies. *Oecologia* 85: 1–7.

Ganapol, B.D., Johnson, L.F., Hammer, P.D., Hlavka, C.A. & Peterson, D.L. 1998. LEAFMOD: a new within-leaf radiative transfer model. *Remote Sensing of Environment* 63: 182–193.

Gao, B.C., Heidebrecht, K.B. & Goetz, A.F. 1993. Derivation of scaled surface reflectances from AVIRIS data. *Remote Sensing of Environment* 44: 165–178.

Gao, B.C., Montes, M.J., Davis, C.O. & Goetz, A.F.H. 2009. Atmospheric correction algorithms for hyperspectral remote sensing data of land and ocean. *Remote Sensing of Environment* 113, Supplement 1: S17–S24.

Gascon, F., Gastellu-Etchegorry, J.P., Lefevre-Fonollosa, M.J. & Dufrene, E. 2004. Retrieval of forest biophysical variables by inverting a 3-d radiative transfer model and using high and very high resolution imagery. *International Journal of Remote Sensing* 25: 5601–5616.

Gastellu-Etchegorry, J.P., Demarez, V., Pinel, V. & Zagolski, F. 1996. Modeling radiative transfer in heterogeneous 3-d vegetation canopies. *Remote Sensing of Environment* 58: 131–156.

Gastellu-Etchegorry, J.P., Martin, E. & Gascon, F. 2004. DART: a 3d model for simulating satellite

images and studying surface radiation budget. *International Journal of Remote Sensing* 25: 73–96.

Giardino, C., Bresciani, M., Valentini, E., Gasperini, L., Bolpagni, R. & Brando, V.E. 2014. Airborne hyperspectral data to assess suspended particulate matter and aquatic vegetation in a shallow and turbid lake. *Remote Sensing of Environment*.

Gitelson, A. & Merzlyak, M. 1994. Spectral relfectance changes associated with autumn senescence of aesculus hippocastanum l. and acer platanoides l. leaves. spectral features and relation to chlorophyll estimation. *Journal of Plant Physiology* 143: 286–292.

Gitelson, A.A., Gritz, Y. & Merzlyak, M.N. 2003. Relationships between leaf chlorophyll content and spectral reflectance and algorithms for non-destructive chlorophyll assessment in higher plant leaves. *Journal of Plant Physiology* 160: 271–282.

Gitelson, A.A., Merzlyak, M.N. & Lichtenthaler, H.K. 1996. Detection of red edge position and chlorophyll content by reflectance measurements near 700 nm. *Journal of Plant Physiology* 148: 501–508.

Gitelson, A.A., Schalles, J.F. & Hladik, C.M. 2007. Remote chlorophyll-a retrieval in turbid, productive estuaries: Chesapeake bay case study. *Remote Sensing of Environment* 109: 464–472.

Gökkaya, K., Thomas, V., Noland, T., McCaughey, H. & Treitz, P. 2014. Testing the robustness of predictive models for chlorophyll generated from spaceborne imaging spectroscopy data for a mixedwood boreal forest canopy. *International Journal of Remote Sensing* 35: 218–233.

Goddard, V., Baker, A., Davy, J., Adams, D., De Ville, M., Thackeray, S., Maberly, S. & Wilson, W. 2005. Temporal distribution of viruses, bacteria and phytoplankton throughout the water column in a freshwater hypereutrophic lake. *Aquatic Microbial Ecology* 39: 211–223.

Godwin, R.J. & Miller, P.C.H. 2003. A review of the technologies for mapping within-field variability. *Biosystems Engineering* 84: 393–407.

Gougeon, F.A. 1995. A crown-following approach to the automatic delineation of individual tree crowns in high spatial resolution digital images. *Canadian Journal of Remote Sensing* 21: 274–284.

Govaerts, Y.M. & Verstraete, M.M. 1998. Raytran: A monte carlo ray-tracing model to compute light scattering in three-dimensional heterogeneous media. *IEEE Transactions on Geoscience and Remote Sensing* 36: 493–505.

Gower, J.F.R., Borstad, G.A., Anger, G.D. & Edel, H.R. 1992. CCD-based imaging spectroscopy for remote sensing: The FLI and CASI programs. *Canadian Journal of Remote Sensing* 18.

Gregor, J., Geriš, R., Maršálek, B., Heteša, J. & Marvan, P. 2005. In situ quantification of phytoplankton in reservoirs using a submersible spectrofluorometer. *Hydrobiologia* 548: 141–151.

Gregor, J. & Maršálek, B. 2004. Freshwater phytoplankton quantification by chlorophyll a: a comparative study of in vitro, in vivo and in situ methods. *Water Research* 38: 517–522.

Gregor, J., Maršálek, B. & Šípková, H. 2007. Detection and estimation of potentially toxic cyanobacteria in raw water at the drinking water treatment plant by in vivo fluorescence method. *Water Research* 41: 228–234.

Gu, D., Gillespie, A., Kahle, A. & Palluconi, F. 2000. Autonomous atmospheric compensation (AAC) of high resolution hyperspectral thermal infrared remote-sensing imagery. *IEEE Transactions on Geoscience and Remote Sensing* 38: 2557–2570.

Gupta, S., Weinacker, H. & Koch, B. 2010. Comparative analysis of clustering-based approaches for 3-d single tree detection using airborne fullwave lidar data. *Remote Sensing* 2: 968–989.

Guyot, G. & Baret, F. 1988. Utilisation de la haute resolution spectrale pour suivre l'etat des couverts vegetaux. 279.

Guyot, G., Baret, F. & Major, D. 1988. High spectral resolution: determination of spectral shifts between the red and the near infrared. *International Archives of Photogrammetry and Remote Sensing* 11: 750–760.

Haboudane, D., Miller, J.R., Tremblay, N., Zarco-Tejada, P.J. & Dextraze, L. 2002. Integrated narrow-band vegetation indices for prediction of crop chlorophyll content for application to precision agriculture. *Remote Sensing of Environment* 81: 416–426.

Hansen, M.C. & Loveland, T.R. 2012. A review of large area monitoring of land cover change using landsat data. *Remote Sensing of Environment* 122: 66–74.

Hanuš, J., Fabiánek, T., Kaplan, V. & Homolová, L. 2014. Flying laboratory of imaging systems (FLIS) at CzechGlobe. *14^{th} International Multidisciplinary scientific conference SGEM 2014 on Informatics, Geoinformatics and Remote Sensing*, vol. III, 177–182, 17-26, June 2014, Bulgaria.

Hedley, J.D., Harborne, A.R. & Mumby, P.J. 2005. Simple and robust removal of sun glint for mapping shallow-water benthos. *International Journal of Remote Sensing* 26: 2107–2112.

Heege, H.J., Reusch, S. & Thiessen, E. 2008. Prospects and results for optical systems for site-specific on-the-go control of nitrogen-top-dressing in germany. *Precision Agriculture* 9: 115–131.

Heinzel, J. & Koch, B. 2011. Exploring full-waveform LiDAR parameters for tree species classification. *International Journal of Applied Earth Observation and Geoinformation* 13: 152–160.

Hesslerová, P. & Pokorný, J. 2010a. Forest clearing, water loss, and land surface rating as development costs. *International Journal of Water* 5: 401 – 418.

Hesslerová, P. & Pokorný, J. 2010b. The synergy of solar radiation, plant biomass, and humidity as an indicator of ecological functions of the landscape: A case study from central europe. *Integrated Environmental Assessment and Management* 6: 249 – 259.

Hesslerová, P., Pokorný, J., Brom, J. & Rejšková Procházková, A. 2013. Daily dynamics of radiation surface temperature of different land cover types in a temperate cultural landscape: Consequences for the local climate. *Ecological Engineering* 145 – 154.

Heurich, M., Schneider, T. & Kennel, E. 2003. Laser scanning for identification of forest structures in the bavarian forest national park. *Proceedings of the ScandLaser scientific worskhop on airborne laser scanning of forests.*, 98–107, Swedish University of Agricultural Sciences, Umea, Sweeden.

Hirschmugl, M., Ofner, M., Raggam, J. & Schardt, M. 2007. Single tree detection in very high resolution remote sensing data. *Remote Sensing of Environment* 110: 533–544.

Hilker, T., Coops, N.C., Wulder, M.A., Black, T.A. & Guy, R.D. 2008. The use of remote sensing in light use efficiency based models of gross primary production: A review of current status and future requirements. *Science of the Total Environment* 404: 411–423.

Holopainen, M. & Hyyppä, J. 2003. Possibilities with laser scanning in practical forestry. *Proceedings of the ScandLaser scientific worskhop on airborne laser scanning of forests.*, 265–274, Swedish University of Agricultural Sciences, Umea, Sweeden.

Holopainen, M., Mäkinen, A., Rasinmäki, J., Hyyppä, J., Hyyppä, H., Kaartinen, H., Viitala, R., Vastaranta, M. & Kangas, A. 2010. Effect of tree-level airborne laser-scanning measurement accuracy on the timing and expected value of harvest decisions. *European Journal of Forest Research* 129: 899–907.

Holopainen, M., Vastaranta, M. & Hyyppä, J. 2014. Outlook for the next generation's precision forestry in finland. *Forests* 5: 1682–1694.

Homolová, L., Malenovský, Z., Clevers, J., García-Santos, G. & Schaepman, M. 2013. Review of optical-based remote sensing for plant trait mapping. *Ecological Complexity* 15: 1–16.

Houborg, R., Anderson, M. & Daughtry, C. 2009. Utility of an image-based canopy reflectance modeling tool for remote estimation of LAI and leaf chlorophyll content at the field scale. *Remote Sensing of Environment* 113: 259–274.

Hyyppä, H. & Hyyppä, J. 1999. Comparing the accuracy of laser scanner with other optical remote sensing data sources for stand attribute retrieval. *The Photogrammetric Journal of Finland* 16: 5–15.

Hyyppä, J. & Inkinen, M. 1999. Detecting and estimating attributes for single trees using laser scanner. *The Photogrammetric Journal of Finland* 16: 27–42.

IPCC, 2007. Climate change: the physical science basis. *Contribution of Working Group I to the Fourth Assessment Report of the Intergovernmental Panel on Climate Change* 996–996.

Izydorczyk, K., Tarczynska, M., Jurczak, T., Mrowczynski, J. & Zalewski, M. 2005. Measurement of phycocyanin fluorescenceas an online early warning system for cyanobacteria in reservoir intake water. *Environmental Toxicology* 20: 425–430.

Jacquemoud, S. & Baret, F. 1990. PROSPECT: A model of leaf optical properties spectra. *Remote Sensing of Environment* 34: 75–91.

Jacquemoud, S., Verhoef, W., Baret, F., Bacour, C., Zarco-Tejada, P.J., Asner, G.P., Francois, C. & Ustin, S.L. 2009. PROSPECT + SAIL models: A review of use for vegetation characterization. *Remote Sensing of Environment* 113: S56–S66.

Janik, L.J., Skjemstad, J.O., Shepherd, K.D. & Spouncer, L.R. 2007. The prediction of soil carbon fractions using mid-infrared-partial least square analysis. *Australian Journal of Soil Research* 45: 73–73.

Jirka, V., Pokorný, J., Kobrzek, F., Mareček, P., Zicha, J. & Bíla, J., 2011, Soustava prostředků pro zjišťování energetických toků v přízemní vrstvě atmosféry. Česká republika. Užitný vzor, 22671 u1. 2011-09-12. (the system for detecting energy flows in the ground layer of the atmosphere. the czech republic. utility model, 22671 u1. 2011-09-12.).

Jupp, D., Kirk, J. & Harris, G. 1994. Detection, identification and mapping of cyanobacteria — using remote sensing to measure the optical quality of turbid inland waters. *Marine and Freshwater Research* 45: 801–828.

Jutzi, B. & Gross, H. 2007. Normalization of lidar intensity data based on range and surface incidence angle. ETH, Zürich, Switzerland, July 9-12, 2007.

Kahru, M., Savchuk, O. & Elmgren, R. 2007. Satellite measurements of cyanobacterial bloom frequency in the baltic sea: interannual and spatial variability. *Marine Ecology Progress Series* 343: 15–23.

Karu, H., Szava-Kovats, R., Pensa, M. & Kull, O. 2009. Carbon sequestration in a chronosequence of scots pine stands in a reclaimed opencast oil shale mine. *Canadian Journal of Forest Research-Revue Canadienne De Recherche Forestiere* 39: 1507–1517.

Katsiabani, K., Adaktilou, N. & Cartalis, C. 2009. A generalised methodology for estimating land surface temperature for non-urban areas of Greece through the combined use of NOAA–AVHRR data and ancillary information. 43, 930–940. *Advances in Space Research* 930 – 940.

Kříbek, B., Strnad, M., Boháček, Z., Sýkorová, I., Čejka, J. & Sobalík, Z. 1998. Geochemistry of miocene lacustrine sediments from the Sokolov coal basin (Czech Republic). *International Journal of Coal Geology* 37: 207–233.

Kedziora, A. 2010. Landscape management practices for maintenance and enhancement of ecosystem services in countryside. *Ecohydrology & Hydrobiology* 10: 133 – 152.

Křen, J., Klem, K., Svobodová, I., Míša, P. & Neudert, L. 2014. Yield and grain quality of spring barley as affected by biomass formation at early growth stages. *Plant Soil and Environment* 60: 221–227.

Křen, J., Lukas, V., Svobodová, I., Dryšlová, T., Míša, P. & Neudert, L. 2009. Possibilities of cereal canopy assessment by using the NDVI. In *Proceedings of Precision Agriculture '09*, E.J. van Henten, D. Goense & C. Lokhorst (Eds.), 151–158, Wageningen Academic Publishers.

Kimes, D., Gastellu-Etchegorry, J. & Esteve, P. 2002. Recovery of forest canopy characteristics through inversion of a complex 3d model. *Remote Sensing of Environment* 79: 320–328.

Kirilin, A., Achmetov, R., Stratilatov, N., Baklanov, A., Fedorov, V. & Novikov, M. 2010. Spacecraft resurs-p. *Geomatics by Sovzond* 4: 23–25 (in Russian).

Koch, B., Heyder, U. & Weinacker, H. 2006. Detection of individual tree crowns in airborne lidar data. *Photogrammetric Engineering & Remote Sensing* 72: 357–363.

Kokaly, R.F., Asner, G.P., Ollinger, S.V., Martin, M.E. & Wessman, C.A. 2009. Characterizing canopy biochemistry from imaging spectroscopy and its application to ecosystem studies. *Remote Sensing of Environment* 113: S78–S91.

Kokaly, R.F. & Clark, R.N. 1999. Spectroscopic determination of leaf biochemistry using band-depth analysis of absorption features and stepwise multiple linear regression. *Remote Sensing of Environment* 67: 267–287.

Korpela, I., Ørka, H.O., Maltamo, M., Tokola, T. & Hyyppä, J. 2010. Tree species classification using airborne LiDAR—effects of stand and tree parameters, downsizing of training set, intensity normalization, and sensor type. *Silva Fennica* 44: 319–339.

Kotchenova, S.Y., Vermote, E.F., Matarrese, R. & Klemm Jr, F.J. 2006. Validation of a vector version of the 6s radiative transfer code for atmo-

spheric correction of satellite data. part i: Path radiance. *Applied Optics* 45: 6762–6774.

Kruse, F., Lefkoff, A., Boardman, J., Heidebrecht, K., Shapiro, A., Barloon, P. & Goetz, A. 1993. The spectral image processing system (SIPS)—interactive visualization and analysis of imaging spectrometer data. *Remote Sensing of Environment* 44: 145–163.

Kruse, F.A. 2004. Comparison of ATREM, ACORN, and FLAASH atmospheric corrections using low-altitude AVIRIS data of boulder, CO. *13th JPL Airborne Geoscience Workshop*.

Kunkel, B., Blechinger, F., Viehmann, D., Van Der Piepen, H. & Doerffer, R. 1991. ROSIS imaging spectrometer and its potential for ocean parameter measurements (airborne and spaceborne). *International Journal of Remote Sensing* 12: 753–761.

Kwak, D.A., Lee, W.K., Lee, J.H., Biging, G.S. & Gong, P. 2007. Detection of individual trees and estimation of tree height using LiDAR data. *Journal of Forest Research* 12: 425–434.

Laurent, V.C.E., Verhoef, W., Clevers, J.G.P.W. & Schaepman, M.E. 2011. Estimating forest variables from top-of-atmosphere radiance satellite measurements using coupled radiative transfer models. *Remote Sensing of Environment* 115: 1043–1052.

Laurent, V.C.E., Verhoef, W., Damm, A., Schaepman, M.E. & Clevers, J.G.P.W. 2013. A bayesian object-based approach for estimating vegetation biophysical and biochemical variables from APEX at-sensor radiance data. *Remote Sensing of Environment* 139: 6–17.

Le, C., Li, Y., Zha, Y., Sun, D., Huang, C. & Lu, H. 2009. A four-band semi-analytical model for estimating chlorophyll a in highly turbid lakes: The case of Taihu lake, China. *Remote Sensing of Environment* 113: 1175–1182.

le Maire, G., François, C. & Dufrêne, E. 2004. Towards universal broad leaf chlorophyll indices using PROSPECT simulated database and hyperspectral reflectance measurements. *Remote Sensing of Environment* 89: 1–28.

le Maire, G., François, C., Soudani, K., Berveiller, D., Pontailler, J.Y., Bréda, N., Genet, H., Davi, H. & Dufrêne, E. 2008. Calibration and validation of hyperspectral indices for the estimation of broadleaved forest leaf chlorophyll content, leaf mass per area, leaf area index and leaf canopy biomass. *Remote Sensing of Environment* 112: 3846–3864.

Leckie, D., Gougeon, F., Hill, D., Quinn, R., Armstrong, L. & Shreenan, R. 2003. Combined high-density lidar and multispectral imagery for individual tree crown analysis. *Canadian Journal of Remote Sensing* 29: 633–649.

Leonenko, G., Los, S.O. & North, P.R.J. 2013. Statistical distances and their applications to biophysical parameter estimation: Information measures, m-estimates, and minimum contrast methods. *Remote Sensing* 5: 1355–1388.

Lhotáková, Z., Albrechtová, J., Malenovský, Z., Rock, B.N., Polák, T. & Cudlín, P. 2007. Does the azimuth orientation of norway spruce (*Picea abies*/L./Karst.) branches within sunlit crown part influence the heterogeneity of biochemical, structural and spectral characteristics of needles? *Environmental and Experimental Botany* 59: 283–292.

Li, F., Mistele, B., Hu, Y., Chen, X. & Schmidhalter, U. 2014. Reflectance estimation of canopy nitrogen content in winter wheat using optimised hyperspectral spectral indices and partial least squares regression. *European Journal of Agronomy* 52: 198–209.

Li, Z.L., Tang, B.H., Wu, H., Ren, H., Yan, G., Wan, Z., Trigo, I.F. & Sobrino, J.A. 2013. Satellite-derived land surface temperature: Current status and perspectives. *Remote Sensing of Environment* 131: 14–37.

Liang, S. 2004. *Quantitative remote sensing of land surfaces*. John Wiley & Sons, Inc., Hoboken, New Jersey.

Lilienthal, H. 2003. *Entwicklung eines bodengestützten Fernerkundungssystems für die Landwirtschaft*, *Landbauforschung Völkenrode*, vol. Sonderheft 254. Bundesforschungsanst. für Landwirtschaft (FAL), Braunschweig.

Lillesand, T.M. & Kiefer, R.W. 2000. *Remote Sensing and Image Interpretation (4th edition)*. John Wiley & Sons, Inc., New York.

Lillesand, T.M., Kiefer, R.W. & Chipman, J.W. 2008. *Remote sensing and image interpretation*. John Wiley & Sons, Hoboken, NJ.

Loague, K. & Green, R.E. 1991. Statistical and graphical methods for evaluating solute transport models: Overview and application. *Journal of Contaminant Hydrology* 7: 51–73.

Lukas, V., Neudert, L. & Křen, J. 2011a. *Mapování variability půdy a porostů v precizním zemědělství*. Metodika pro praxi. Mendel University, Brno, Czech Republic.

Lukas, V., Ryant, P., Neudert, L., Dryšlová, T., Gnip, P. & Smutný, V. 2011b. *Tvorba aplikačních map pro základní hnojení plodin v precizním zemědělství*. Metodika pro praxi. Mendel University, Brno, Czech Republic.

Ma, S., Tao, Z., Yang, X., Yu, Y., Zhou, X. & Li, Z. 2014. Bathymetry retrieval from hyperspectral remote sensing data in optical-shallow water. *IEEE Transactions on Geoscience and Remote Sensing* 52: 1205–1212.

Machala, M. & Zejdová, L. 2014. Forest mapping through object-based image analysis of multispectral and LiDAR aerial data. *European Journal of Remote Sensing* 47: 117–131.

Maier, S.W., Ludeker, W. & Gunther, K.P. 1999. SLOP: A revised version of the stochastic model for leaf optical properties. *Remote Sensing of Environment* 68: 273–280.

Main, R., Cho, M.A., Mathieu, R., O'Kennedy, M.M., Ramoelo, A. & Koch, S. 2011. An investigation into robust spectral indices for leaf chlorophyll estimation. *ISPRS Journal of Photogrammetry and Remote Sensing* 66: 751–761.

Makarieva, A., Gorshkov, V. & Li, B.L. 2006. Conservation of water cycle on land via restoration of natural closed-canopy forests: implications for regional landscape planning. *Ecological Research* 21: 897 – 906.

Malenovský, Z., Albrechtová, J., Lhotáková, Z., Zurita-Milla, R., Clevers, J., Schaepman, M.E. & Cudlín, P. 2006. Applicability of the PROSPECT model for Norway spruce needles. *International Journal of Remote Sensing* 27: 5315–5340.

Malenovský, Z., Homolová, L., Zurita-Milla, R., Lukeš, P., Kaplan, V., Hanuš, J., Gastellu-Etchegorry, J.P. & Schaepman, M.E. 2013. Retrieval of spruce leaf chlorophyll content from airborne image data using continuum removal and radiative transfer. *Remote Sensing of Environment* 131: 85–102.

Malenovský, Z., Martin, E., Homolová, L., Gastellu-

Etchegorry, J.P., Zurita-Milla, R., Schaepman, M.E., Pokorný, R., Clevers, J.G.P.W. & Cudlín, P. 2008. Influence of woody elements of a norway spruce canopy on nadir reflectance simulated by the DART model at very high spatial resolution. *Remote Sensing of Environment* 112: 1–18.

Mallet, C. & Bretar, F. 2009. Full-waveform topographic lidar: State-of-the-art. *ISPRS Journal of Photogrammetry and Remote Sensing* 64: 1–16.

Maltamo, M. 2004. Estimation of timber volume and stem density based on scanning laser altimetry and expected tree size distribution functions. *Remote Sensing of Environment* 90: 319–330.

Maltamo, M., Packalén, P., Suvanto, A., Korhonen, K.T., Mehtätalo, L. & Hyvönen, P. 2009. Combining ALS and NFI training data for forest management planning: a case study in Kuortane, western Finland. *European Journal of Forest Research* 128: 305–317.

Maltese, A., Bates, P., Capodici, F., Cannarozzo, M., Ciraolo, G. & La Loggia, G. 2013. Critical analysis of thermal inertia approaches for surface soil water content retrieval. *Hydrological Sciences Journal* 58: 1144–1161.

Mandlburger, G., Pfennigbauer, M., Steinbacher, F. & Pfeifer, N. 2011. Airborne hydrographic LiDAR mapping-potential of a new technique for capturing shallow water bodies. *MODSIM2011, 19th International Congress on Modelling and Simulation, Modelling and Simulation Society of Australia and New Zealand*, 2416–2422.

Mariotto, I., Thenkabail, P.S., Huete, A., Slonecker, E.T. & Platonov, A. 2013. Hyperspectral versus multispectral crop-productivity modeling and type discrimination for the HyspIRI mission. *Remote Sensing of Environment* 139: 291–305.

Mas, J. & Flores, J. 2008. The application of artificial neural networks to the analysis of remotely sensed data. *International Journal of Remote Sensing* 29: 617–663.

McCoy, R.M. 2004. *Field Methods in Remote Sensing*. 1 edition ed., The Guilford Press, New York.

Michajlov, I. 1943. Zahlenmäßiges verfahren für die ausfürrung der Bestandeshöhenkurven. *Forstwissenschaftliches Centralblatt* 6: 273–279.

Michel, K., Terhoeven-Urselmans, T., Nitschke, R., Steffan, P. & Ludwig, B. 2009. Use of near- and mid-infrared spectroscopy to distinguish carbon and nitrogen originating from char and forest-floor material in soils. *Journal Of Plant Nutrition And Soil Science* 172: 63–70.

Mikita, T., Cibulka, M. & Janata, P. 2013a. Hodnocení přesnosti digitálních modelů reliéfu 4. a 5. generace v lesních porostech. *Geodetický a kartografický obzor* 59: 76–85.

Mikita, T., Klimánek, M. & Cibulka, M. 2013b. Evaluation of airborne laser scanning data for tree parameters and terrain modelling in forest environment. *Acta Universitatis Agriculturae et Silviculturae Mendelianae Brunensis* 61: 1339–1347.

Miller, J., Hare, E. & Wu, J. 1990. Quantitative characterization of the vegetation red edge reflectance 1. an inverted-gaussian reflectance model. *International Journal of Remote Sensing* 11: 1755–1773.

Milton, E.J., Schaepman, M.E., Anderson, K., Kneubühler, M. & Fox, N. 2009. Progress in field spectroscopy. *Remote Sensing of Environment* 113: S92–S109.

Ministry of Agriculture. 2010. *Angriculture status report 2009 (Zpráva o stavu zemědělství ČR za rok 2009)*. Ministry of Agriculture, Prague, Czech Republic.

Mishra, S., Mishra, D.R. & Schluchter, W.M. 2009. A novel algorithm for predicting phycocyanin concentrations in cyanobacteria: A proximal hyperspectral remote sensing approach. *Remote Sensing* 1: 758–775.

Montreuil, A.L., Levoy, F., Bretel, P. & Anthony, E.J. 2014. Morphological diversity and complex sediment recirculation on the ebb delta of a macrotidal inlet (Normandy, France): A multiple LiDAR dataset approach. *Geomorphology* 219: 114–125.

Mulder, V.L., de Bruin, S., Schaepman, M.E. & Mayr, T.R. 2011. The use of remote sensing in soil and terrain mapping — a review. *Geoderma* 162: 1–19.

Mutanga, O. & Skidmore, A.K. 2007. Red edge shift and biochemical content in grass canopies. *ISPRS Journal of Photogrammetry and Remote Sensing* 62: 34–42.

Norman, J.M. & Becker, F. 1995. Terminology in thermal infrared remote sensing of natural surfaces. *Agricultural and Forest Meteorology* 77: 153 – 166.

North, P.R.J. 1996. Three-dimensional forest light interaction model using a monte carlo method. *IEEE Transactions on Geoscience and Remote Sensing* 34: 946–956.

Novotný, J. 2014. Tree crown delineation using region growing and active contour: Approach introduction. *Mendel 2014: 20th International Conference on Soft Computing*, vol. 20, Brno University of Technology, Brno.

Næsset, E. 2004. Accuracy of forest inventory using airborne laser scanning: Evaluating the first nordic full-scale operational project. *Scandinavian Journal of Forest Research* 19: 554–557.

Šourková, M., Frouz, J. & Šantrůčková, H. 2005. Accumulation of carbon, nitrogen and phosphorus during soil formation on alder spoil heaps after brown-coal mining, near Sokolov (Czech Republic). *Geoderma* 124: 203–214.

Paerl, H.W. & Paul, V.J. 2012. Climate change: Links to global expansion of harmful cyanobacteria. *Water Research* 46: 1349–1363.

Pal Arya, S. 2001. *Introduction to Micrometeorology.*. No. 79 in International Geophysics Series, Academic Press, San Diego.

Pearlman, J., Barry, P., Segal, C., Shepanski, J., Beiso, D. & Carman, S. 2003. Hyperion, a space-based imaging spectrometer. *IEEE Transactions on Geoscience and Remote Sensing* 41: 1160–1173.

Penuelas, J., Filella, I., Biel, C., Serrano, L. & Save, R. 1993. The reflectance at the 950-970 nm region as an indicator of plant water status. *International Journal of Remote Sensing* 14: 1887–1905.

Penuelas, J., Gamon, J., Fredeen, A., Merino, J. & Field, C. 1994. Reflectance indices associated with physiological changes in nitrogen- and water-limited sunflower leaves. *Remote Sensing of Environment* 48: 135–146, cited By (since 1996)336.

Petráš, R. & Pajtík, J. 1991. Sústava československých objemových tabuliek drevín. *Lesnícky časopis* 37: 49–56.

Petrie, G. 2011. Airborne topographic laser scanners. *GEO Informatics* 14: 34–44.

Pierce, F.J. & Nowak, P. 1999. Aspects of precision agriculture. *Advances in Agronomy* 67: 1–85.

Pitkänen, J. 2001. Individual tree detection in digital aerial images by combining locally adaptive binarization and local maxima methods. *Canadian Journal of forest research* 31: 832–844.

Planck, M. 1900. Zur theorie des gesetzes der energieverteilung im normalspektrum. verhandlungen der deutschen physikalischen gesellschaft 2: 237. *ter Haar, D. 1967. On the Theory of the Energy Distribution Law of the Normal Spectrum. The Old Quantum Theory*, Pergamon Press, p. 82, LCNN 66029628.

Pokorný, J., Brom, J., Čermák, J., Hesslerová, P., Huryna, H., Nadezhdina, N. & Rejšková, A. 2010. How water and vegetation control solar energy fluxes and landscape heat. *International Journal of Water* 5: 311 – 336.

Pouliot, D.A., King, D.J. & Pitt, D.G. 2005. Development and evaluation of an automated tree detection delineation algorithm for monitoring regenerating coniferous forests. *Canadian Journal of Forest Research* 35: 2332–2345.

Qu, Z., Kindel, B. & Goetz, A.F.H. 2003. The high accuracy atmospheric correction for hyperspectral data (HATCH) model. *IEEE Transactions on Geoscience and Remote Sensing* 41: 1223–1231.

Quattrochi, D.A. & Luvall, J.C. 2004. *Thermal Remote Sensing in Land Surface Processing*. CRC Press.

Randolph, K., Wilson, J., Tedesco, L., Li, L., Pascual, D.L. & Soyeux, E. 2008. Hyperspectral remote sensing of cyanobacteria in turbid productive water using optically active pigments, chlorophyll a and phycocyanin. *Remote Sensing of Environment* 112: 4009–4019.

Rao, P.V.L., Gupta, N., Bhaskar, A.S.B. & Jayaraj, R. 2002. Toxins and bioactive compounds from cyanobacteria and their implications on human health. *Journal of environmental biology / Academy of Environmental Biology, India* 23: 215–224.

Richter, R. 2012. Atmospheric / topographic correction for airborne imagery (ATCOR-4 user guide, version 6.2 BETA). Tech. rep., DLR - German Aerospace Center, Wessling (Germany).

Richter, R. & Schläpfer, D. 2002. Geo-atmospheric processing of airborne imaging spectrometry data. Part 2: Atmospheric/topographic correction. *International Journal of Remote Sensing* 23: 2631–2649.

Ripl, W. 1995. Management of water cycle and energy flow for ecosystem control: the energy-transport-reaction (ETR) model. *Ecological Modelling* 78: 61 – 76.

Rivera, J.P., Verrelst, J., Leonenko, G. & Moreno, J. 2013. Multiple cost functions and regularization options for improved retrieval of leaf chlorophyll content and LAI through inversion of the PROSAIL model. *Remote Sensing* 5: 3280–3304.

Rodriguez-Moreno, F., Lukas, V., Neudert, L. & Dryšlová, T. 2014. Spatial interpretation of plant parameters in winter wheat. *Precision Agriculture* 15: 447–465.

Rouse, J.W., Haas, R.H., Schell, J.A. & Deering, D.W. 1974. Monitoring vegetation systems in the great plains with ERTS. *3rd ERTS-1 Symposium*, editors S. Fraden, E. Marcanti & M. Becker, 309–317, NASA SP-351, Washington D.C, USA.

Sampson, P.H., Zarco-Tejada, P.J., Mohammed, G.H., Miller, J.R. & Noland, T.L. 2003. Hyperspectral remote sensing of forest condition: Estimating chlorophyll content in tolerant hardwoods. *Forest Science* 49: 381–391.

Savitzky, A. & Golay, M.J.E. 1964. Smoothing and differentiation of data by simplified least squares procedures. *Analytical Chemistry* 36: 1627–1639.

Schaepman, M. 2009. Imaging spectrometers. *The SAGE Handbook of Remote Sensing*, editors T.A. Warner, M. Duane Nellis & G.M. Foody, 166–178, SAGE, London (UK).

Schaepman, M.E., Ustin, S.L., Plaza, A.J., Painter, T.H., Verrelst, J. & Liang, S. 2009. Earth system science related imaging spectroscopy - an assessment. *Remote Sensing of Environment* 113: S123–S137.

Schaepman-Strub, G., Schaepman, M.E., Painter, T.H., Dangel, S. & Martonchik, J.V. 2006. Reflectance quantities in optical remote sensing-definitions and case studies. *Remote Sensing of Environment* 103: 27–42.

Schläpfer, D. & Richter, R. 2002. Geo-atmospheric processing of airborne imaging spectrometry data. Part 1: Parametric orthorectification. *International Journal of Remote Sensing* 23: 2609–2630.

Schlerf, M. & Atzberger, C. 2006. Inversion of a forest reflectance model to estimate structural canopy variables from hyperspectral remote sensing data. *Remote Sensing of Environment* 100: 281–294.

Schlerf, M., Atzberger, C., Hill, J., Buddenbaum, H., Werner, W. & Schüler, G. 2010. Retrieval of chlorophyll and nitrogen in Norway spruce (*Picea abies* /L./Karst.) using imaging spectroscopy. *International Journal of Applied Earth Observation and Geoinformation* 12: 17–26.

Schneider, E. & Sagan, D. 2005. *Into the Cool: Energy Flow, Thermodynamics, and Life*. The University of Chicago Press, Chicago, London.

Schrödinger, E. 1944. *What is Life?* Cambridge University Press.

Sims, D.A. & Gamon, J.A. 2002. Relationships between leaf pigment content and spectral reflectance across a wide range of species, leaf structures and developmental stages. *Remote Sensing of Environment* 81: 337–354.

Sithole, G. & Vosselman, G. 2004. Experimental comparison of filter algorithms for bare-earth extraction from airborne laser scanning point clouds. *ISPRS Journal of Photogrammetry and Remote Sensing* 59: 85–101.

Srivastava, A., Singh, S., Ahn, C.Y., Oh, H.M. & Asthana, R.K. 2013. Monitoring approaches for a toxic cyanobacterial bloom. *Environmental Science & Technology* 47: 8999–9013.

Stenberg, B., Rossel, R.A.V., Mouazen, A.M. & Wetterlind, J. 2010. Chapter five – visible and near infrared spectroscopy in soil science. *Advances in Agronomy* 107: 163–215.

Stoney, W.E. 2005. A guide to the global explosion of land-imaging satellites. markets and opportunities. *Earth Imaging Source* 2: 10–14.

Stuckens, J., Verstraeten, W., Delalieux, S., Swennen, R. & Coppin, P. 2009. A dorsiventral leaf radiative transfer model: Development, validation and improved model inversion techniques. *Remote Sensing of Environment* 113: 2560–2573.

Thom, A.S. 1975. *Momentum, Mass and Heat Exchange of Plant Communities: Edited by J.L. Monteith*.

Tonolli, S., Dalponte, M., Vescovo, L., Rodeghiero, M., Bruzzone, L. & Gianelle, D. 2011. Mapping and modeling forest tree volume using forest inventory and airborne laser scanning. *European Journal of Forest Research* 130: 569–577.

Ustin, S.L., Gitelson, A.A., Jacquemoud, S., Schaepman, M., Asner, G.P., Gamon, J.A. & Zarco-Tejada, P. 2009. Retrieval of foliar information about plant pigment systems from high resolu-

tion spectroscopy. *Remote Sensing of Environment* 113: S67–S77.

Ustin, S.L., Roberts, D.A., Gamon, J.A., Asner, G.P. & Green, R.O. 2004. Using imaging spectroscopy to study ecosystem processes and properties. *BioScience* 54: 523–534.

van der Meer, F. & de Jong, S.M. 2006. *Imaging spectrometry: Basic principles and prospective applications*, Kluwer Academic Publishers, Dordrecht, The Netherlands.

van Leeuwen, M. & Nieuwenhuis, M. 2010. Retrieval of forest structural parameters using LiDAR remote sensing. *European Journal of Forest Research* 129: 749–770.

Vane, G., Goetz, A.F. & Wellman, J.B. 1984. Airborne imaging spectrometer: A new tool for remote sensing. *IEEE Transactions on Geoscience and Remote Sensing* GE-22: 546–549.

Vastaranta, M., Holopainen, M., Yu, X., Hyyppä, J., Mäkinen, A., Rasinmäki, J., Melkas, T., Kaartinen, H. & Hyyppä, H. 2011. Effects of individual tree detection error sources on forest management planning calculations. *Remote Sensing* 3: 1614–1626.

Vauhkonen, J., Tokola, T., Maltamo, M. & Packalén, P. 2010. Applied 3d texture features in ALS-based forest inventory. *European Journal of Forest Research* 129: 803–811.

Verhoef, W. & Bach, H. 2007. Coupled soil-leaf-canopy and atmosphere radiative transfier modeling to simulate hyperspectral multi-angular surface reflectance and TOA radiance data. *Remote Sensing of Environment* 109: 166–182.

Verrelst, J., Alonso, L., Camps-Valls, G., Delegido, J. & Moreno, 2012a. Retrieval of vegetation biophysical parameters using gaussian process techniques. *IEEE Transactions on Geoscience and Remote Sensing* 50: 1832–1843.

Verrelst, J., Muñoz, J., Alonso, L., Delegido, J., Rivera, J.P., Camps-Valls, G. & Moreno, J. 2012b. Machine learning regression algorithms for biophysical parameter retrieval: Opportunities for Sentinel-2 and -3. *Remote Sensing of Environment* 118: 127–139.

Vinciková, H., Pechar, L. & Hanuš, J. 2013. *Měření a využití spektrální odrazivosti (reflektance) slunečního záření z hladiny povrchových vod.*

Vindušková, O. & Frouz, J. 2013. Soil carbon accumulation after open-cast coal and oil shale mining in northern hemisphere: a quantitative review. *Environmental Earth Sciences* 69: 1685–1698.

Vogelmann, J.E., Rock, B.N. & Moss, D.M. 1993. Red edge spectral measurements from sugar maple leaves. *International Journal of Remote Sensing* 14: 1563–1575.

Vos, R.J., Hakvoort, J.H.M., Jordans, R.W.J. & Ibelings, B.W. 2003. Multiplatform optical monitoring of eutrophication in temporally and spatially variable lakes. *Science of The Total Environment* 312: 221–243.

Vosselman, G. 2000. Slope based filtering of laser altimetry data. *International Archives of Photogrammetry and Remote Sensing* 33: 935–942.

Wei, G., Shalei, S., Bo, Z., Shuo, S., Faquan, L. & Xuewu, C. 2012. Multi-wavelength canopy LiDAR for remote sensing of vegetation: Design and system performance. *ISPRS Journal of Photogrammetry and Remote Sensing* 69: 1–9.

Weiss, M., Baret, F., Myneni, R.B., Pragnere, A. & Knyazikhin, Y. 2000. Investigation of a model inversion technique to estimate canopy biophysical variables from spectral and directional reflectance data. *Agronomie* 20: 3–22.

Widlowski, J.L., Taberner, M., Pinty, B., Bruniquel-Pinel, V., Disney, M., Fernandes, R., Gastellu-Etchegorry, J.P., Gobron, N., Kuusk, A., Lavergne, T., Leblanc, S., Lewis, P.E., Martin, E., Mol̀fttus, M., North, P.R.J., Qin, W., Robustelli, M., Rochdi, N., Ruiloba, R., Soler, C., Thompson, R., Verhoef, W., Verstraete, M.M. & Xie, D. 2007. Third radiation transfer model intercomparison (RAMI) exercise: Documenting progress in canopy reflectance models. *Journal of Geophysical Research D: Atmospheres* 112.

Wulder, M.A., White, J.C., Nelson, R.F., Næsset, E., Ørka, H.O., Coops, N.C., Hilker, T., Bater, C.W. & Gobakken, T. 2012. Lidar sampling for large-area forest characterization: A review. *Remote Sensing of Environment* 121: 196–209.

Young, S.J., Johnson, B.R. & Hackwell, J.A. 2002. An in-scene method for atmospheric compensation of thermal hyperspectral data. *Journal of Geophysical Research: Atmospheres* 107: 4774.

Yu, X., Hyyppä, J., Holopainen, M. & Vastaranta, M. 2010. Comparison of area-based and individual tree-based methods for predicting plot-level forest attributes. *Remote Sensing* 2: 1481–1495.

Yu, X., Litkey, P., Hyyppä, J., Holopainen, M. & Vastaranta, M. 2014. Assessment of low density full-waveform airborne laser scanning for individual tree detection and tree species classification. *Forests* 5: 1011–1031.

Zarco-Tejada, P.J., Miller, J.R., Harron, J., Hu, B., Noland, T.L., Goel, N., Mohammed, G.H. & Sampson, P. 2004. Needle chlorophyll content estimation through model inversion using hyperspectral data from boreal conifer forest canopies. *Remote Sensing of Environment* 89: 189–199.

Zarco-Tejada, P.J., Miller, J.R., Noland, T.L., Mohammed, G.H. & Sampson, P.H. 2001. Scaling-up and model inversion methods with narrowband optical indices for chlorophyll content estimation in closed forest canopies with hyperspectral data. *IEEE Transactions on Geoscience and Remote Sensing* 39: 1491–1507.

Zarco-Tejada, P.J., Pushnik, J.C., Dobrowski, S. & Ustin, S.L. 2003. Steady-state chlorophyll a fluorescence detection from canopy derivative reflectance and double-peak red-edge effects. *Remote Sensing of Environment* 84: 283–294.

Zhu, W., Tian, Y.Q., Yu, Q. & Becker, B.L. 2013. Using hyperion imagery to monitor the spatial and temporal distribution of colored dissolved organic matter in estuarine and coastal regions. *Remote Sensing of Environment* 134: 342–354.